UC Berkeley
UC Berkeley Electronic Theses and Dissertations

Title

Estimation Challenges in Batteries: From Prevailing Li-ion Batteries to Emerging Alternative Lithium Sulfur Batteries

Permalink

https://escholarship.org/uc/item/1v164989

Author

DANGWAL, CHITRA

Publication Date

2023

Peer reviewed|Thesis/dissertation

Estimation Challenges in Batteries: From Prevailing Li-ion Batteries to Emerging
Alternative Lithium Sulfur Batteries

By

Chitra Dangwal

A dissertation submitted in partial satisfaction of the

requirements for the degree of

Doctor of Philosophy

in

Engineering - Civil and Environmental Engineering

in the

Graduate Division

of the

University of California, Berkeley

Committee in charge:

Professor Scott J. Moura, Chair
Professor Marta Gonzalez
Professor Bryan D. McCloskey

Fall 2023

Estimation Challenges in Batteries: From Prevailing Li-ion Batteries to Emerging
Alternative Lithium Sulfur Batteries

Abstract

Estimation Challenges in Batteries: From Prevailing Li-ion Batteries to Emerging
Alternative Lithium Sulfur Batteries

By

Chitra Dangwal

Doctor of Philosophy in Engineering - Civil and Environmental Engineering

University of California, Berkeley

Professor Scott J. Moura, Chair

This dissertation delves into the challenges associated with modeling, state estimation, and
parameter identification for currently prevailing lithium-ion (Li-ion) battery technologies and
the emerging frontiers of lithium-sulfur (Li-S) batteries. With rapid development in elec-
trification, Lithium-ion (Li-ion) batteries have reshaped the realms of portable electronics,
electric mobility, grid storage, and renewable energy systems. The increasing scale and de-
mand for battery systems warrant research efforts to improve battery management systems
and explore alternative high-energy materials. This dissertation explores two crucial areas
of focus: the development of scalable algorithms for large battery packs with heterogene-
ity and the design of algorithms for advanced battery chemistry, specifically Lithium-Sulfur
technology.

Chapters 2 to 4 focus on the challenges of Li-ion battery packs, addressing real-time power
estimation in the presence of heterogeneity among individual cells. A computationally ef-
ficient and scalable algorithm for estimating the state of power (SOP) for a heterogeneous
battery pack using interval prediction is first introduced in Chapter 2. In Chapter 3, the
focus shifts from theoretical exploration to empirical validation, as we experimentally verify
the performance of the SOP algorithm proposed in Chapter 2. In Chapter 4, heterogeneity in
the cells is further explored, where uncertainty in thermal parameters is also addressed. The
addition of thermal heterogeneity needed a more accurate and robust interval algorithm than
originally proposed in Chapter 2. Chapter 4 enhances the performance of interval prediction
using reachability analysis for mixed monotonic systems. Chapters 2 through 4 unravel the
complexities of the SOP framework, elucidating its theoretical foundations, practical limita-
tions, and the prospective transformative influence it could have on the optimization of the
performance of a heterogeneous battery pack.

Transitioning to emerging technologies, Chapters 5 and 6 shift the focus to Li-S batteries.
Chapter 5 investigates global parameter sensitivity for a zero-dimensional Li-S battery model,

addressing challenges in parameter identification crucial for battery management systems. Global sensitivity analysis is employed to understand parameter relevance and interdependence, highlighting the impact of different parameter distributions on model performance. Chapter 6 focuses on efficient modeling and state estimation algorithms for Li-S batteries, proposing a physics-informed neural network model with a moving horizon state estimator. The state estimation accuracy is compared with the extended Kalman filter. The developed model and a moving horizon estimator framework demonstrate robust state estimation accuracy under varying current profiles.

In conclusion, this dissertation contributes to advancing the understanding and optimization of established and emerging battery technologies, providing valuable insights for applications ranging from automotive to grid storage.

Contents

List of Figures

List of Tables

Acknowledgments

I would like to express my gratitude first and foremost to my adviser Professor Scott Moura for all his support and guidance in my entire PhD journey. I feel extremely fortunate to have had the opportunity to work with him and learn from him. His thought process, ideas, and drive were influential in my time at UC Berkeley.

My gratitude also extends to Professor Marta Gonzalez, Professor Bryan D. McCloskey, and Professor Xinfan Lin for their valuable feedback and guidance in my Qualifying exam, which contributed significantly to my academic progress. I express my thanks to Benjamin Sebastien from SAFT and Wente Zeng from Total Energies for their constructive feedback and guidance.

To my eCAL lab mates turned friends, Guillaume and Dylan, your companionship, insightful discussions, and the collaborative atmosphere during both work and non-work meetings have enriched and made my PhD experience truly fulfilling. I am also thankful to Dr. Zhijia Huang and Dr. Dong Zhang for their help and guidance.

Special thanks to David for his constant support, engaging intellectual conversations, and everlasting laughs.

My deepest gratitude extends to my mom, Subodhani, my dad, Shailender, and my brother, Ashwani, for consistently being my cheerleaders in every endeavor throughout my life.

Thank you, everyone, for being a part of my PhD journey!

Chapter 1

Introduction

1.1   Background and motivation

With the growing rise in electrification, Li-ion batteries have become ubiquitous in various applications ranging from portable electronics, electric vehicles (EVs), and stationary energy storage due to their high energy density, relatively lightweight design, and long cycle life.

Rechargeable Li-ion batteries invented by Dr. John Goodenough in 1980 have revolutionized the energy storage industry. Since its first commercialization in 1991 by Sony Corporation, the Li-ion battery has gone through rapid technological development. Its high energy density and lightweight allows energy storage in a compact and lightweight form making it a preferred choice in laptops and smartphones. Increasing environmental concerns regarding fossil fuel usage have also expedited the transition to electric mobility, where lithium-ion batteries are playing a pivotal role.

Advances in materials, including lithium iron phosphate (LFP), lithium manganese oxide(LMO), and Nickel Manganese Cobalt(NMC) improved the stability, safety, and energy density of Li-ion batteries. These efforts also resulted in decreasing its cost from $1000/kWh in 2007 to $200/kWh in 2017 [1]. Ongoing research in Li-ion batteries continues to push for reducing cost, enhancing safety, and increasing the available energy density.

At present, the prevailing Li-ion technology in the market comprises of intercalation-based cathodes (such as NMC, LFP, LMO), liquid electrolytes, and graphite anodes. Li-ion batteries, while highly successful, face challenges such as the availability of raw materials (like cobalt) and safety issues related to dendrite growth, overheating, and thermal runaways. Ongoing research focuses on addressing these challenges through the development of alternative materials, solid-state electrolytes, and improved battery management systems.

In this dissertation, we focus on two areas of development.

1. Advanced battery power estimation algorithm for a heterogeneous battery pack.

   Along with material development, advancement in Li-ion battery algorithm development has played a crucial role in the commercialization of these batteries. As the
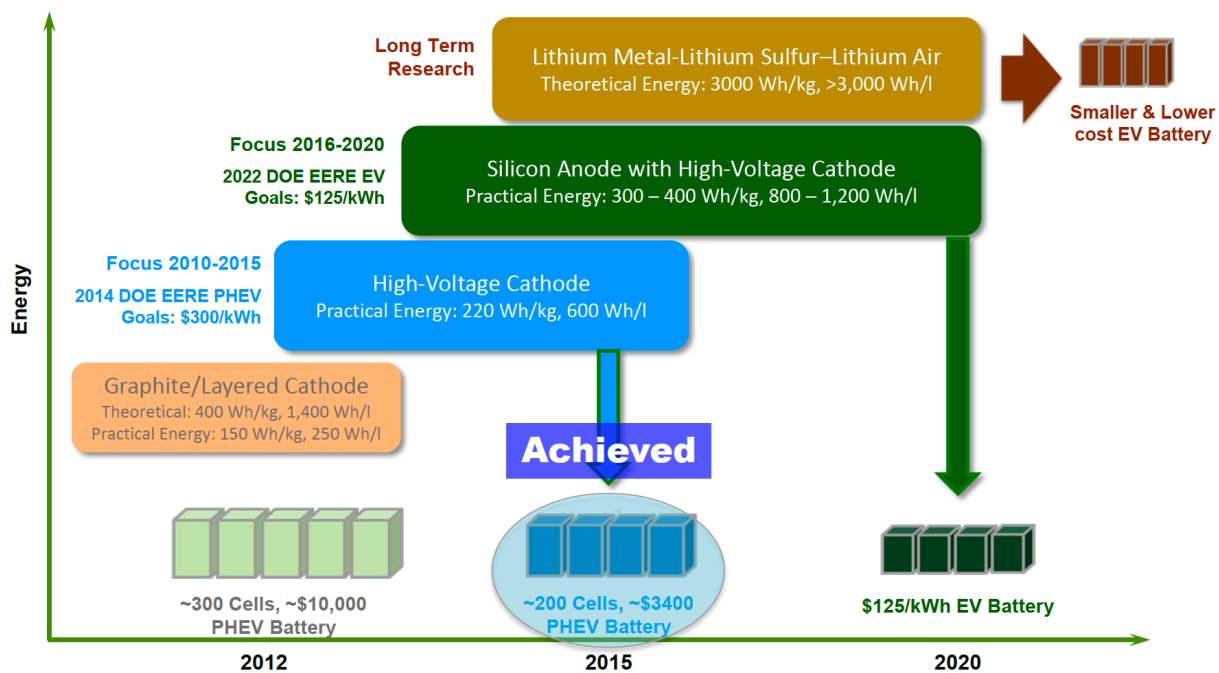
Figure 1.1: Battery research roadmap; Source: Overview of the DoE VTO Advanced Battery R&D Program - DoE USA, 2016 [2]

battery systems are becoming bigger and more complex, with the battery packs compromising thousands of cells, the need for an efficient battery management system (BMS) has become critical. The BMS plays a vital role in monitoring the performance and health of the battery and optimizes its performance and longevity. As technology is progressing, BMS needs to be more advanced in its estimation and control algorithms.

This dissertation addresses the intricate challenge of power estimation in battery packs with heterogeneous cells. Given the inherent cell-to-cell variation in these packs, this research focuses on pioneering algorithm design in an area that currently lacks maturity.

2. Modeling and estimation for alternative materials: Sulfur cathodes

Lithium Sulfur batteries are a potential alternative to Li-ion batteries. The cathode in Li-S is composed of sulfur, and the anode is made of lithium or lithium-containing materials. Compared to current Li-ion batteries, Li-S batteries have high energy density ($\sim 2600 Wh/kg$), which is 2-3 greater than current Li-ion batteries. Figure 1.1 shows the research roadmap for the development of high-energy batteries detailed in [2].

Research in the modeling and estimation of Li-S batteries is currently in its early stages. In [3], the authors emphasize the lack of maturity in the development of modeling and estimation algorithms for Li-S. This dissertation seeks to make a contribution to the

advancement of Li-S battery technology by concentrating on tackling challenges related to parameter identification, model development, and state estimation.

1.2 Pack state estimation challenges of Li-ion batteries

Accurate state estimation is crucial for monitoring the internal states and overall health of batteries. While a significant body of literature has focused on individual cells or packs with uniform cells, the challenge intensifies in the context of battery packs found in applications like electric vehicles and stationary storage systems, which often are composed of hundreds or thousands of cells. These battery packs, comprised of numerous cells exhibit inherent cell-to-cell variation as shown in Fig. 1.2, resulting from factors like manufacturing variability, cell aging, and temperature gradients in the pack, which make 'pack level' state estimation challenging. The simplistic approach for pack-level state estimation is treating the whole pack as an aggregate cell which would be a representation of the average property of the pack. This approach does not address the variability in cells and can cause some cells to operate in unsafe regimes. The other way to do pack estimation is to estimate the state of each individual cell. Even though this approach would ensure accurate pack state estimation, it faces practical limitations, due to the intensive computational and memory costs involved and available sensing hardware. Hence innovative and novel approaches are needed to overcome the state estimation challenges of heterogeneous battery packs that ensure the scalability and safety of the battery.

In this dissertation, state of power (SOP) estimation for battery packs with heterogeneous cells is studied. In a range of applications from automotive to grid storage, the accurate prediction of available power within battery packs stands as a critical factor in optimizing the overall system performance. The SOP metric serves as a key parameter in predicting the peak power performance of a battery system, thereby playing a central role in the assessment of its fitness for specific operational demands. In this dissertation SOP estimation framework is presented specially for series-connected heterogeneous cells. The SOP algorithm methodology presented utilizes an interval prediction algorithm, which accounts for the inherent cell-to-cell variability. Importantly, the proposed algorithm distinguishes itself by predicting pack power without fixating on any individual cell. This not only enhances the computational efficiency of the methodology but also renders it highly scalable to accommodate any number of cells. As we delve into the subsequent chapters, the dissertation will unfold the intricacies of the proposed SOP framework, shedding light on its theoretical underpinnings, practical implications, and real-world applicability. Different case studies also offer insights into the algorithms' adaptability and reliability when confronted with the complexities inherent in practical battery pack scenarios.
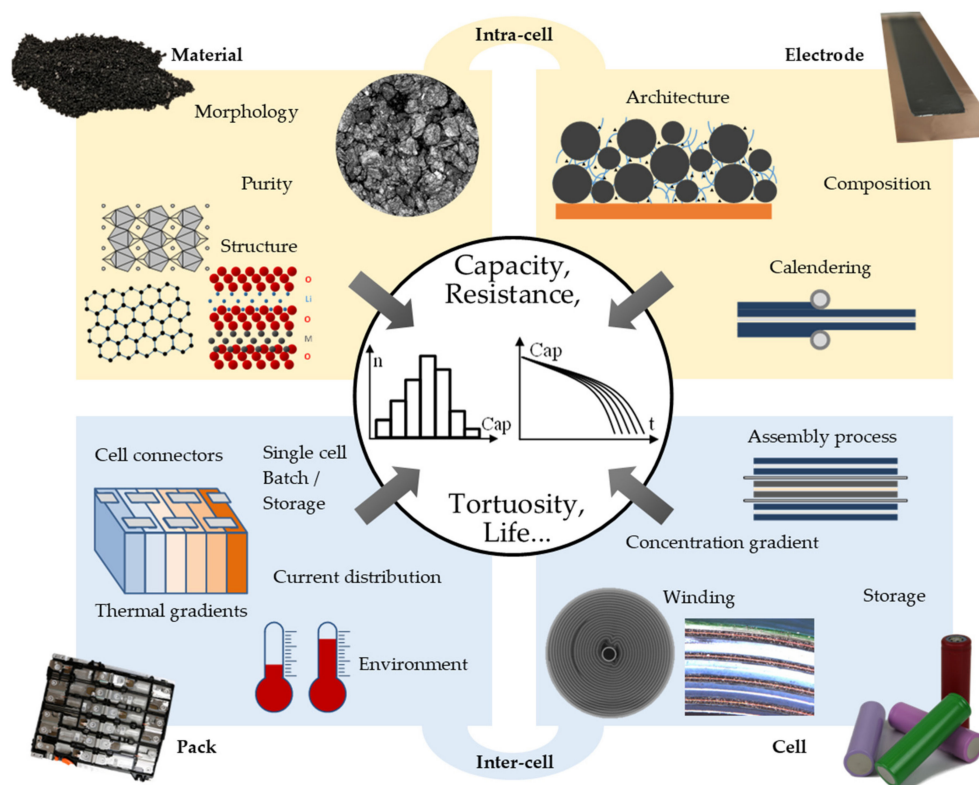
Figure 1.2: Origins of Cell to Cell Variability, Source:[4]

1.3 Modeling & estimation challenges of Li-S battery

Lithium-sulfur (Li-S) batteries have gained significant attention in the past decade, as an advanced battery chemistry, providing an alternative to current Li-ion batteries with the prospect of high theoretical energy density, abundant supply, and cost-effectiveness. Despite these promising attributes, the translation of Li-S battery technology into commercial applications is impeded by a scarcity of comprehensive modeling and estimation approaches. Efficient modeling and estimation algorithms are crucial for the development of an effective battery management system (BMS) to monitor its performance and health and optimize its usage. In this dissertation, we focus on two main estimation challenges associated with Li-S battery i.e., parameter identification and state estimation. The dissertation first dwells on the challenges associated with parameter identification of Li-S models. The lack of available information in the literature regarding a-priori distributions of Li-S parameters complicates the parameter identification process. This is elucidated by examining the parameter sensitivities of a physics-based electrochemical model using global sensitivity analysis.

The dissertation further explores the modeling and states estimation challenges of Li-S. The primary complexity in modeling and estimation of Li-S batteries arises from the
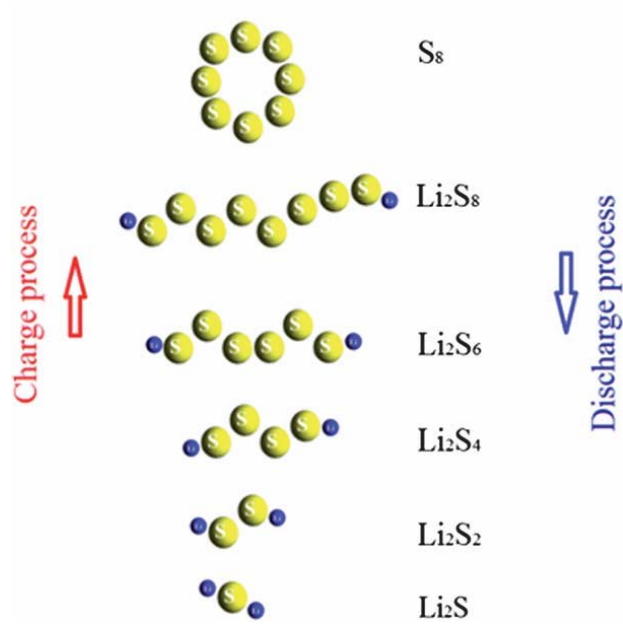
Figure 1.3: Electrochemical process of a Li-S cell [5]

intricate reaction kinetics at the cathode. Unlike a typical Li-ion battery, where the anode and cathode reactions simplify to a single-step oxidation/reduction process, Li-S batteries involve a multi-step electrochemical reaction during both charge and discharge, leading to various polysulfide species, as shown in Fig. 1.3. The resulting dynamics of Li-S give rise to a complex nonlinear system of differential-algebraic equations (DAE), posing challenges for state estimation. The challenge of modeling and state estimation in Li-S electrochemical systems is exacerbated by the numerical stability of existing models and the system's inherent weak observability, adding complexity and interest to the task.

Addressing these challenges, this dissertation proposes a novel solution in the shape of a physics-informed neural network model. This model not only precisely captures the electrochemical complexities of Li-S batteries but also offers valuable insights into the system's physical states. Utilizing this neural network model, the research employs a Moving Horizon Estimator (MHE) framework to achieve accurate state estimation. This study not only advances Li-S battery technology but also lays the groundwork for incorporating innovative modeling and estimation approaches into the realm of energy storage research and development.

1.4 Outline of the Dissertation and Contributions of Each Chapter

This dissertation addresses the various challenges in modeling, state, and parameter estimation for the established Li-ion technologies and the emerging frontiers of lithium-sulfur (Li-S) batteries. Chapters 2, 3 and 4 are dedicated to the challenges of Lithium-ion battery packs, in real-time power estimation due to the inherent heterogeneity among individual cells. Chapters 5 and 6 venture into the state and parameter estimation challenges of promising but nascent Li-S battery technology.

In Chapter 2, we examine the problem of estimating real-time power limits in lithium-ion battery packs containing heterogeneous cells. Accurate prediction of available power in battery packs is crucial for managing performance in automotive and grid storage applications. This chapter presents a methodology to estimate the state of power (SOP) of a battery pack, composed of series connected heterogeneous cells using intervals. The presented SOP framework combines an interval prediction algorithm, with a modified reference governor. The concept of interval prediction accounts for cell-to-cell variability by predicting bounds that enclose all the states of all the cells at any given time. In this chapter cell heterogeneity is taken in battery electrical parameters. The proposed algorithm accurately predicts pack power without fixating on any individual cell. This makes the presented methodology computationally efficient and scalable to any number of heterogeneous cells.

Contributions of Chapter 2 are:

- Developing a computationally efficient and scalable framework for estimating SOP for a battery pack with heterogeneity amongst the cells.

- Application of interval prediction to account for cell heterogeneity by predicting bounds that enclose all the states of all the cells at any given time.

Building upon the foundation laid in Chapter 2, Chapter 3 transitions to experimental validation, quantifying the accuracy of State of Charge (SOC), State of Health (SOH), and State of Power (SOP) interval estimation algorithms. One of the main objectives, in this chapter is to experimentally validate the SOP algorithm developed in Chapter 2. Interval SOC and SOH algorithms previously developed for heterogeneous cells [6, 7] were also experimentally validated in the process, as the SOP algorithm proposed in Chapter 2 is integrated with interval SOC and SOH framework. The interval algorithms (SOC/SOH/SOP) were previously validated on a model-to-model framework. In this chapter, we experimentally validate the algorithms for a heterogeneous battery pack. In our experimental case study, the battery module constructed consists of 3 cells in series. This module is purposely composed of heterogeneous cells, to mimic large battery packs. The algorithm's performance with actual data is quantified.

The main contributions of this chapter are as follows:

- Experimental validation of joint SOC and SOH algorithm developed in [6, 7]

- Experimental validation of SOP algorithm developed in Chapter 2

- Inclusion of heterogeneity in Open Circuit Voltage (OCV)- SOC maps caused by aging of cells.

In Chapter 3, we focus on the problem of power prediction for a battery pack with cell-to-cell heterogeneity. Preliminary work for power prediction was explored in Chapter 1, where we investigated SOP estimation for ECM battery models with uncertain electrical parameters. Experimental validation of the algorithms in Chapter 2 highlighted the need for accurate models to increase the accuracy of the algorithms. With this in mind, we focus on including the effect of heterogeneity in thermal parameters for SOP estimation. The inclusion of heterogeneity in thermal parameters showed limitations in the performance of the interval predictor proposed in Chapter 1. In this chapter hence, accurate and robust interval prediction algorithms were explored. Inclusive and tight bounds for interval prediction of the battery thermal model are achieved using reachability analysis for mixed monotonic systems. The designed SOP algorithm is validated for two case studies i.e., a small HEV and a Tesla Powerwall storage. Both these applications were chosen as they are immensely different in terms of the number of cells in the pack and the prediction time horizon. The results show accurate SOP prediction in both the case study thereby validating the robustness of the algorithm. The novel contributions of this chapter are as follows:

- The first adoption of reachability analysis to equivalent circuit battery models for SOP prediction.

- An extended definition for state-of-power (SOP) for multi-cell heterogeneous battery packs that considers limits due to voltage, SOC, temperature, and current. The heterogeneity is considered in both electrical and thermal parameters of the cells for more practical application.

Transitioning to the realm of emerging battery technologies, Chapters 5 and 6 shift the focus to lithium-sulfur (Li-S) batteries. The challenges in modeling, state, and parameter estimation are explored.

Chapter 5 examines global parameter sensitivity in a zero-dimensional lithium-sulfur (Li-S) battery model. Li-S batteries are an appealing cell chemistry due to their high theoretical energy density, abundant supply, and low cost. Due to the lack of complete understanding of the underlying working mechanisms for Li-S cells, the development of mathematical models and state estimation is still in its early stages. Model development and parameter identification are closely associated. Both are essential for developing battery management systems (BMS) in commercialized Li-S-powered applications. This paper highlights the parameter identification challenges associated with Li-S models. Sensitivity analysis helps with parameter identification by revealing information about parameter relevance and interdependence. Sensitivity analysis also helps in understanding different physical ranges of parameters, and their impact on model performance/response. In this work, we examine global sensitivity

analysis (GSA). A key challenge for GSA, especially in Li-S batteries, is a lack of available information in the literature about a-priori distributions of Li-S parameters. This paper aims to elucidate this challenge by comparing GSA under different parameter distributions. Three model parameters are chosen in this analysis, and their sensitivities are compared under three different distributions. We find that, under certain distributions of parameters, the relative importance of the parameters shifts.

The main contributions of this chapter are:

- Analysis of a 0-D lithium Sulfur battery model using global sensitivity analysis.

- Analysis of Global sensitivity methods and their robustness to parameter distributions. To the authors' knowledge, this is the first work that explores how parameter distributions change the results of global sensitivity analysis.

Chapter 6, focuses on developing efficient modeling and state estimation algorithms for Li-S batteries. Work in the field of modeling and estimation of Li-S batteries is limited. The development of efficient modeling and estimation algorithms is essential for the commercialization of Li-S batteries. The complex reaction pathway of Li-S makes the application of the available physics-based model and its use in estimation algorithms numerically challenging. In this study, we propose a physics-informed neural network model that accurately approximates the electrochemical model, while providing insight into the physical states of the model. The moving horizon estimator (MHE) framework is applied to the developed neural network model for accurate state estimation and its efficiency is compared to the more widely used extended Kalman filter (EKF). The state estimation accuracy is tested on different varying current profiles. The results validate the robustness of the algorithm.

The novel contributions of this chapter are summarized as follows:

- The physics-informed neural network model architecture is used to capture the electrochemical dynamic of the Li-S battery.

- The model estimates a diverse range of charging and discharging profiles accurately. Most literature in Li-S is limited to replicating the discharge performance [8, 9].

- Moving horizon estimation is used for state estimation of the Li-S neural network model for accurate state estimation. The accuracy of the MHE state estimator is compared with EKF.

Chapter 2

Pack Level State-of-Power Prediction for Heterogeneous Cells

2.1 INTRODUCTION

This chapter examines the problem of estimating real-time power limits in lithium-ion battery packs containing heterogeneous cells.

With increasing electrification in every domain of technology, the importance of energy storage systems is immense. Lithium-ion batteries have played a key role and have become ubiquitous in many applications, especially the automotive industry and grid energy storage. These batteries are being constantly improved to extract their maximum potential, which means pushing the operational limits, safely. Accurate estimation of the battery's state hence becomes critical to increasing performance.

To quantify cell performance, different 'states of performance' are defined in literature. For example, state of charge (SOC) is an indication of the available battery capacity at any instant. State of health (SOH) is an indication of battery age and degradation. SOP similarly provides information about the peak power performance of the cell. Power performance of an electrified vehicle is translated to the acceleration, braking, charging, or climbing capacity of the vehicle, which is directly related to the discharge and charging capability of the vehicle's battery. Unlike SOC and SOH, where myriad research publications have been produced, the available literature on SOP estimation remains limited, despite its critical role for providing safe charge/discharge limits.

The two main methods for SOP estimation can be categorized as: (i) the characteristic map based method, and (ii) the model-based prediction method [10]. The former is a straightforward method that uses maps of power parameters and battery states stored offline in the BMS [10, 11]. Although this technique is very easy to implement, the accuracy is limited for a number of reasons. Firstly, the maps are designed from the battery's static characteristics, and ignores the dynamic behavior. Secondly, the method is open loop and not closed-loop. This makes it susceptible to modeling and measurement errors [10, 11]. The

model-based SOP estimation method, on the other hand, is more accurate and robust since
it accounts for dynamics and utilizes feedback. This second method use a battery model to
describe the cell dynamics. The most common model used is the equivalent circuit model
(ECM) [10–20]. Commonly, Taylor series expansion is used to approximate the nonlinear
voltage output function, and the battery is subject to constraints on current, voltage and
SOC [10–12, 14–20]. This method is also vulnerable to inaccuracies, due to errors associ-
ated with Taylor series approximation and the omission of time-varying (state-dependent)
parameters. Article [10] presented an SOP estimation method using a genetic algorithm as
an improvement over Taylor's method, to increase accuracy at longer time-scales. Article
[21] includes thermal dynamics in the ECM model and introduces a linear parameter-varying
(LPV) model predictive control (MPC) based method for SOP. The LPV model accounts for
parameter variations in the ECM, and MPC is used for accurate power estimation. Finally,
the articles [13, 17, 21] include temperature constraints (in addition to SOC, voltage and
power limits) to define a safe area of battery operation. Most of the existing SOP estimation
literature, including the papers discussed above, focus on a single cell. Only a few address
the challenges associated with estimating power in a pack.

A battery pack consists of many cells arranged in a series-parallel fashion to reach a de-
sired voltage and capacity. The cells have inherent heterogeneity that arise from micro meter
length scale effects (electrode particle densities, porosity, radius etc.) to macro length scale
effects (cell manufacturing and assembly, external temperature variation). When modeling
packs, a nominal set of parameters is considered to represent all cells [10, 12]. This assump-
tion is valid if parameter heterogeneity is negligible, or at relatively low currents with low
cell-to-cell temperature variation. For power prediction, where the objective is to evaluate
the maximum current of the battery, heterogeneity among the cells significantly impacts
overall pack power. Hence, heterogeneity needs to be accounted [16, 18, 20].

Cell heterogeneity can cause differences in the peak power availability among cells. The
few existing techniques to address heterogeneity are based on two approaches. The first
approach is to monitor the state of all the cells in a pack [16]. The second approach is
to identify the 'weakest' cells in a pack [18, 20]. The former approach, where all the cells
are monitored, results in accurate power prediction but requires substantial computational
power and memory for processing and storing data on each cell [18, 20]. These problems
escalate significantly with the number of cells in the pack. The latter method relies on iden-
tifying the 'weakest' cells for power prediction, and then applies single cell techniques. This
usually relies on certain assumptions about the cell characteristics, e.g. some parameters are
homogeneous and/or follow prescribed patterns [18, 20]. This method uses less computation
and memory than the first method, but is not as accurate because the assumptions about
cell characteristics generally do not hold true, as we explore later. Also, the set of possible
weakest cells increases substantially with the number of cells in a pack.

This paper provides a framework for estimating SOP for a battery pack with heterogeneity
amongst the cells. Heterogeneity is addresses by considering the battery as a dynamic
system with parametric uncertainty. The mentioned challenges in the existing literature,
namely increased computational burden and the 'weakest cell' concept, are overcome by

utilizing the interval prediction approach [22–24]. The interval prediction approach focuses on determining bounds on the states of the system, rather than estimating the states of all/any of the cells. The battery model used in this study is a parameter varying system to account for state dependent parameters and also includes the thermal dynamics. These features advance the state-of-art for accurate SOP prediction.

The paper is organized as follows. Section 2.2 details the battery model considered in the study. Section 2.3 discusses different challenges associated with SOP prediction and details the problem statement. Section 2.4 outlines the overall framework for SOP estimation, describing the tools/methods used in addressing the challenges of section 2.3. The concept of interval prediction is introduced to handle the heterogeneity problem, which combined with a reference governor forms the basis for power prediction. Section 2.5 presents the simulation results done to validate the SOP algorithm. Finally, section 2.6 provides conclusion for the overall SOP estimation study.

2.2   Battery Modelling

Cell modelling is broadly classified into heuristic and physics based approaches, which trade-off simplicity with fidelity [25]. In this paper, we require accuracy and scalability to model many cells in a pack. Hence, the battery model chosen for power prediction analysis is a 1st order ECM coupled with two-state thermal dynamics. The ECM predicts voltage using the open circuit voltage (OCV), connected in series with an ohmic resistance R_0 and an R-C pair $\{R_1, C\}$.

Electrical Part

The voltage dynamics of a single cell indexed k are:

$$\dot{z}_k(t) = \frac{1}{Q_k} I_k(t), \tag{2.1}$$

$$\dot{V}_{c,k} = -\frac{1}{R_{1,k}(z_k, T_k)C_k(z_k, T_k)}\, V_{c,k} + \frac{1}{C_k(z_k, T_k)}\, I_k(t), \tag{2.2}$$

$$V_k(t) = OCV(z_k(t)) - V_{c,k}(t) - R_{0,k}(z_k, T_k)I_k(t), \tag{2.3}$$

where $V_{c,k}$, i.e. the voltage drop across the RC pair, and z_k (SOC) represent the states of the kth cell. Symbol Q_k is the cell capacity taken as a constant. Input I_k denotes current, which is positive for charging and negative for discharging. The parameters $R_{0,k}$, $R_{1,k}$, C_k depend on SOC and temperature, yielding a time-varying and state-dependent system.

In this study, the pack is configured as a set of m heterogeneous cells (or modules) connected in series.

Thermal Part

The temperature dynamics are modelled by considering two lumped thermal states for each cell, i.e. core temperature $T_{c,k}$ and surface temperature $T_{s,k}$ [26]. The cell temperature T_k is taken as the average temperature between core and surface. Each cell has a heat generation term $\dot{q}_k(t)$, which accounts for the ohmic and over-potential thermal losses. The cells exchange heat with a coolant fluid and their neighboring cells, as seen in (2.4)-(2.5). The temperature evolution for each cell is given by [26]:

$$C_c \dot{T}_{c,k}(t) = \dot{q}_k(t) + \frac{T_{s,k}(t) - T_{c,k}(t)}{R_c}, \tag{2.4}$$

$$C_s \dot{T}_{s,k}(t) = \frac{T_{f,k}(t) - T_{s,k}(t)}{R_u} - \frac{T_{s,k}(t) - T_{c,k}(t)}{R_c}, \tag{2.5}$$

$$\dot{q}_k(t) = I_k(t)(V_k(t) - OCV(z_k(t)), \tag{2.6}$$

$$T_k(t) = \frac{1}{2}(T_{s,k}(t) + T_{c,k}(t)). \tag{2.7}$$

The parameters C_c, C_s represents the thermal capacity of the core and surface, while R_c, R_u represent thermal resistance for the heat conduction between core and surface, and heat convection between surface and coolant, respectively. The coolant interacting with all the cells is assumed constant across all cells $T_{f,k}$. This model, i.e. ECM coupled with thermal dynamics, from hereon is referred to as ECMT.

2.3   Challenges
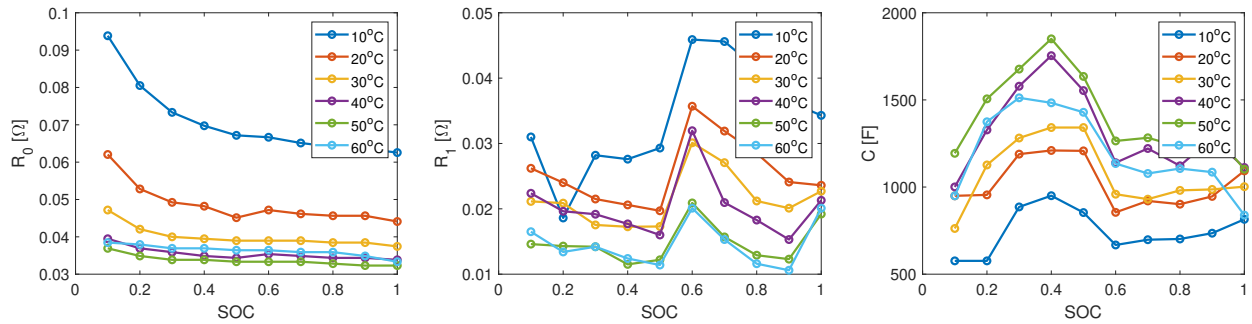
Figure 2.1: Experimentally derived data on how R_0, R_1, C vary with SOC and $T = \frac{1}{2}(T_c + T_s)$.

This section first presents practical challenges associated with SOP estimation, then provides a formal problem statement.

SOP Definition

Unlike SOC, SOP does not have a clear definition in the literature. The most used definition for SOP is based on evaluating the maximum power that can be applied/supplied to the cell constantly for a finite-time horizon [1-4,6-11], while maintaining the cell in a safe operating regime. Since battery loads in many applications are often difficult to predict, the reference case of constant current, constant voltage is used to define SOP. Since voltage remains nearly constant during a constant current pulse, the maximum power calculations in the literature often simplify to determining maximum current [10–20]. The constant current definition is also useful in a practical sense. The battery cells can be regulated at constant current for many application, e.g. charging EVs. The other SOP definition used in some literature is the ratio of peak power to nominal power [15].

SOP is defined by the safety constraints. If the definition of 'safe operating conditions' are altered, then the SOP would correspondingly change. Certain battery operating limits are specified by the manufacturer to prevent instantaneous failure (e.g. thermal runaway, short circuiting), or to prevent battery health degradation (e.g. SEI formation, lithium plating). Generally, these operating limits are defined by voltage, SOC, current and temperature.

The SOP analysis presented here focuses on predicting the maximum current that can be constantly supplied over a fixed time horizon without violating any safety constraints. An NMC-graphite cell with 2.6Ah nominal capacity is considered for analysis in this study. The safety constraints considered are voltage, SOC, current and temperature, as detailed in Table 2.1.

Table 2.1: Safety constraint parameter

Constraints	Lower limit	Upper limit
Voltage : $V_{min} \leq V \leq V_{max}$	2.8 V	4.2 V
SOC : $SOC_{min} \leq SOC \leq SOC_{max}$	0.1	1
Current : $I_{min} \leq I \leq I_{max}$	-10 C	10 C
Temperature : $T_{min} \leq T \leq T_{max}$	$10°C$	$60°C$

Parameter varying system

The parameters of the ECM model are not constant, and dependent on SOC and temperature. This means many methods in the literature, e.g. [10, 12], will be inaccurate. For this reason we consider a parameter varying system which not only accounts for state dependent parameters, but also avoids the inaccuracy in using Taylor series approximation for handling the dependence of OCV on SOC. Fig. 2.1 provides experimentally derived data of ECM parameters variation with SOC and temperature of an 2.6 Ah NMC cell .

Heterogeneity

Scaling the power estimation problem from the cell level to the pack level increases complexity. Due to cell-to-cell interactions, a single cell's dynamics are affected by the neighboring cells. Moreover, the inherent cell-to-cell heterogeneity means one cannot simply use a single representative cell for the entire pack.

Fig. 2.2 shows the simulated voltage evolution for 50 heterogeneous cells undergoing a Hybrid Power Pulse Characterization (HPPC) cycle. Parameters for each cell are chosen at random from a uniform distribution, whose mean is the nominal value of the parametric set. In the simulation, $\pm 50\%$ parametric variation is considered in the 'ECM' parameters i.e. R_0, R_1, C, $\pm 5\%$ variation is considered in the cell capacity Q, and $\pm 5\%$ variation is considered in initial SOC, $z(0)$. Note that none of the cells with extreme parameters in terms of capacity, ohmic resistance or initial SOC can be deemed as the uniformly 'limiting/extreme' cells of the pack. In fact, the limiting cells are sometimes from the interior of the parametric distribution, and can change throughout the cycle.
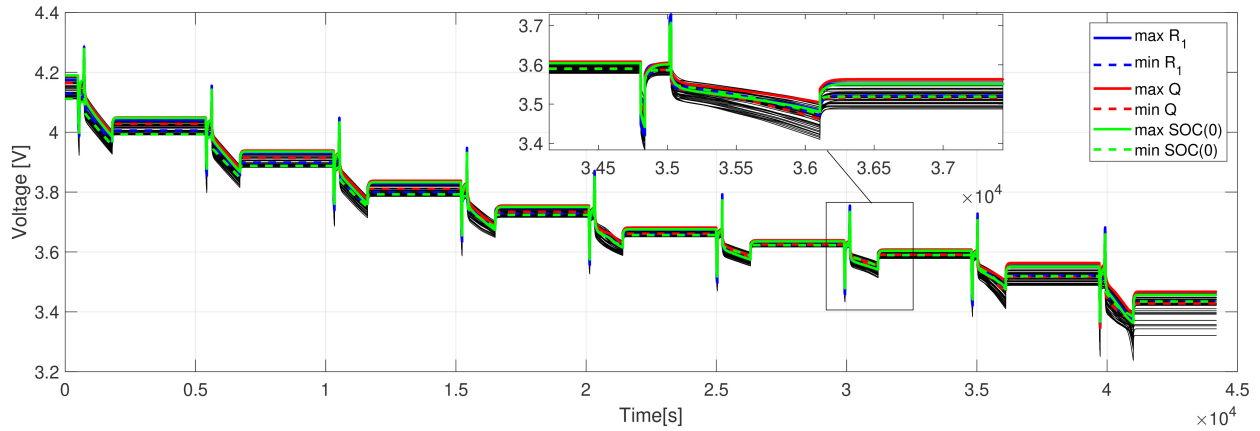
Figure 2.2: Cell voltage responses for 50 heterogeneous cells connected in series under HPPC cycle.

Problem Statement

Considering all the aforementioned challenges, the SOP prediction problem for a battery pack can be stated as peak power prediction for a parameter varying system, with uncertain parameters. The ECM part of the model is parameter-varying, as the parameters R_0, R_1, C are state (SOC and temperature) dependent. Additionally, these parameters along with Q are uncertain as well. Temperature differences between the cells is also introduced because of different heat generation among the cells. The SOP problem can be stated as determining $I_{max,pack}^{dis}$, $P_{max,pack}^{dis}$ for discharge limits, and $I_{max,pack}^{ch}$, $P_{max,pack}^{ch}$ for charge limits. For a chosen prediction time horizon T_p, the maximum constant current that can be supplied to

the battery pack with m cells at any instant t is:

$$\begin{cases} I_{max,pack}^{dis} = \min_{k=1,...m} \left(I_{max,k}^{dis} \right) \\ I_{max,pack}^{ch} = \min_{k=1,...m} \left(I_{max,k}^{ch} \right) \end{cases} \tag{2.8}$$

where $I_{max,pack}^{dis}$ and $I_{max,pack}^{ch}$ are the maximum constant discharge and charge current appli-
cable for the entire battery pack, and $I_{max,k}^{dis}$ and $I_{max,k}^{ch}$ are the maximum current applicable
to the cell 'k' of the pack. Maximum constant current of each cell 'k' further is calculated
by considering the SOC, voltage, temperature and current constraints of each cell.

$$\begin{cases} I_{max,k}^{dis} = \min \left\{ i_{max,k}^{dis|SOC}, i_{max,k}^{dis|V}, i_{max,k}^{dis|T}, i_{max,k}^{dis|I} \right\} \\ I_{max,k}^{ch} = \min \left\{ i_{max,k}^{ch|SOC}, i_{max,k}^{ch|V}, i_{max,k}^{ch|T}, i_{max,k}^{ch|I} \right\} \end{cases} \tag{2.9}$$

where $i_{max,k}^{dis|SOC}$, $i_{max,k}^{dis|V}$, $i_{max,k}^{dis|T}$, $i_{max,k}^{dis|I}$ are the maximum constant current discharge pulse that
can be applied for T_p duration, without violating the SOC, voltage, temperature and current
constrains, respectively, for any cells in the pack.

SOP can thus be estimated (bounded) for the pack with m cells in series as:

$$SOP : \begin{cases} P^{dis} = m \cdot I_{max,pack}^{dis} \cdot \underline{V}(I_{max,pack}^{dis}) \\ P^{ch} = m \cdot I_{max,pack}^{ch} \cdot \underline{V}(I_{max,pack}^{ch}) \end{cases} \tag{2.10}$$

where
$$\underline{V} \left(I_{max,t}^{dis} \right) = \min \left\{ V \left(I_{max,t}^{dis} \right) \;\middle|\; \forall \{1,..,m\}, \; t \in [t, \; t + T_p] \right\},$$
$$\underline{V} \left(I_{max,t}^{ch} \right) = \min \left\{ V \left(I_{max,t}^{ch} \right) \;\middle|\; \forall \{1,..,m\}, \; t \in [t, \; t + T_p] \right\}$$

2.4 SOP Prediction Algorithm

To predict SOP, we seek the maximum current such that safe operating conditions are
satisfied. To handle cell heterogeneity, we estimate bounds on the state trajectories under
parameter uncertainty, rather than evaluating the states of all cells. This is formalized as
follows. Consider the dynamical system:

$$\dot{x} = f(t, x, p), \tag{2.11}$$

where x represents the states and p represents the parameter, $x(t; t_0, x_0, p)$ indicates the
state of the system at time $t \geq t_0$ given the initial condition x_0. For the ECMT system
formulated as (2.11), the objective is to determine bounds on the state trajectories, given
uncertain parameters and initial condition. This is accomplished by computing upper and
lower bounds on the ECMT state trajectories, i.e.

$$x(t; t_0, x_0, p) \subset [\underline{x}(t), \overline{x}(t)]. \tag{2.12}$$

We have the following state bounds for the ECMT:

$$
\begin{cases}
\underline{SOC}(t) \leq SOC_k \leq \overline{SOC}(t); \quad \underline{V_c}(t) \leq V_{c,k} \leq \overline{V_c}(t) \\
\underline{T_c}(t) \leq T_{c,k} \leq \overline{T_c}(t); \quad \underline{T_s}(t) \leq T_{s,k} \leq \overline{T_s}(t)
\end{cases}
\tag{2.13}
$$

Since we assume OCV is a monotonic function of SOC, the following can be implied for voltage when $I(t) \geq 0$:

$$
\overline{V}(t) = OCV(\overline{SOC}(t)) + \overline{V_c}(t) + I(t)R_{0,max}, \tag{2.14}
$$

$$
\underline{V}(t) = OCV(\underline{SOC}(t)) + \underline{V_c}(t) + I(t)R_{0,min}, \tag{2.15}
$$

$$
\overline{T}(t) = \frac{1}{2}(\overline{T_c}(t) + \overline{T_s}(t)), \quad \underline{T}(t) = \frac{1}{2}(\underline{T_c}(t) + \underline{T_s}(t)). \tag{2.16}
$$

For SOP evaluation during charging, the following constraints will be enforced:

$$
I_{max} \colon \overline{V}(t) \leq V_{max}; \quad \overline{SOC}(t) \leq SOC_{max}; \quad \overline{T}(t) \leq T_{max}. \tag{2.17}
$$

Similarly for discharging:

$$
I_{max} \colon V_{min} \leq \underline{V}(t); \quad SOC_{min} \leq \underline{SOC}(t); \quad T_{min} \leq \underline{T}(t). \tag{2.18}
$$

This section describes the SOP algorithm developed, focusing on the design of all the sub-components involved. The interval predictor is used to predict the state/output bounds for a given parametric uncertainty and input current, which when combined with modified reference governor (MRG) is used to estimate the maximum current that can be applied such that the constraints (2.17)-(2.18) are satisfied. The SOP model also uses the concept of interval observer and adaptive parameter bounding to increase the accuracy of the algorithm by better estimation of state initial conditions and parameter bound at any given time. Fig. 2.4 shows the overall SOP framework and how the different sub-components are interconnected.

Interval Prediction

Interval state estimation with observers has been studied for several continuous LPV systems [6, 27, 28], with a fair degree of accuracy, stability and robustness. The availability of output measurement and control over observer gain selection aids in keeping the interval observer state stable and estimation error small. This, however, is not the case when working with state interval prediction. A poorly designed interval prediction algorithm can cause the interval predictor to be unstable, as shown in [23], or have very large overapproximation. The interval prediction model used for this study follows the work in [23]. This subsection discusses the assumptions and theorem used for predicting ECMT state bounds. For the given LPV system:

$$
\dot{x}(t) = A(p)x(t) + b(p, u(t)), \tag{2.19}
$$

$x \in \mathbb{R}^n$ is the system state, $u(t) \in \mathbb{R}^m$ is the input vector and p is the vector of parameters
with a known range of uncertainty. The input $u(t)$ is known, and the matrices $A \in \mathbb{R}^{n \times n}$,
$B \in \mathbb{R}^{n \times m}$ are both continuous and locally bounded. To design the interval predictor, a
system with state vectors $[\underline{x}(t), \overline{x}(t)]$ is built. The following assumptions are used to construct
the state predictor system:

Assumption 1: The initial uncertainty in the state of the system (2.19), i.e. $x_0 \in [\underline{x}_0, \overline{x}_0]$
is known.

Assumption 2 [23]: The matrix $A(p)$ can be decomposed into a Metzler matrix $A_0 \in$
$\mathbb{R}^{n \times n}$ and matrices $\Delta A_i \in \mathbb{R}^{n \times n}, i = 1, .., N$, where $N \in \mathbb{Z}_+$ such that $A(p) = A_0 +$
$\sum_{i=1}^N \lambda_i(p)\Delta A_i$.

Assumption 3: Bounding function $[\underline{b}, \overline{b}]$ exists and is known, such that for all $p \in [\underline{p}, \overline{p}]$
$: \underline{b} \leq b(p, u(t)) \leq \overline{b}$.

Notation: For a matrix $A \in \mathbb{R}^{n \times n}$, define $A^+ = \max\{0, A\}$ and $A^- = A^+ - A$. For a
vector $x \in \mathbb{R}^n$, define $x^+ = \max\{0, x\}$ and $x^- = x^+ - x$.

Theorem [23]: Consider system (2.19) that satisfies Assumptions 1-3. The state tra-
jectory of (2.19) is enclosed within the interval $[\underline{x}(t), \overline{x}(t)]$, whose bounds evolve according
to:

$$\dot{\underline{x}}(t) = A_0 \underline{x}(t) - \Delta A_+ \underline{x}^-(t) - \Delta A_- \overline{x}^+(t) + \underline{b} \tag{2.20}$$

$$\dot{\overline{x}}(t) = A_0 \overline{x}(t) + \Delta A_+ \overline{x}^+(t) + \Delta A_- \underline{x}^-(t) + \overline{b} \tag{2.21}$$

where $\Delta A_+ = \sum_{i=1}^N \Delta A_i^+$, $\Delta A_- = \sum_{i=1}^N \Delta A_i^-$. The input-to-state stability properties of the
interval predictor above are described in [23].

Interval prediction for battery power prediction1

For the ECMT model described in Section 2.2, power prediction is accomplished using the
interval predictor design mentioned above. From the model equations, it can be seen that
the two states, i.e. $\{SOC, V_c\}$, that represent the electric part of the model for each cell
are associated with uncertain parameters $\{R_0, R_1, C, Q\}$. The thermal parameters of the
model, on the other hand, are assumed known, as heterogeneity in thermal properties across
the cells is relatively small compared to the heterogeneity in the electric properties. This
assumption can be problematic when the thermal parameters vary significantly across the
cells. Considering the ECM part of the model, the uncertain set of parameters are:

$$p = \begin{bmatrix} R_{0,k} & R_{1,k} & C_k & Q_k \end{bmatrix} \in \mathbb{R}^4. \tag{2.22}$$

The heterogeneity as well as state dependence of the above parameters is clubbed together
as uncertainty in the model parameters. Bounds on the uncertain parameters are assumed
to be known:

$$\underline{p} \leq p_k(t) \leq \overline{p} \qquad \forall\, k \in \{1, 2, ..m\}, \tag{2.23}$$

where $\underline{p} = [\underline{R_0} \quad \underline{R_1} \quad \underline{C} \quad \underline{Q}]$, $\overline{p} = [\overline{R_0} \quad \overline{R_1} \quad \overline{C} \quad \overline{Q}]$. The ECM model equation can be formulated in the form of (2.19), where:

$$x = \begin{bmatrix} x_1 \\ x_2 \end{bmatrix} = \begin{bmatrix} SOC \\ V_c \end{bmatrix}, \tag{2.24}$$

$$A(p) = \begin{bmatrix} 0 & 0 \\ 0 & -\tau \end{bmatrix}, \quad \text{where } \tau = \frac{1}{R_1 C}, \tag{2.25}$$

$$b(p, u) = \begin{bmatrix} \frac{1}{Q} \\ \frac{1}{C} \end{bmatrix} I, \quad u(t) = I(t). \tag{2.26}$$

To apply the predictor model equations (2.20)-(2.21) to the ECM, the following decomposition of $A(p)$ is applied.

$$A_0 = \begin{bmatrix} 0 & 0 \\ 0 & -\overline{\tau} \end{bmatrix}, \quad \Delta A_+ = \begin{bmatrix} 0 & 0 \\ 0 & \overline{\tau} - \underline{\tau} \end{bmatrix}, \quad \Delta A_- = \begin{bmatrix} 0 & 0 \\ 0 & 0 \end{bmatrix} \tag{2.27}$$

The bounding function for b depends on the sign of current applied. When $I \geq 0$

$$\underline{b} = \begin{bmatrix} \frac{1}{\overline{Q}} & \frac{1}{\overline{C}} \end{bmatrix}^{\top} I, \quad \overline{b} = \begin{bmatrix} \frac{1}{\underline{Q}} & \frac{1}{\underline{C}} \end{bmatrix}^{\top} I \tag{2.28}$$

The resulting state equations during charging $(I(t) \geq 0)$ hence can be written as:

$$\underline{\dot{SOC}}(t) = \frac{1}{\overline{Q}} I(t), \tag{2.29}$$

$$\overline{\dot{SOC}}(t) = \frac{1}{\underline{Q}} I(t), \tag{2.30}$$

$$\underline{\dot{V_c}}(t) = -\overline{\tau}\underline{V_c} - (\overline{\tau} - \underline{\tau})\overline{V_c}^- + \frac{1}{\overline{C}} I(t), \tag{2.31}$$

$$\overline{\dot{V}_c}(t) = -\overline{\tau}\overline{V_c} + (\overline{\tau} - \underline{\tau})\overline{V_c}^+ + \frac{1}{\underline{C}} I(t). \tag{2.32}$$

The thermal part of the model, even with uniform thermal parameters across the cells, still has cell to cell temperature variation caused by non-uniform heat generation. The equations used to predict bounds on the thermal states are:

$$\underline{\dot{\zeta}}(t) = A_{0,T}\underline{\zeta} + \Delta A_T \underline{\zeta} + \underline{B_T}, \tag{2.33}$$

$$\overline{\dot{\zeta}}(t) = A_{0,T}\overline{\zeta} + \Delta A_T \overline{\zeta} + \overline{B_T}, \tag{2.34}$$

where $\zeta = \begin{bmatrix} T_c \\ T_s \end{bmatrix}$ and

$$A_{0,T} = \begin{bmatrix} -\frac{1}{R_c C_c} & \frac{1}{R_c C_c} \\ \frac{1}{R_c C_s} & -\left(\frac{1}{R_u C_s} + \frac{1}{R_c C_s}\right) \end{bmatrix}, \quad \Delta A_T = 0,$$

$$B_T = \begin{bmatrix} \frac{\dot{Q}_k}{C_c} & \frac{1}{R_u C_s}T_f \end{bmatrix}^\top = \begin{bmatrix} \frac{I_k(V_c + IR_0)}{C_c} & \frac{1}{R_u C_s}T_f \end{bmatrix}^\top,$$

$$\underline{B_T} = \begin{bmatrix} \frac{I_k\left(\underline{V_c} + I\underline{R_0}\right)}{C_c} & \frac{1}{R_u C_s}T_f \end{bmatrix}^\top, \overline{B_T} = \begin{bmatrix} \frac{I_k\left(\overline{V_c} + I\overline{R_0}\right)}{C_c} & \frac{1}{R_u C_s}T_f \end{bmatrix}^\top.$$

Equations (2.29)-(2.34) can be used for state interval prediction. Now that we can accurately predict bounds on the state of the uncertain LPV (ECMT) system, for a given current magnitude, the remaining task is to compute the maximum current which satisfies safety constraints. This is accomplished using the MRG, as explained in the next section.

Modified Reference Governor

The concept of MRG is to attenuate the input signal of a dynamical system with a pole at the origin, such that a set of constraints are satisfied (Fig. 2.3). The logic behind MRG is to iteratively compute, at any given time instant, the safe applicable current $I(t)$, as close as possible to the reference input current $I^r(t)$, such that the system constraints are always satisfied during the SOP prediction time horizon [29]. This is similar to the bisection approach implemented in [12] for maximum current computation. The reference current, I^r, is generally taken as the maximum safe current. The safe applicable current $I(t)$ is related to I_r as follows:

$$I(t) = \alpha I^r(t) \quad \forall \, t \in [t, \, t + T_p]. \tag{2.35}$$

Reference current I_r is typically a constant value, and $\alpha \in [0, 1]$ is the scaling factor that is evaluated to determine $I(t)$. Let Y represents the set of admissible state/outputs of the system, i.e. $SOC \in [SOC_{min}, \, SOC_{max}]$, $V \in [V_{min}, \, V_{max}]$ and $T \in [T_{min}, \, T_{max}]$, and y be output of the battery interval state predictor i.e. $[\underline{SOC}, \overline{SOC}, \underline{V}, \overline{V}, \underline{T}, \overline{T}]$. The scaling factor α_k is evaluated such that:

$$\alpha = \max\left\{\alpha \in [0, 1] \; : \; y \in Y, \quad t \in [t, t + T_p]\right\}. \tag{2.36}$$

In words, the objective is to obtain the maximum value of $\alpha \in [0, 1]$ which satisfies the safety constraints during the prediction time horizon. MRG accomplishes this by simulating the interval predictor battery model forward in time $[t, \, t + T_p]$ and checking if the constraints are satisfied. MRG initializes with $\alpha = 1$, and finds the optimal α using the bisection algorithm. If for a given value of α, the constrains are not satisfied, then the value of α is scaled down, and the predictor model is re-simulated. On the other hand, if the constrains are satisfied, α is scaled up so as to find the maximum value of α that satisfies the constraints. The MRG and interval predictor combined provide the SOP algorithm for the battery pack.
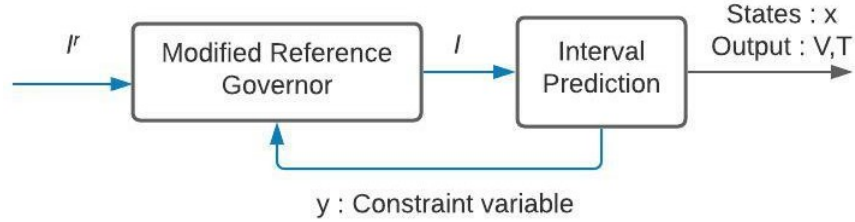
Figure 2.3: SOP prediction using MRG and interval prediction

Interval Observer

To complete the SOP prediction framework, the only missing component is initializing the state intervals. A relaxed approximation of the initial condition will directly lead to over-approximations in the state interval trajectory predictions. Accurate and tight initialization of the state intervals is crucial for interval prediction. Note that in most cases full knowledge of the state vectors in never available. In practice, only voltage, current, and temperature are measured. Consequently, the state must be estimated, via observers, from measured outputs in real time.

We focus on series connected heterogeneous cells and prefer precise state interval initialization for power prediction at any given instant. To this end, we apply the framework of interval observers in [6], as it also uses a similar battery-cell configuration. The main idea of the interval observer is similar to interval prediction: estimate the state intervals for an uncertain parameter system, given measurements, i.e. voltage and temperature. The state interval estimates (based on ECMT) of a heterogeneous battery pack $\overline{x}(t)$ and $\underline{x}(t)$ are obtained using the following assumptions:

1. Parametric uncertainty bound is known: $\underline{\theta} < \theta(t) < \overline{\theta}$

2. Initial condition bounds are known: $\underline{x_0} < x_0 < \overline{x_0}$

3. The maximum/minimum voltage and surface temperature across all series-connected cells are measured, along with current:

$$y(t) = [I(t), \max_k V_k(t), \max_k T_{s,k}(t), \min_k V_k(t), \min_k T_{s,k}(t)] \qquad (2.37)$$

The state intervals for the ECMT system are obtained using Lie derivatives, by first converting the nonlinear model dynamics into a partial-linear form:

$$\dot{\xi}_k = A_0 \xi_k + \delta A(\theta_k) \xi_k + b(\xi_k, \theta_k, u) \qquad (2.38)$$

$$V_k = H\xi_k + \delta h(\theta_k) u \qquad (2.39)$$

The interval observer design is based on the lemma in [6]. The following proposition [6]
provides the dynamics to obtain the interval estimates:

$$
\dot{\overline{\xi}} = (A_0 - \overline{L}H)\overline{\xi} + (\overline{\delta A}^+ \overline{\xi}^+ - \underline{\delta A}^+ \underline{\xi}^- - \overline{\delta A}^- \xi^+ +
$$
$$
\underline{\delta A}^- \underline{\xi}^-) + \overline{b}(t) + \overline{L}y + |\overline{L}|V \tag{2.40}
$$

$$
\dot{\underline{\xi}} = (A_0 - \underline{L}H)\underline{\xi} + (\underline{\delta A}^+ \underline{\xi}^+ - \overline{\delta A}^+ \underline{\xi}^- - \underline{\delta A}^- \overline{\xi}^+ +
$$
$$
\overline{\delta A}^- \overline{\xi}^-) + \underline{b}(t) + \underline{L}y + |\underline{L}|V \tag{2.41}
$$

where L is the observer gain to be selected. The procedure for constructing $A_0, \delta A, b, L,$
including mathematics behind obtaining (2.40)-(2.41), can be found in [6].

Adaptive Parameter bounding

The adaptive parameter bounding is a small improvement added to SOP prediction for
increasing state prediction accuracy. Interval prediction uses the parameter bound $[\overline{\theta}, \underline{\theta}]$ for
state bound prediction. As mentioned before, the parameters R_0, R_1, C are not constant but
dependent on states (SOC, temperature). Hence, defining ECM parameter bounds are not
straightforward. One of the simplest methods would be to take the extreme values from
the ECM parameter maps, but this results in conservative bounds. The adaptive parameter
bounding eliminates conservatism by defining a tighter parameter bound based on a localized
region of the parameter space. This is done without simulating the model, as follows:

1. For a constant current magnitude, given initial state intervals $[SOC_0, T_0]$ and predic-
tion horizon, we can easily estimate the SOC range where SOP prediction is relevant.
For charging $I > 0$:

$$
SOC_{high} = \overline{SOC_0} + \int_0^{T_p} \frac{I}{\underline{Q}}dt ; \qquad SOC_{low} = \underline{SOC_0} \tag{2.42}
$$

For discharging $I < 0$:

$$
SOC_{high} = \overline{SOC_0}; \qquad SOC_{low} = \underline{SOC_0} + \int_0^{T_p} \frac{I}{\underline{Q}}dt \tag{2.43}
$$

2. Since the ECMT only accounts for irreversible heat generation, both charging and
discharging are exothermic. Hence the temperature range where SOP prediction is relevant
can be between T_0 and the maximum temperature.

$$
T_{low} = \min(T_f, T_0); \quad T_{high} = T_{max} \tag{2.44}
$$

Therefore, the parameter bound chosen $[\overline{\theta}, \underline{\theta}]$ is taken as the parameter's extreme values
from the SOC and temperature region of focus $[SOC_{low}, SOC_{high}] \times [T_{low}, T_{high}]$.
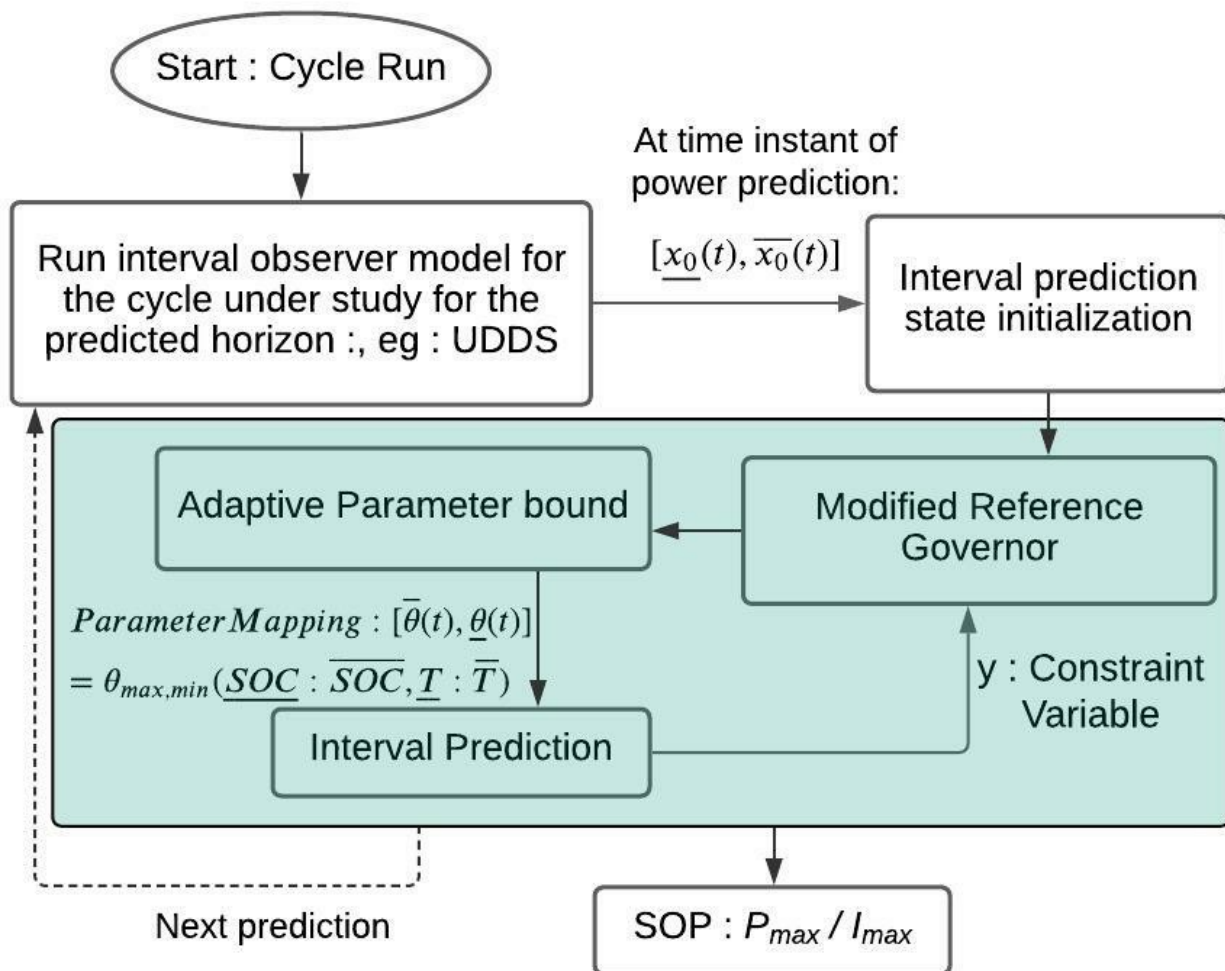
Figure 2.4: SOP framework showing the relationship between the interval observer, interval prediction, adaptive parameter bounds, and MRG.

2.5 Results

The SOP algorithm developed for heterogeneous cells in series is tested in this section, via simulation. An NMC cell with 2.6Ah nominal capacity is used. The cell data and input current profile (Fig. 4.6) used in study is same as the one used in [6] for state estimation. To demonstrate a hybrid electric vehicle application with a small battery pack, we consider 5 heterogeneous cells connected in series. A section of the UDDS cycle with a high C-rate is used for the analysis (Fig. 4.6). The prediction horizon for automotive applications is taken between 10sec-120sec in the literature. As the prediction horizon increases, the

heterogeneity effect worsens. Hence, for testing robustness, we take the prediction horizon as 120 sec. Figure 4.7 shows the voltage and state responses for the 5 cells subjected to the current input shown in Fig. 4.6. Both parameter and initial condition heterogeneity are considered.
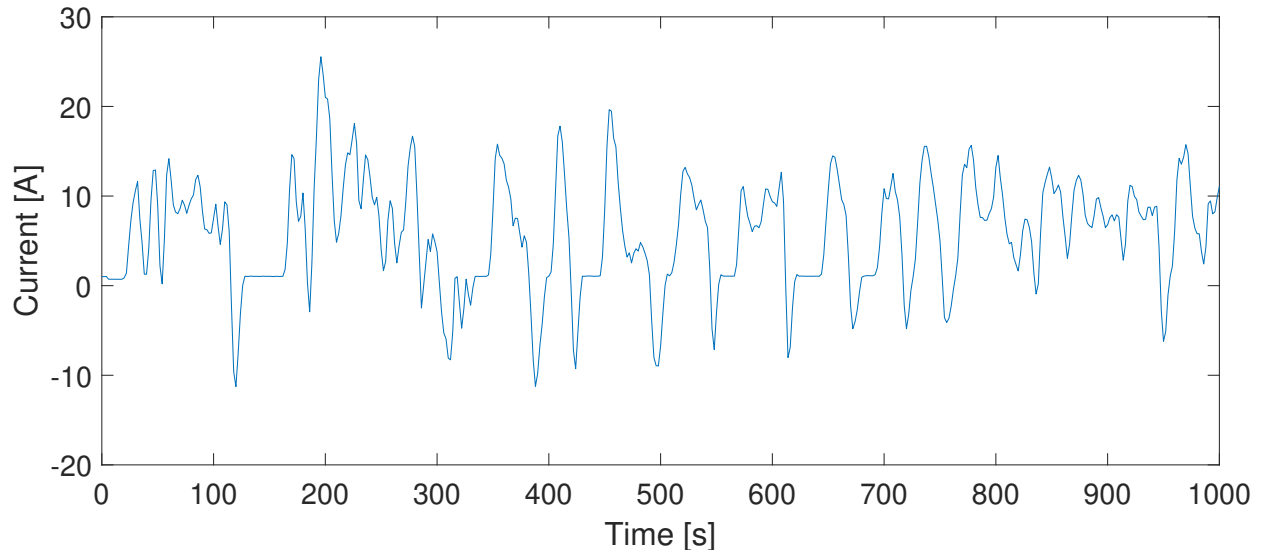
Figure 2.5: Current profile for analysis
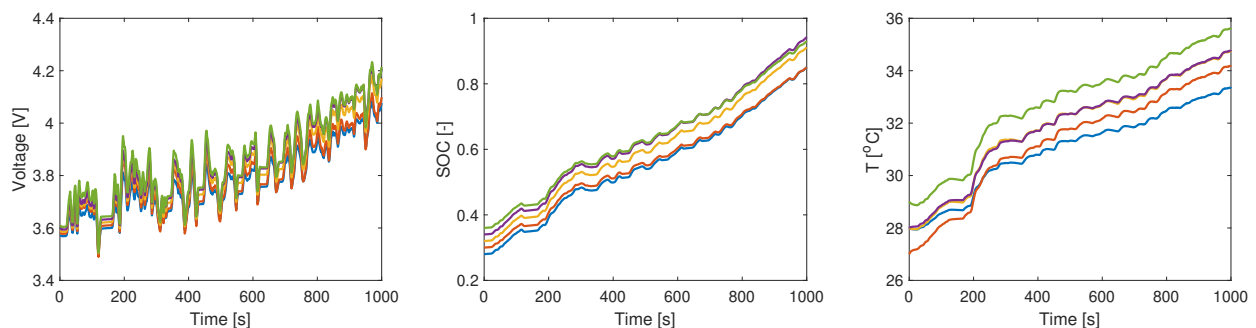
Figure 2.6: State and output profile for individual cells

For the given cycle, the predicted maximum current capability are shown in Fig. 4.8 for SOP under both charging and discharging. The solid line represents the SOP current values for the 5 individual cells, whereas the dotted line represents the upper and lower SOP current bounds obtained using the interval prediction approach. It should be noted that even though we show both the upper and lower bounds, the SOP of the pack is defined by the lower bound. This is because the lower SOP bound ensures safety for all cells.

The maximum safe current in this analysis is taken as 10C (i.e 26A), which equals I^r in the modified reference governor. Whenever the SOP algorithm predicts maximum 26A current, this signifies that the battery pack power is constrained by current limits. In other regions the power is limited by either SOC, voltage or temperature limits. For the cycle considered, we see that cell SOC, voltage and temperature increase over time. Temperature is expected to increase because the overall process is exothermic. The increasing SOC trend implies that the battery is running through a net charging profile. This is the reason behind the trend observed for SOP charge/discharge in Fig. 4.8. The battery cells in the simulations start from a low SOC regime. Hence, the charging SOP predicted is high initially. As the battery cell moves to higher SOC ranges, the charging power diminishes. Vice-versa is true for discharge power prediction. The highlight of the simulation study presented here, is the accuracy and tightness of the SOP prediction for the whole pack of heterogeneous cells. This is directly linked with the accuracy of the interval predictor and interval observer.

2.6 CONCLUSIONS

This paper presents a framework for SOP prediction in a battery pack. We first examine the definition of SOP, and analyze gaps in the literature for both cell-level and pack-level SOP prediction. We focus on the problem of heterogeneous cells in packs, and propose interval prediction as a solution. Specifically, we focus on obtaining accurate and tight state interval predictions, which are used to compute safe pack power limits. A reference governor is applied for obtaining the safe maximum applied current, which ultimately defines SOP. The proposed power estimation method yields accurate and relatively tight bounds, and is scalable with the number of cells in the pack, since it predicts bounds. This was illustrated via simulation on an HEV-like application.
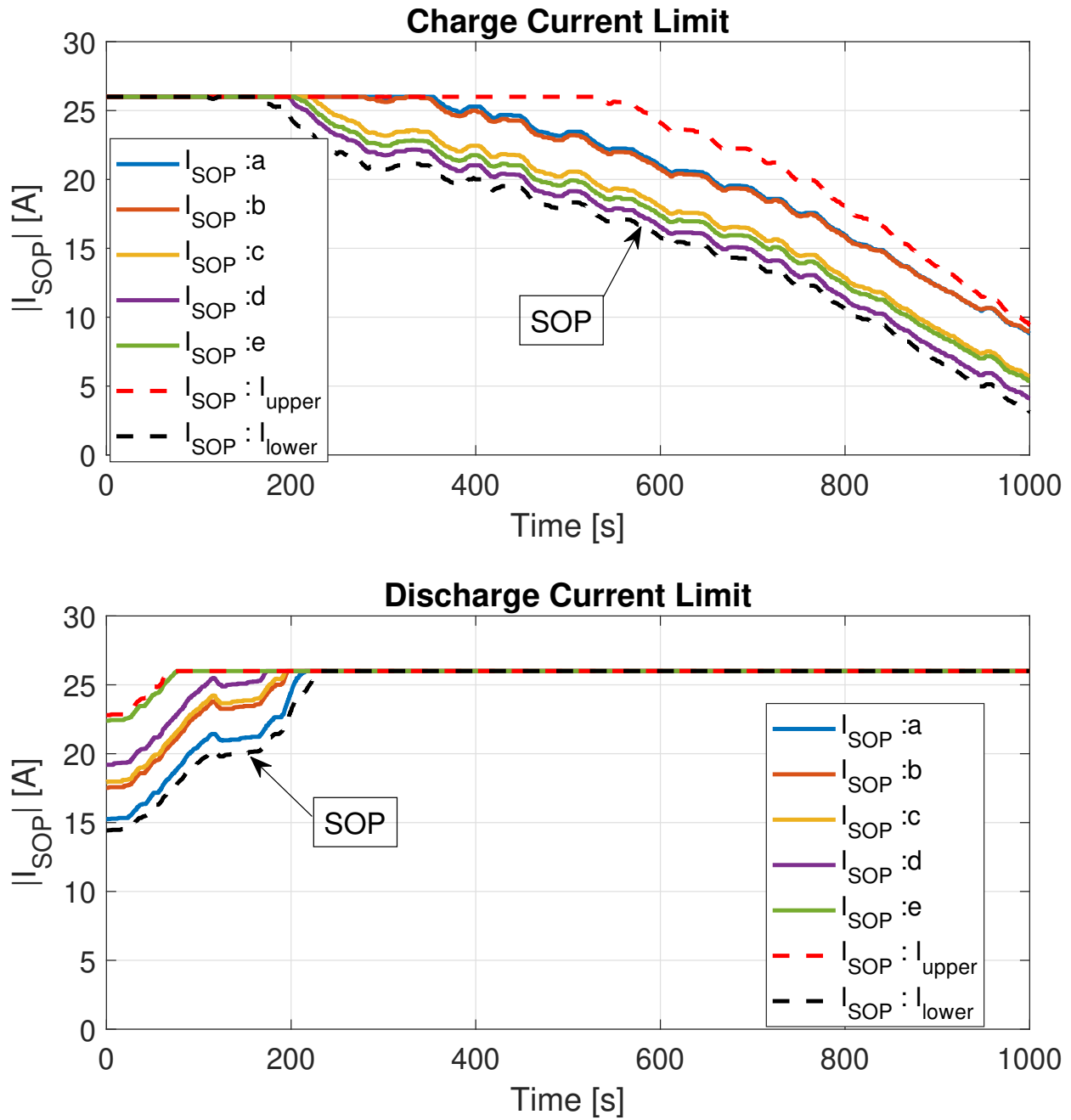
Figure 2.7: SOP: Charging and discharging current prediction

Chapter 3

Experimental Validation of Interval SOC, SOH and SOP algorithms

In this chapter, we experimentally quantify the estimation accuracy of SOC/SOH/SOP interval estimation algorithms with a 3-cell battery module.

3.1 INTRODUCTION

The SOC, SOH, and SOP [6, 7, 30] estimation in battery packs with heterogeneous cells were explored with SAFT and Total Energies. The algorithms were validated on a model-to-model framework. In this chapter, we experimentally validate the algorithms (SOC/SOH/SOP) for a heterogeneous battery pack. The algorithm's performance with actual data is quantified. In our experimental case study, the battery module constructed consists of 3 cells in series, as seen in Fig. 3.1 below.

This module is purposely composed of heterogeneous cells, to mimic large battery packs. During the experiments performed, the battery module is cycled, and the current, voltage, and temperature data are fed into the SOC, SOH, and SOP estimation algorithms. The current and voltage are also measured for all individual cells.

All the experiments, for parameter identification and algorithm validation were performed at 25°C.

Cell Specifications

The 3 battery cells used for validation are provided by SAFT. The cells are Li-ion NMC cells with 2.6Ah nominal capacity at 1C discharge rate. To generate cell heterogeneity, two of these cells were aged using accelerated aging tests to different cell capacities. The 3 cells were indexed #1, #2 and #5. Cell #5 is the cell with the maximum discharge capacity and cell #1 has the minimum discharge capacity. Table 3.1 shows the discharge capacities of the three cells used in the battery module.
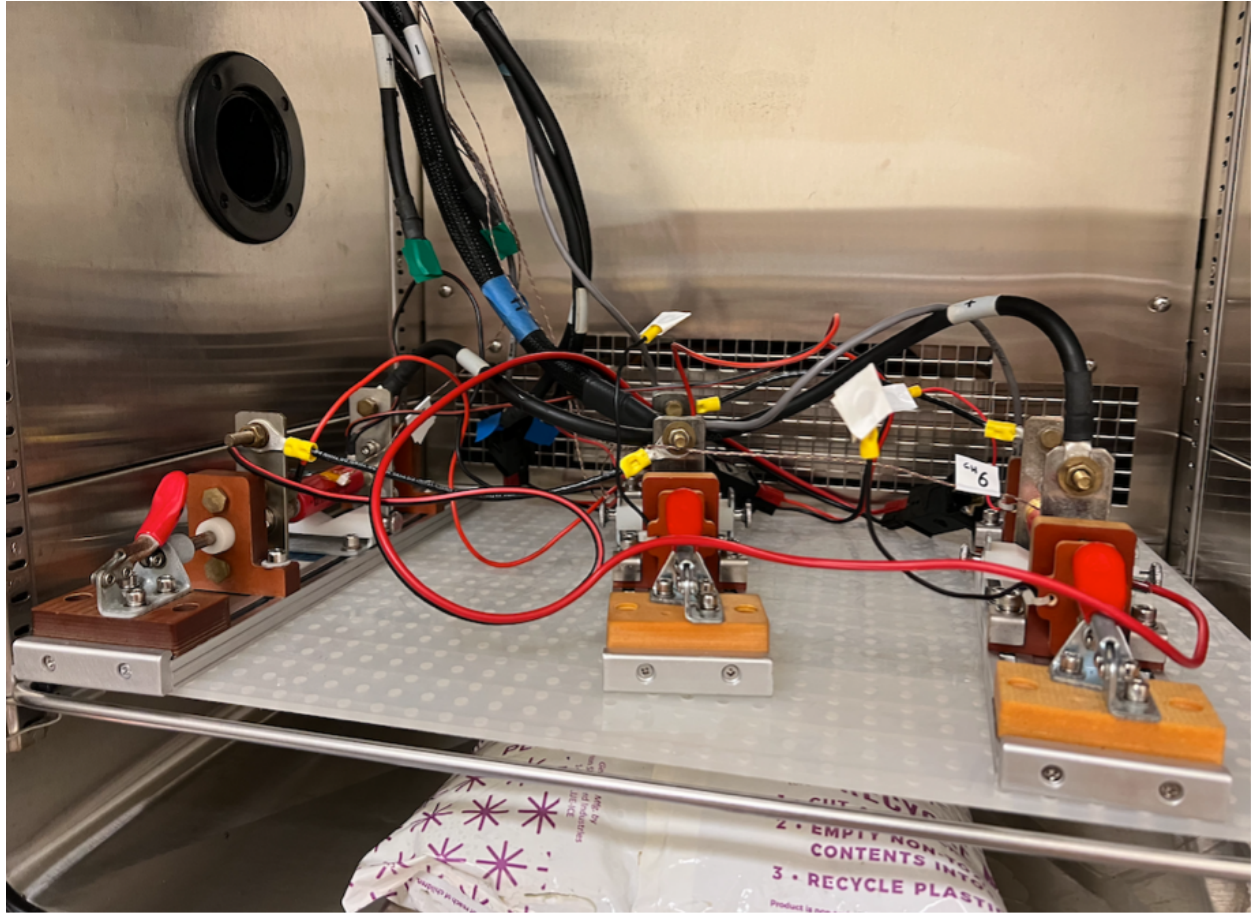
Figure 3.1: Battery pack: 3 Cells in series in PEC tester

Table 3.1: Experimental Safety constraints

Cell Index No.	C/50 discharge capacities (Ah)
#1	2.2469
#2	2.6312
#5	2.7503

The outline of this chapter is as follows. Section 3.2 goes over the experimental validation for the joint SOC/SOH estimator, where the SOH framework and interval SOC framework are integrated and tested together. The performance of the algorithm is tested, the limitations of the algorithm are discussed, and further improvements are explored. Section 3.3 goes over the experimental validation for SOP. The experiment plan for the SOP is discussed, and three different experimental frameworks are considered and tested.

3.2 Joint SOC/SOH Validation

Objective and outline of the algorithm

In this section, we evaluate the performance of an interval SOC algorithm [6, 7, 30] integrated with the SOH algorithm. The interval SOC algorithm [6] estimates the bounds of the state intervals for the battery pack with cell heterogeneity. The cell heterogeneity is modeled as a system with known parametric and initial condition uncertainty [6]. The SOH algorithm is used to quantify the parametric uncertainty in the system [7].

Figure 3.2 shows the integration of SOC [6] and SOH [7] algorithm. The SOH diagnostic cycle is run periodically, which then is used in the SOH algorithm to update the ECM parameters maps. One of the critical assumptions in the interval SOC algorithm is knowledge about the bounds of parametric uncertainty. SOH provides this knowledge of the upper and lower bounds of parameters of the entire battery pack that covers the true value.

We hence quantify the performance of this integrated SOC/SOH in terms of how tightly the interval estimate covers the true SOC values.

Parameter bound estimation using SOH algorithm

The SOH algorithm identifies the upper and lower bounds of parameters (SOH-related) of the entire battery pack that covers the true value. The algorithm proposed in the paper [6] follows the following steps:

1. Identify the two representative cells using feature-based polling

2. Estimate R1, R2, and C and Q of extreme cells using online RLS

3. Estimate R1, R2 and C for other discrete operating points (20°C – 40°C, 10% SOC – 100% SOC) using Sparse GPR

In the experiment validation on the 3 cells in the series pack, we first performed a diagnostic pulse test on the battery pack.

The diagnostic pulse test for parameter identification was done at different SOC for the cells, as shown in Fig. 3.3. The pulse was done at 9 different SOCs ranging from 10% – 90% SOC. Out of these 9 pulses, 4 pulses were used to estimate parameters and are called inducing points, and the rest 5 points are used for validation. In this study, the identified inducing points are 10%, 30%, 60%, and 90% SOC. Parameter Identification was done at the inducing points using regression analysis for all the cells. Gaussian Process Regression was then used for parameter estimation at other SOCs and temperatures for the three cells.

Figure 3.4 shows the GPR prediction for ECM parameters for Cell 2. The estimates at 10%, 30%, 60%, and 90% SOC levels, denoted by red points are the inducing points, that are used to get mean prediction (- green curve) at remaining SOC points. The shaded blue region is 95% CI ($\pm 2\sigma$) alongside ground truth validation data, denoted by blue points.
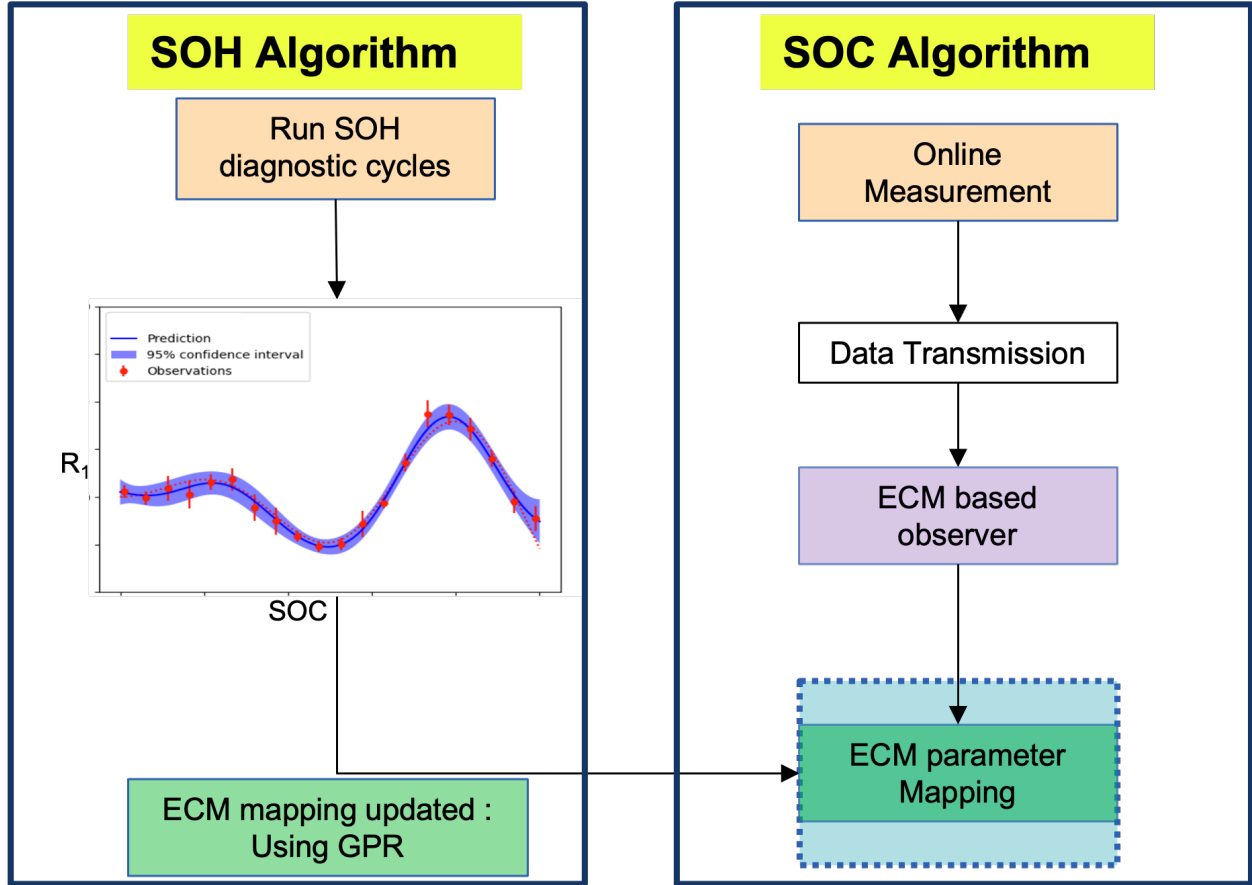
Figure 3.2: Joint SOC and SOH algorithm

Using GPR, we obtain the mean parametric space and $\pm 2\sigma$ confidence interval (CI). The mean GPR maps of cells are taken as the ECM maps of the cells under study. Figure 3.5 shows the parameter maps obtained for the three cells at 25°C.

SOC/SOH Validation

The framework of interval observer in [6], is experimentally validated in this section. The main idea of the interval observer in [6] is the estimation of state intervals, for a system with uncertain parameters and initial conditions. In this validation study, we validate the work in [6], where the battery system is modeled by an ECM with 1RC pair. The states of the system $x(t)$ are $[SOC, V_c(t)]$.

The state interval estimates (based on ECM) of a heterogeneous battery pack $\overline{x}(t)$ and $\underline{x}(t)$ are obtained using the following assumptions:

1. Parametric uncertainty bound is known: $\underline{\theta} \le \theta(t) \le \overline{\theta}(t)$. θ is parameters of the model
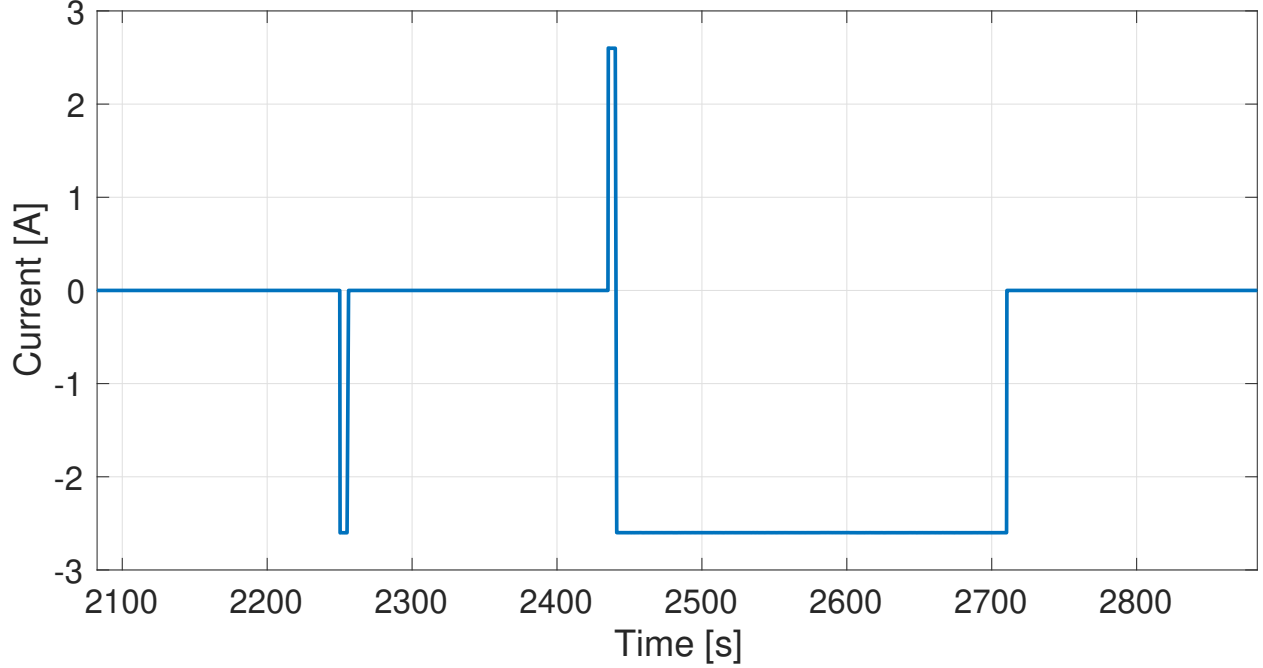
Figure 3.3: Diagnostic current pulse

    i.e., $[R_0, R_1, C, Q]$

2. Initial condition bound at the start of cycle is known: $\underline{x_0} \leq x_0 \leq \overline{x_0}$

3. External measurements about min, max of voltage and current is available: $y_{measured}(t) = [I(t), \max V(t), \min V(t)]$

    The state intervals for the ECM system are obtained, by first converting the nonlinear model dynamics into a partial-linear form using Lie's derivatives. Interval observer design is then built by applying lemma mentioned in [6]. The following is main preposition [6] for obtaining interval estimates:

$$\dot{\overline{\xi}} = (A_0 - \overline{L}H)\overline{\xi} + (\overline{\delta A}^+ \overline{\xi}^+ - \underline{\delta A}^+ \overline{\xi}^- - \overline{\delta A}^- \xi^+ + \underline{\delta A}^- \underline{\xi}^-) + \overline{b}(t) + \overline{L}y + |\overline{L}|V \tag{3.1}$$

$$\dot{\underline{\xi}} = (A_0 - \underline{L}H)\underline{\xi} + (\underline{\delta A}^+ \underline{\xi}^+ - \overline{\delta A}^+ \underline{\xi}^- - \underline{\delta A}^- \overline{\xi}^+ + \overline{\delta A}^- \overline{\xi}^-) + \underline{b}(t) + \underline{L}y + |\underline{L}|V \tag{3.2}$$

    Where $A^+ = \max(0, A)$, $A^- = A^+ - A$, $x^+ = max(0, x)$, $x^- = x^+ - x$ and L is the observer gain selected. The details of the procedure for constructing A_0, δA, b, L, including the mathematics behind obtaining equations above, can be found in [6].
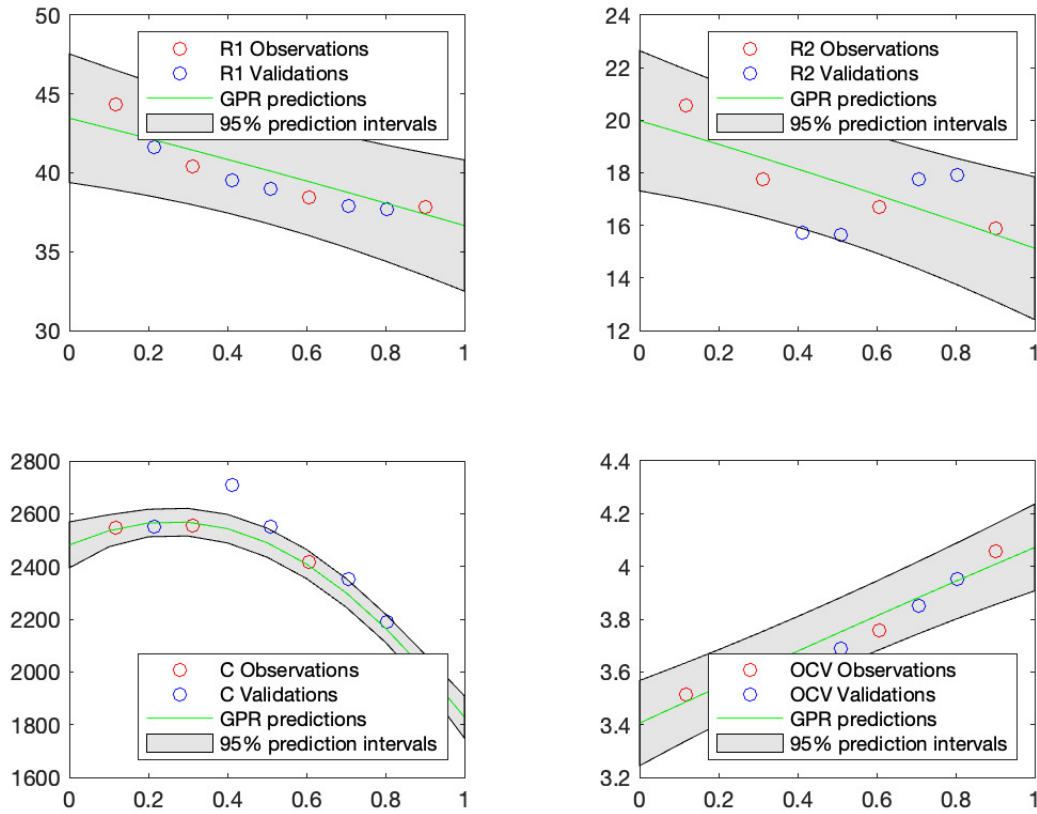
Figure 3.4: GPR parameter prediction for Cell 2
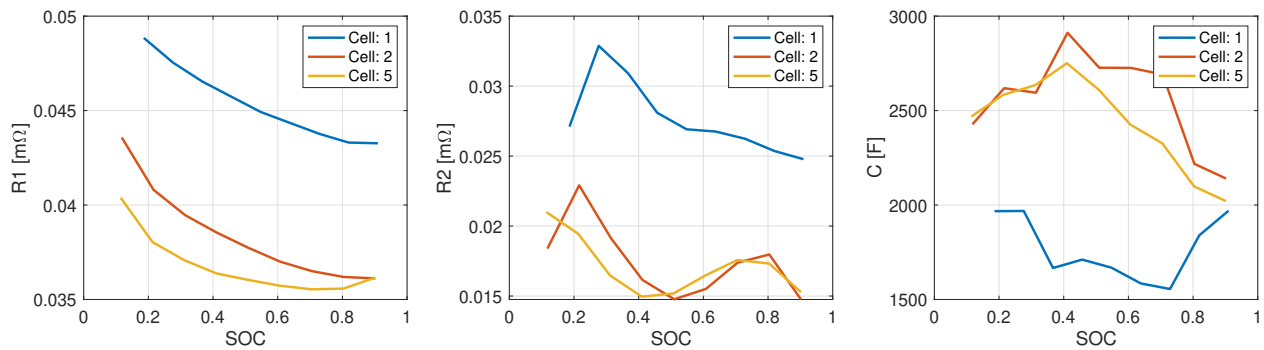
Figure 3.5: ECM parameter maps for Cell 1, Cell 2, and Cell 5

Experiment Performed

The battery module with 3 cells in series was cycled with a constant current and a modified UDDS drive cycle. The current and the voltage for the battery pack is shown in Figure 6.

The Ambient temperature was kept constant at 25°C.
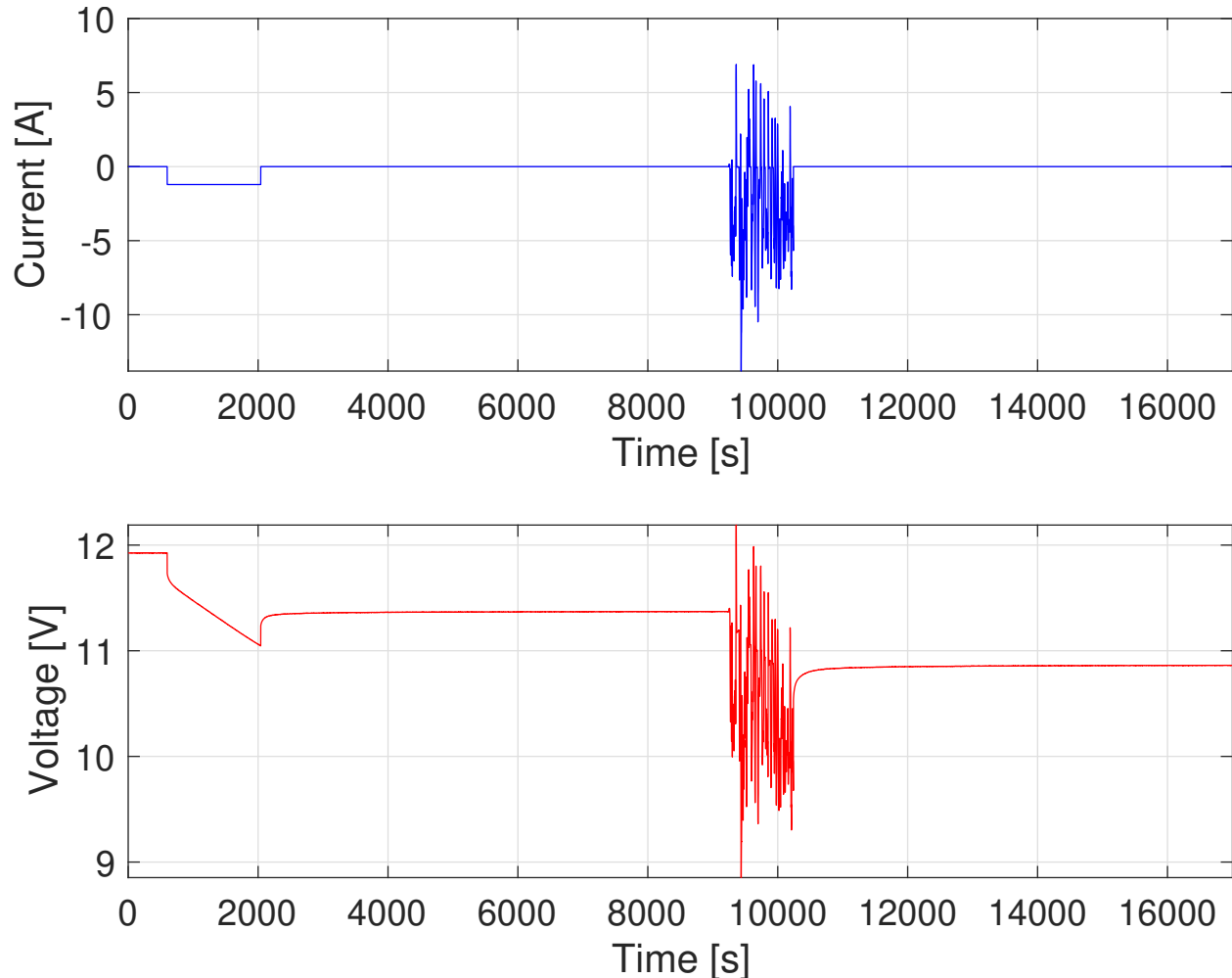
Figure 3.6: Current and voltage evolution of the 3-cell battery pack

Figure 3.6 shows the voltage evolution of the individual cells respectively. It can be observed that due to heterogeneity in the cell, the voltage response of the cells is not identical.

The algorithm postulated in [6], enhances performs SOC estimation by using adaptive parameter bounding. We validated the algorithm in this section by using the interval SOC algorithm both with and without the adaptive bounding.

In this section, we first validate the SOC algorithm without the adaptive bounding. This means that the parameter uncertainty bounds that the SOC algorithm assumes are fixed and are taken as the min/max value of parameters estimated for the three cells across all the SOCs. This approach is conservative and is expected to not give tight SOC intervals.

The green circles in Fig. 3.8 highlight the $[\underline{\theta(t)} \quad \overline{\theta(t)}] = [\underline{\theta} \quad \overline{\theta}]$ used in the algorithm.
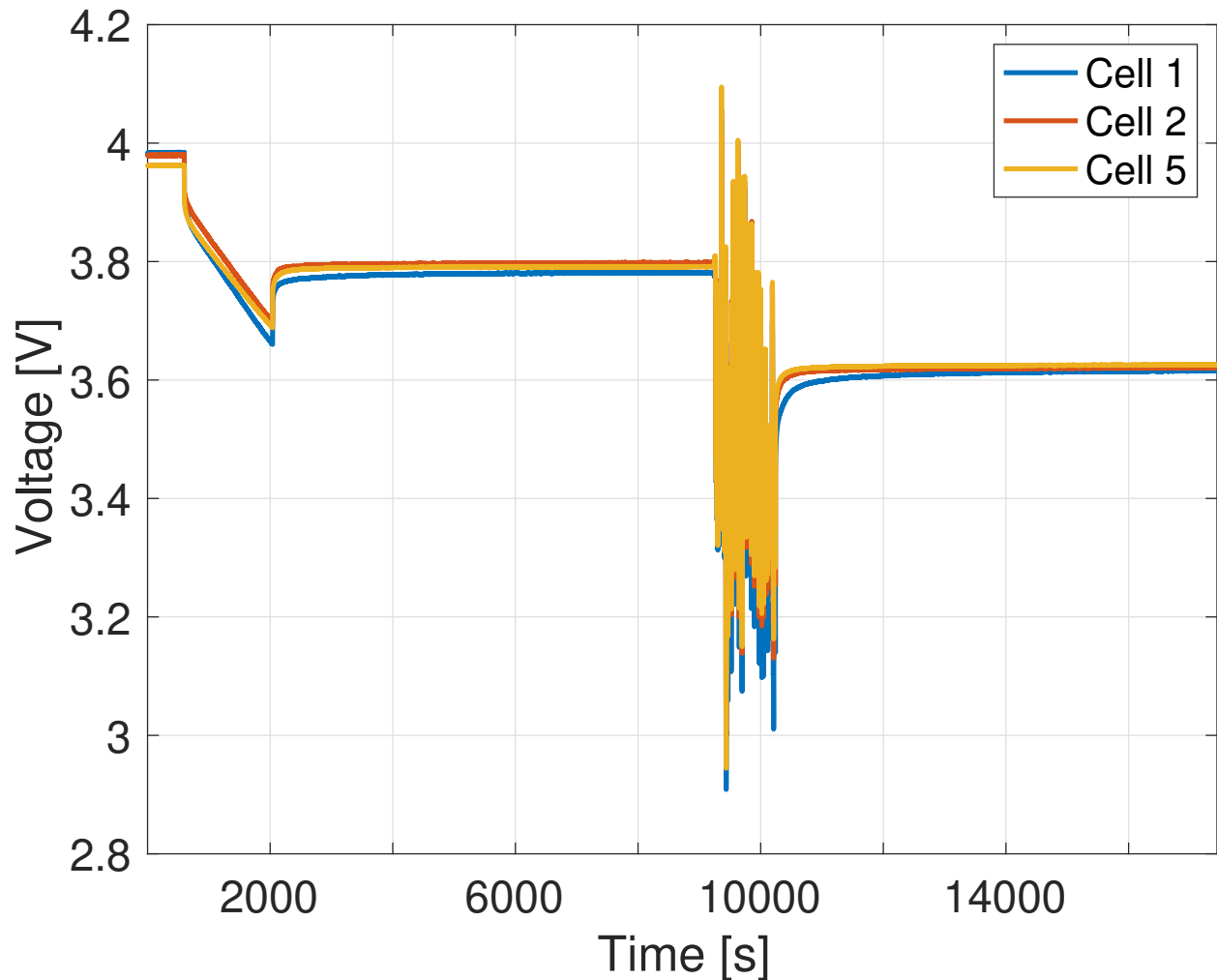
Figure 3.7: Voltage evolution of Cell 1, Cell 2, and Cell 5 respectively

Figure 3.9 shows the result of the interval SOC algorithm. The solid-colored lines are the "true SOC" of the three cells in investigation and the dotted colored lines are the estimates of the interval SOC observer. It can be observed that the interval SOC observer fails to bind the "true SOC" of the cells. To understand the poor performance of the interval observed in estimating SOC bounds, we further investigate how the cell behavior changes as the cell ages.

Inaccuracy observed: Uncertainty in OCV

The algorithm in [6] assumes that as the cell ages the cell parameters $[R_1, R_2, C, Q]$ change as observed in Fig. 3.5, but does not consider any change/shift in the OCV-SOC.

To check the validity of the assumption that OCV-SOC does not change with aging, we
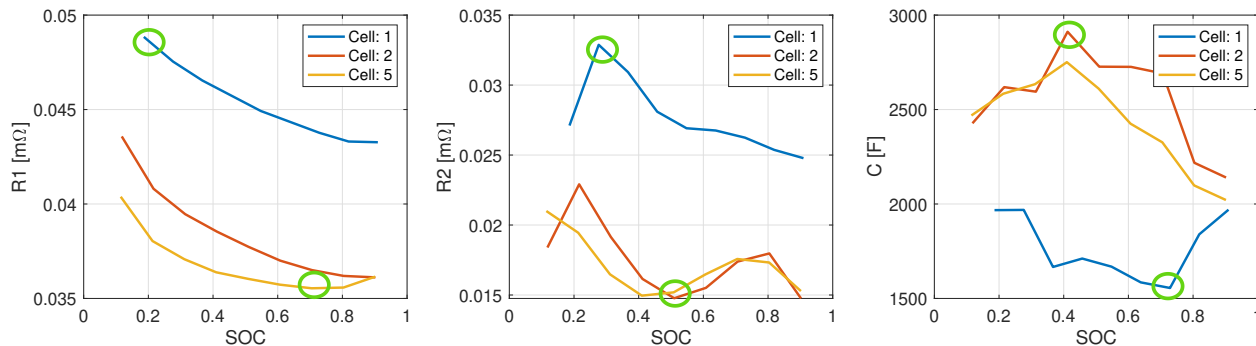
Figure 3.8: ECM parameter bounds without adaptive parameter bound

performed OCV characterization tests (C/50 charge and discharge) on the three cells under investigation. Figure 3.10 shows the Voltage-Capacity curve of the three cells.

Figure 3.11, shows how the OCV vs SOC curve comparison of the most aged (Cell 1) and least aged (Cell 5) cell. The solid lines are the OCV curve obtained using the C/50 discharge test, while the dotted line is the OCV curve obtained using the C/50 charge test.

OCV-SOC curves obtained by just the C/50 discharge test are considerably different for Cell 1 and Cell 5. To highlight the significance of this change in the OCV curve, we obtain the SOC at 3.65V (open-circuit voltage) using the two curves. The horizon line in Fig. 3.11, corresponds to 3.65 V. The OCV-SOC inverse relationship is used to obtain corresponding SOCs. It can be observed from Fig. 3.11, that the SOC corresponding to 3.5 V obtained using the two curves is significantly different and would result in absolute error in SOC as high as 10%. This problem caused by the shift in the OCV curve is worsened when we look at the difference in the OCV curve obtained via charge and discharge, as shown in Fig. 3.11.

This highlights the necessity of including uncertainty in the OCV-SOC map in the interval SOC observer.

Modification to the interval algorithm: OCV uncertainty inclusion

This section describes the modification done to the interval observer algorithm to include the OCV uncertainty caused by the aging of cells. The work in this section is to just highlight the necessary modification done to the algorithm and not to get to the details of the algorithm mentioned in [6].

In [6], the ECM model, the state dynamics, and the output equation can be represented by a system of ODE:
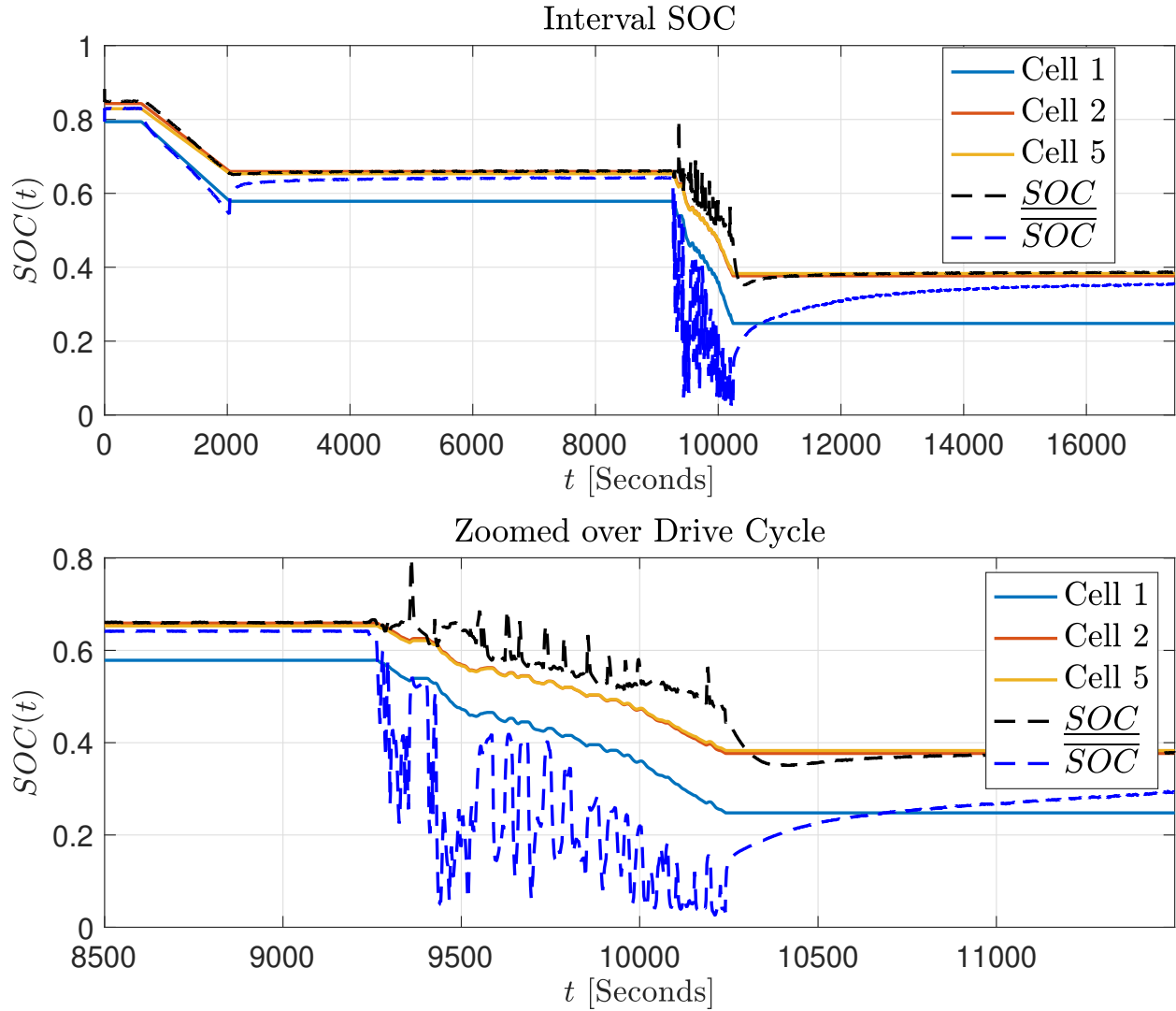
Figure 3.9: Interval Observer performance for 3-cell battery pack

$$\dot{x}_1(t) = \frac{1}{Q}I(t), \tag{3.3}$$

$$\dot{x}_2(t) = -\frac{1}{R_2}\,x_2(t) + \frac{1}{C}\,I_k(t), \tag{3.4}$$

$$y(t) = OCV(x_1(t)) - x_2(t) - R_1 I(t), \tag{3.5}$$

x_1 and x_2 are the state of the system, and system (3.3 - 3.5) has uncertainty in its
parameter R_1, R_2, C, Q.
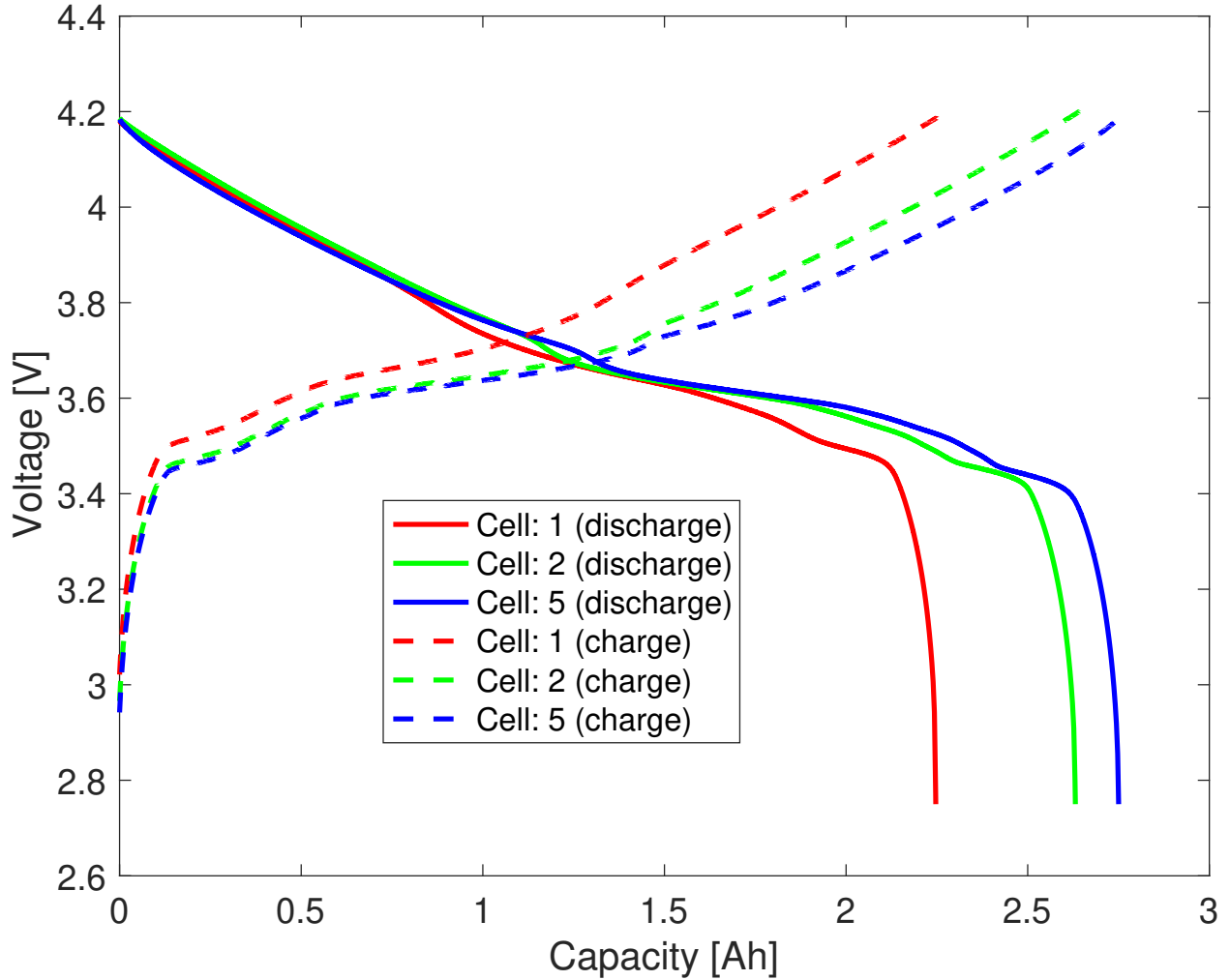
Figure 3.10: Voltage vs Capacity for Cell 1, Cell 2, and Cell 5

$$x = \begin{bmatrix} x_1 \\ x_2 \end{bmatrix} = \begin{bmatrix} SOC \\ V_c \end{bmatrix} \tag{3.6}$$

As shown in [6], the system (3.3 - 3.5) is a locally observable non-linear system that can
be transformed to a partial linear form with a linear output map, using Lie's algebra. Once
the system is transformed to a partial linear system, interval observer design for a Linear
Time invariant(LTI) system [6] can be used to design the state interval observer for SOC.

The transformed coordinates given by Lie's algebra are:

$$\Phi(x) = \begin{bmatrix} \xi_1 \\ \xi_2 \end{bmatrix} = \begin{bmatrix} OCV(x_1) + x_2 \\ -\tau_0 x_2 \end{bmatrix} \tag{3.7}$$
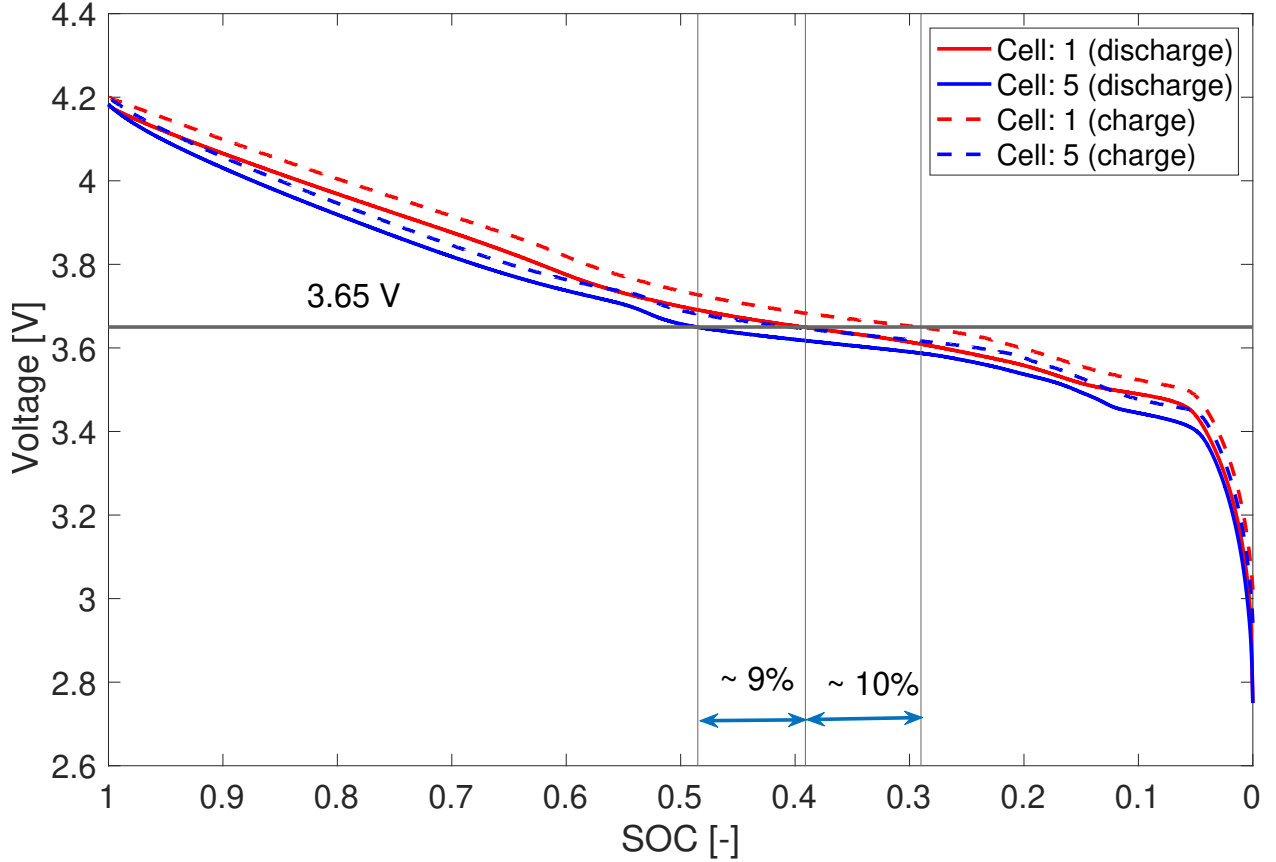
Figure 3.11: OCV-SOC (charge/discharge) for Cell 2 and Cell 5

Using the transformed coordinates, the non-linear system with parametric uncertainty
(3.3 - 3.5) transforms to the following partial-linear system of the form.

$$\dot{\xi}_k = A_0\xi_k + \delta A\left(\theta_k\right)\xi_k + b\left(\xi_k, \theta_k, u\right) \tag{3.8}$$

$$V_k = H\xi_k + \delta h\left(\theta_k\right)u \tag{3.9}$$

where

$$A_0 = \begin{bmatrix} 0 & 0 \\ 0 & -\tau_0 \end{bmatrix}, \; \delta A(\theta_k)_+ = \begin{bmatrix} 0 & \frac{\delta\tau_k}{\tau_0} \\ 0 & \delta\tau_k \end{bmatrix}, \; b(\xi_k, \theta_k) = \begin{bmatrix} \frac{1}{Q_k}\phi(\xi_{k,1} + \frac{\xi_{k,2}}{\tau_0}) + \frac{1}{C_k} \\ -\frac{\tau_0}{C_k} \end{bmatrix} I(t),$$

$$H = [1 \quad 0], \; \delta h(\theta_k) = R_{1,k}$$

$\phi(.) = \frac{dOCV}{dx_{k,1}}[OCV^{-1}(.)]$

The interval observer on the transformed partial linear system proposed in [6] is given
by eq (3.1 - 3.2). It can be observed that the uncertainty in OCV, has a limited impact on
the interval observer structure of the transformed system (3.1 - 3.2). The OCV uncertainty

in (3.8) appears in b, which can be included in the interval observer structure easily by modifying the bounding function for b.

$$\overline{b} = \begin{bmatrix} \frac{1}{Q}\overline{\phi} + \frac{1}{\overline{C}} \\ -\frac{\tau_0}{\overline{C}} \end{bmatrix} I, \ \underline{b} = \begin{bmatrix} \frac{1}{\overline{Q}}\underline{\phi} + \frac{1}{\overline{\underline{C}}} \\ -\frac{\tau_0}{\underline{C}} \end{bmatrix} I,$$

The main impact of OCV uncertainty is on coordinate transformation. The inverse transformation of $\Phi(.)$ is used obtain the original system dynamics (3.3 - 3.5). This is done as follows:

$$\Phi^{-1} = \begin{bmatrix} x_1 \\ x_2 \end{bmatrix} = \begin{bmatrix} OCV^{-1}(\xi_1 + \frac{1}{\tau_0}\xi_2) \\ -\frac{1}{\tau_0}\xi_2 \end{bmatrix} \tag{3.10}$$

As OCV-SOC maps of the cells are different, the OCV^{-1} mapping function gets the bounds of $x(t)$.

Without OCV uncertainty:

$$\overline{x_1} = OCV^{-1}_{Cell5}(\overline{\xi_1} + \frac{1}{\tau_0}\overline{\xi_2}) \tag{3.11}$$

$$\underline{x_1} = OCV^{-1}_{Cell1}(\underline{\xi_1} + \frac{1}{\tau_0}\underline{\xi_2}) \tag{3.12}$$

Modified transformation: With OCV uncertainty:

$$\overline{x_1} = OCV^{-1}(\overline{\xi_1} + \frac{1}{\tau_0}\overline{\xi_2}) \tag{3.13}$$

$$\underline{x_1} = OCV^{-1}(\underline{\xi_1} + \frac{1}{\tau_0}\underline{\xi_2}) \tag{3.14}$$

The upper bound of $\overline{x_1}$ is obtained by using the OCV inverse function of the least aged cell (Cell 5), while $\underline{x_1}$ is obtained by using the OCV inverse function of the most aged cell (Cell 1).

SOC/SOH validation incorporating OCV uncertainty

The modified interval observer algorithm is validated with experimental data. We first validate the SOC algorithm without the adaptive bound mentioned in [6]. Hence parameter uncertainty bounds that the SOC algorithm are taken as the min/max value of parameters estimated for the three cells across all the SOCs, highlighted by the green circles in Fig. 3.8.

Figure 3.12, shows the performance of the interval observer with OCV uncertainty incorporation. It can be observed that results in Fig. 3.12 are better in terms of having bounded
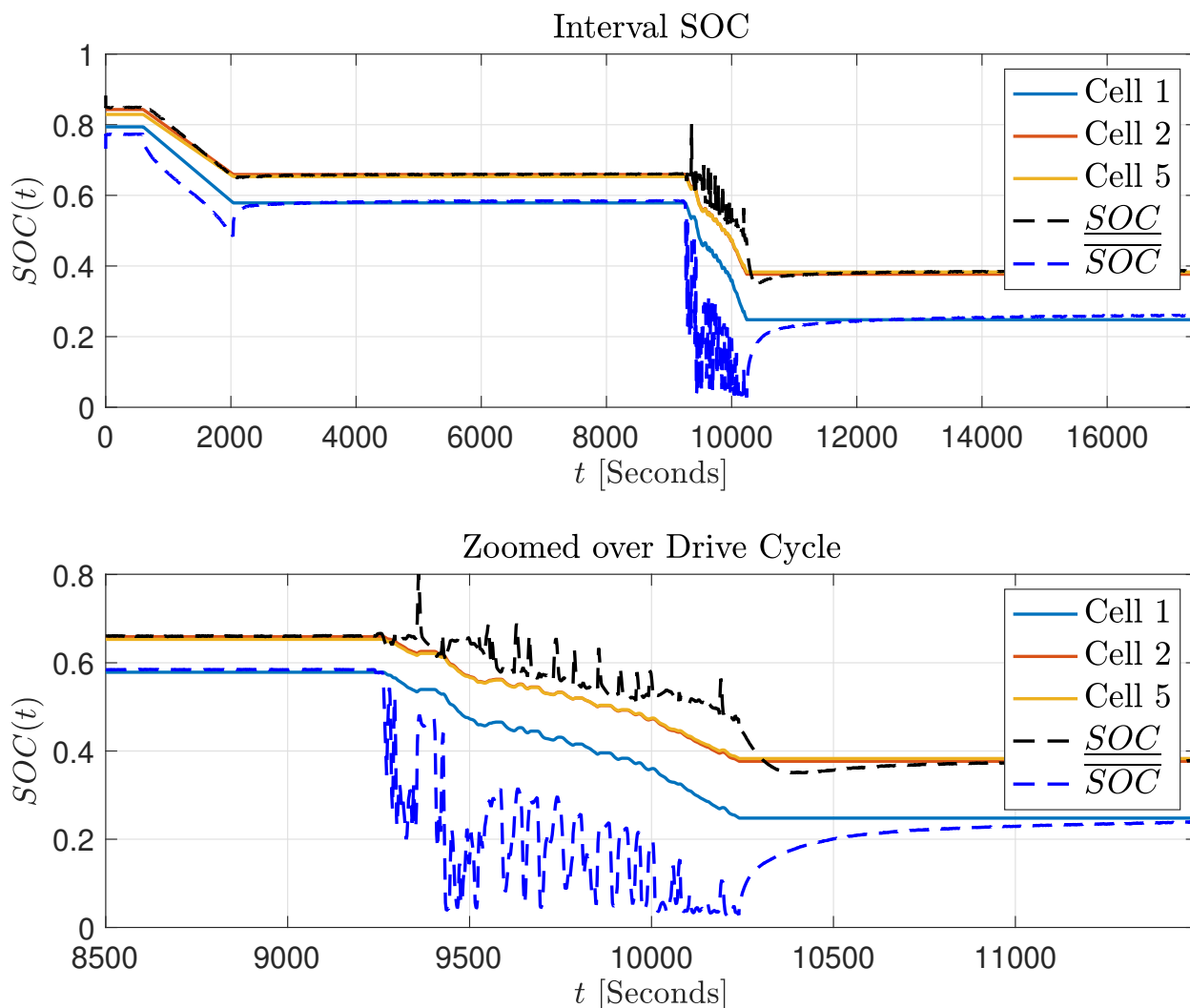
Figure 3.12: Interval Observer with OCV uncertainty inclusion for 3 cell battery pack

interval state estimates, compared to results in Fig. 3.9. The interval observer does not produce tight interval estimates in this validation.

In the above validation, the three cells in the investigation have a high degree of heterogeneity in term in terms of their capacities and parameter estimates. To see if the tightness of interval estimation becomes better by reducing the degree of cell heterogeneity, interval estimation was also done with 2 cells (Cell 2 and Cell 5).

Figure 3.13 shows the algorithm performance with two cells using experimental data and compares it to the algorithm's performance using model data. The model data is obtained by simulating a 1RC - ECM with the parameter maps obtained for the cell shown in Fig. 3.5.
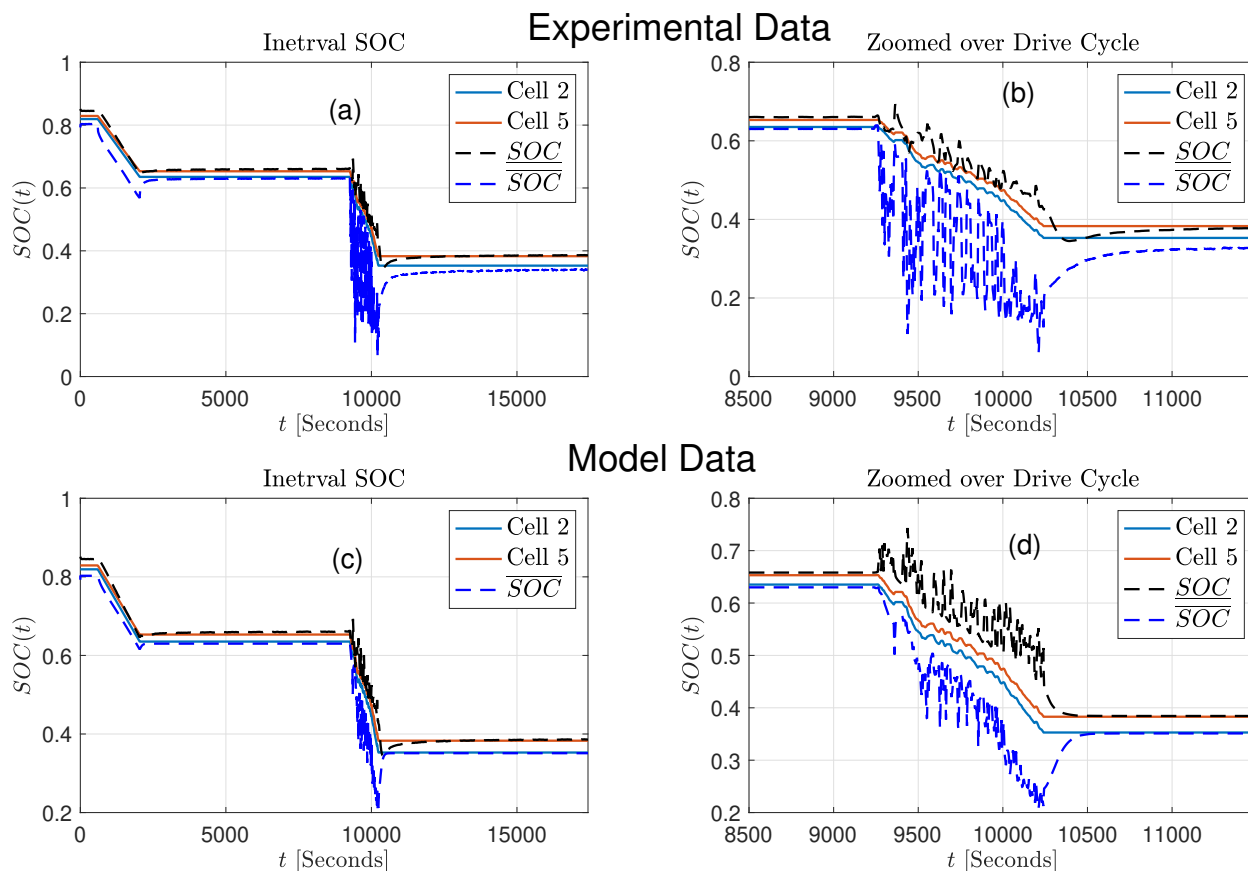
Figure 3.13: Performance of Interval Observer (no adaptive bounding) with OCV uncertainty with model vs experimental data

Figure 3.13 shows the modified interval observer performance with 2 cells (Cell2 and Cell 5). It can be observed that using model data, the algorithm results in bounded intervals at all times, the same is not true with experimental data.

We further test the algorithm performance using adaptive parameter bounding. This is done to check the accuracy of the modified interval algorithm with adaptive bounding and compare it to a model-to-model framework. Adaptive bounding framework was used in [6], to increase tightness of the state interval estimates. Rather than using the worst-case scenarios with maximum parameter uncertainty, the uncertain parameter bounds are updated based on the current estimates of state intervals. This is shown in Fig. 3.14, where the parameter uncertainty bounds in the algorithm are taken from the estimated state intervals highlighted in blue.

Figure 3.15 shows the results of modified interval observer performance with adaptive bounding. Similar to Fig. 3.13, it can be observed that the algorithm results in bounded intervals at all times with model data but performs poorly with experimental data. The

adaptive bounding does increase the performance of the interval estimation algorithm in producing tight-bounded interval estimates when looking at model data. (Fig. 3.13 and Fig. 3.15). However, when using experimental data the algorithm performs poorly both with and without adaptive bounding.
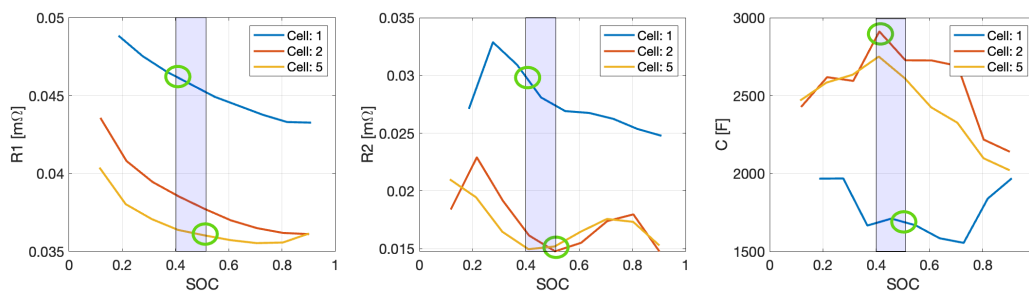
Figure 3.14: ECM parameter bounds with adaptive parameter bound

The main reason for the poor performance of the algorithm in the experimental framework is because of the difference in the model output voltage and the experimental voltage. The accuracy of the observer is dependent on how accurately the model predicts the outputs.

Figure 3.16 compares the voltage $[V_{min}, V_{max}]$ measured experimentally with the model voltage response of the ECM used in above results Fig. 3.13 and Fig. 3.15).

This shows the inaccuracy of the model to predict actual voltage response.

1. Model Limitation: 1 RC ECM is not accurate here. Especially when high magnitude dynamic current profile is involved.

2. Inaccurate in parameter mapping obtained from GPR.

Discussion and Conclusion

Experimental validation is performed in an integrated SOC+SOH validation framework. Three cells in series are used to make a heterogeneous battery pack. Initial experimental validation revealed an unincorporated vital shift in OCV-SOC map of the cell as the cell ages. The modification was done to incorporate OCV uncertainty in the algorithm. Future experimental validation was done using the modified algorithm and the results were compared the model to model framework. The algorithm performs well on a model-to-model framework but the performance on experimental data is poor.

Experimental validation showed that for inclusive and tight bounds, the fitness of the model to experimental data is important. This can be achieved by having a better model e.g., 2RC model. The accuracy of the algorithm also depends on having accurate parameter maps. Using GPR with more training points will help in better estimating parameter maps.
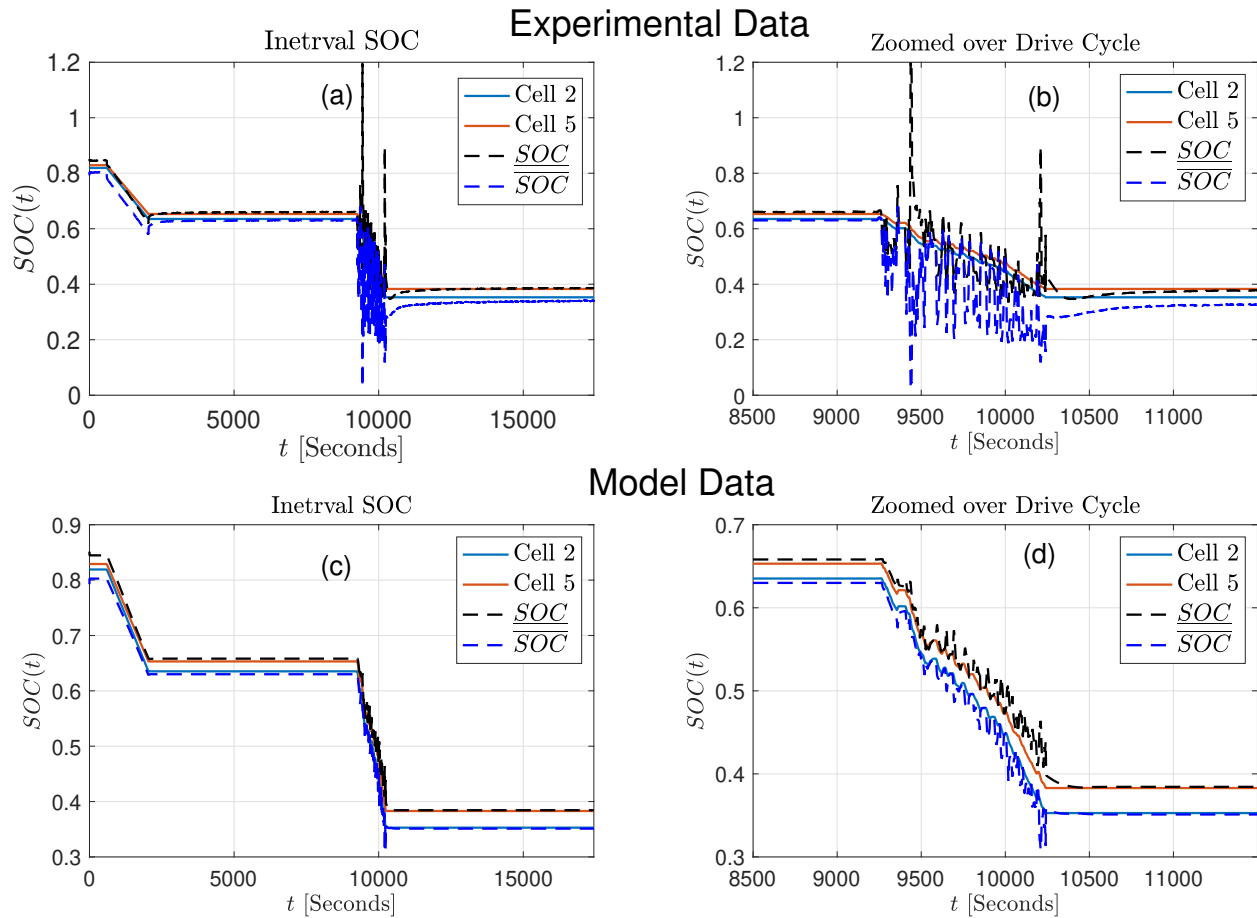
Figure 3.15: Performance of Interval Observer (with adaptive bounding) with OCV uncertainty
with model vs experimental data

3.3 SOP Validation

Objective

In this section, we validate the SOP algorithm presented in [30] experimentally. The work
in [30] defines SOP as the maximum current that can be constantly supplied over a fixed
time horizon without violating any safety constraints. The safety constraints considered in
this experimental validation work are detailed in Table 3.2.

Outline of the experiment

The experiment is performed for a battery with 2 cells in series (Cell 2 and Cell 5). The initial
SOC of the two cells i.e., Cell 2 and Cell 5 are 0.61 and 0.64 respectively. The prediction
horizon for SOP is taken as 120 sec. A section of the modified UDDS cycle is used for the
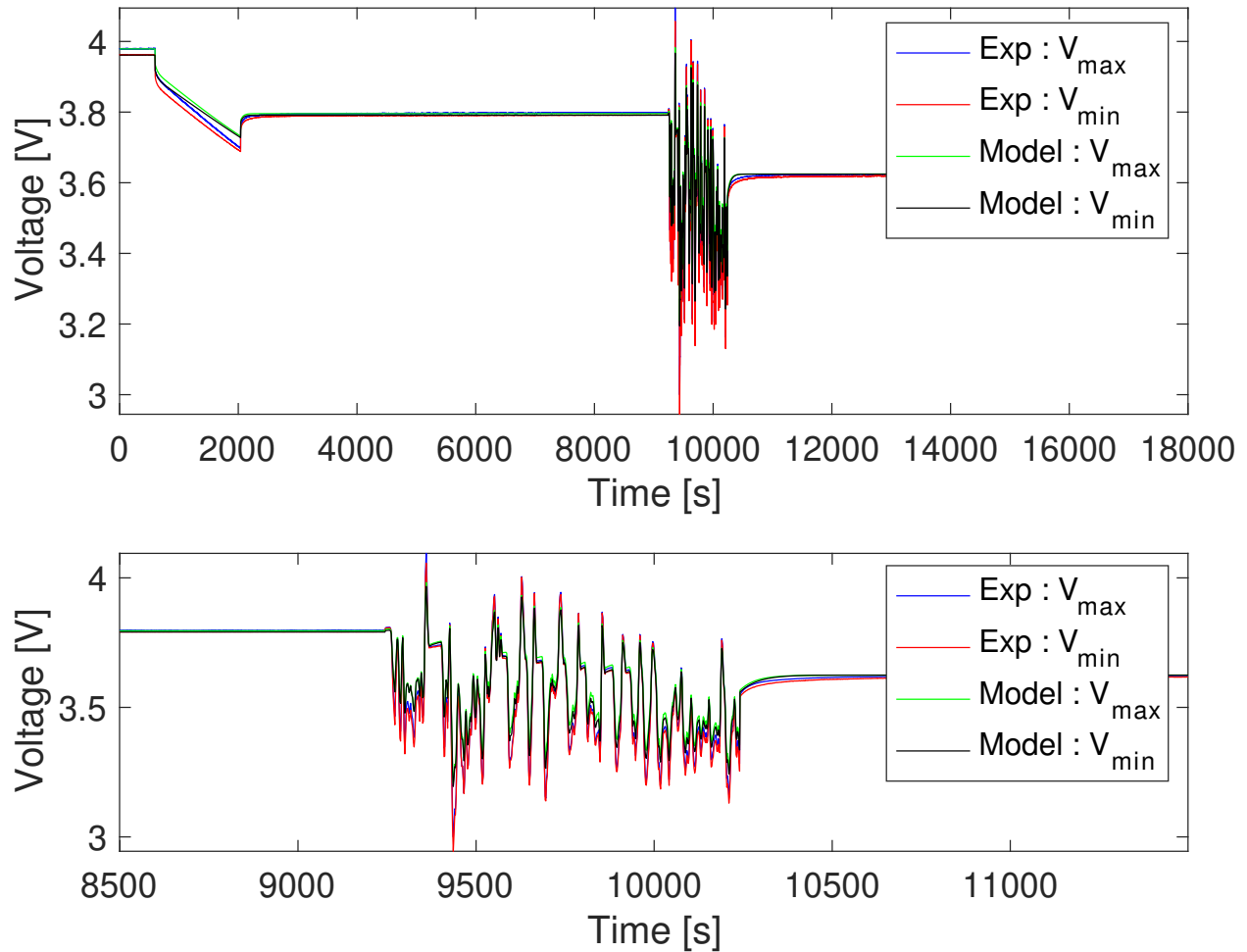
Figure 3.16: Model vs experimental voltage

analysis (Fig. 3.17). The cell is cycled using the modified UDDS cycle, and the SOP is validated periodically every 160 sec. The time instant where SOP is validated is marked by the red cross as shown in Fig. 3.17. We validate discharge SOP in this work.

Hardware-in-loop (HIL) setup is used for SOP validation. The voltage measured V(t) is used to estimate the $[\underline{x(t)} \quad \overline{x(t)}]$ using interval observer, which is used as the initial condition for state uncertainty in the SOP algorithm. As shown in Fig. 3.17, the SOP is validated at 4 points.

The experiment procedure is as follows:

1. Start the experiment: Run the given cycle: (here modified UDDS)

2. At the validation point, estimate the SOP based on $[\underline{x_{0,i}} \quad \overline{x_{0,i}}]$, where i is the index of validation point.

Table 3.2: Experimental SOP safety limits

Constraints	Lower Limit	Upper Limit
#Voltage	3.5V	4.4V
#SOC	0.5	1.0
#Current	10A	10A
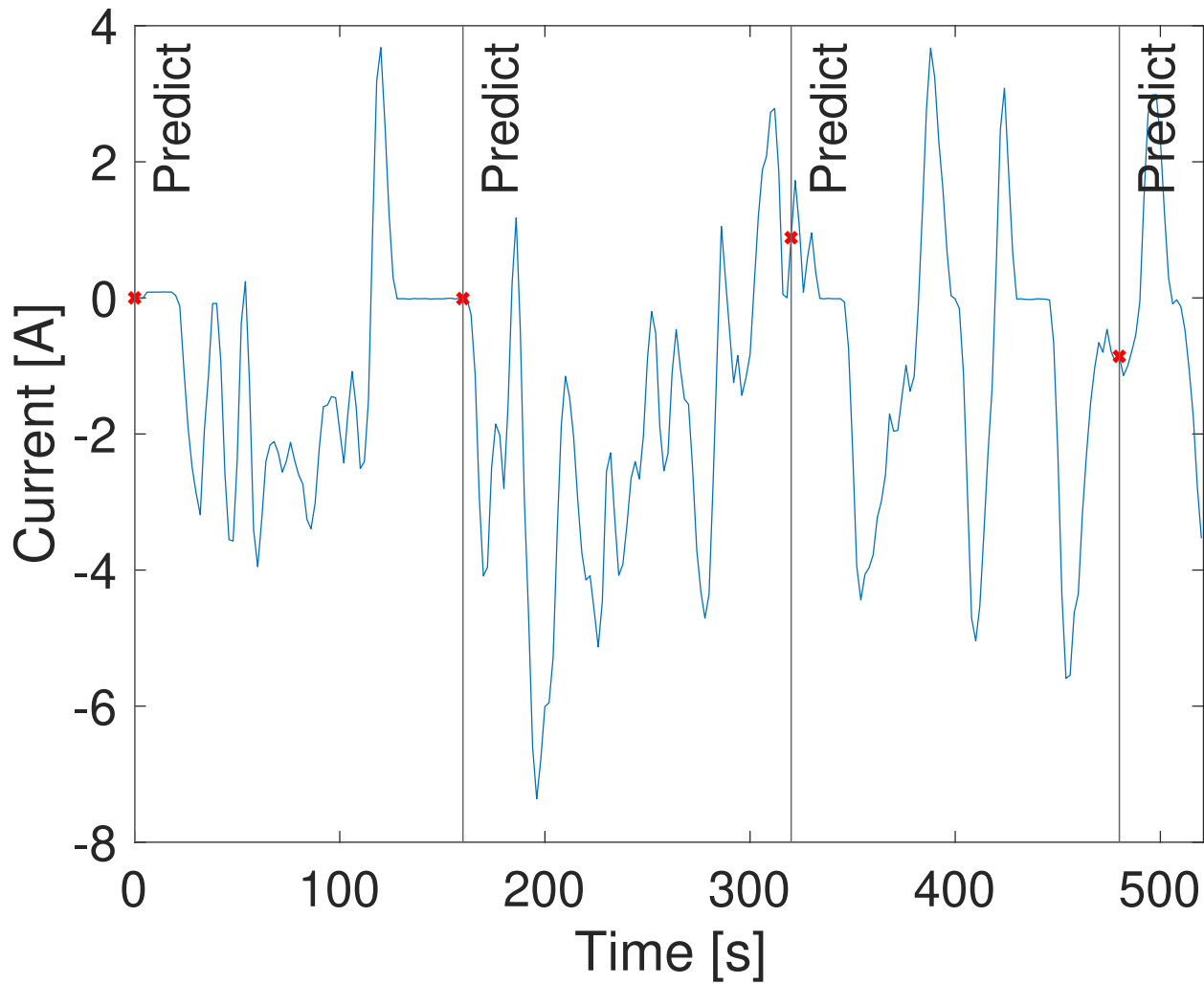
Figure 3.17: Current profile for SOP testing

3. Apply the predicted SOP current pulse at prediction point i

4. Validate SOP at the point: Charge or discharge. (Discharge here)

5. Rest for 60 sec

6. Charge /discharge back to $[\underline{SOC_{0,i}} \quad \overline{SOC_{0,i}}]$

7. Rest for 180 sec

8. Continuing running the cycle (UDDS), till the next prediction point $i = i + 1$ or end of cycle

9. Repeat Step 2 to 8 till i=4

Figure 3.18 shows the SOP validation performed at 4 points when cells are being cycled using the modified UDDS profile. The UDDS cycling is interrupted periodically with SOP validation. At the validation points, cells are discharged with the SOP estimated and then charged back. The resulting current profile with SOP prediction is shown in Fig. 3.18.
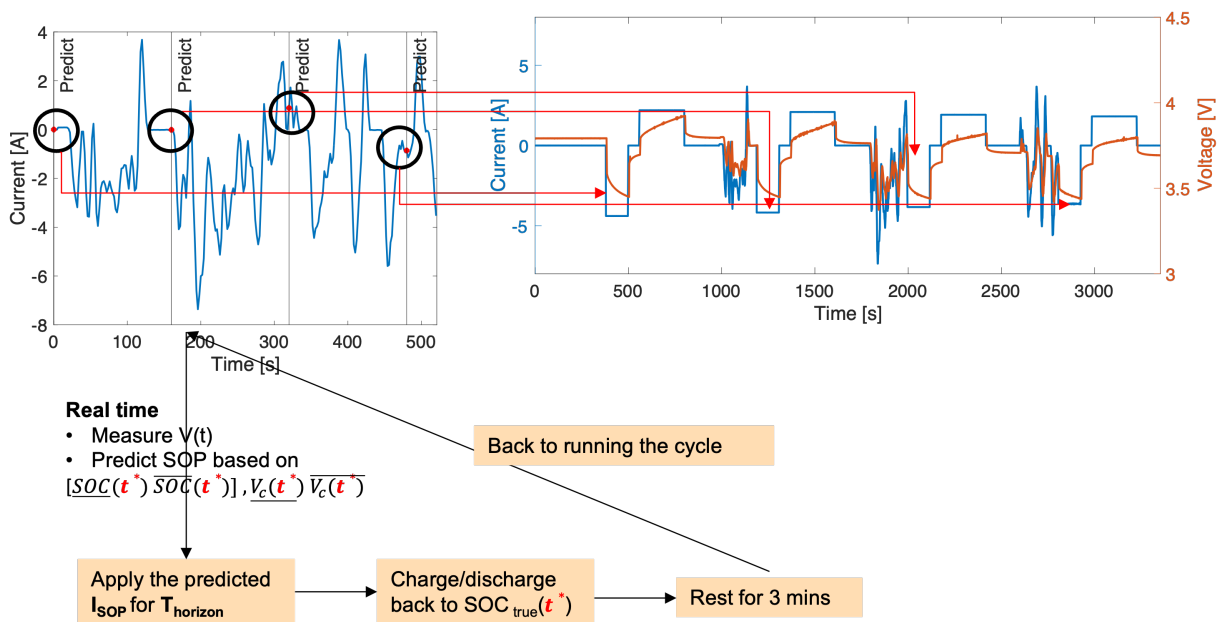
Figure 3.18: SOP Experimental plan outline

Outline of the algorithm

The SOP validation algorithm proposed is integrated with the interval SOC and SOH algorithm. The GPR maps from SOH are the input to both the interval SOC and SOP algorithm. The interval SOC algorithm with adaptive bounding [1] provides bounds of states $[\underline{x(t)} \quad \overline{x(t)}]$. At the point of prediction t=i, the estimated interval state bounds are fed as the initial condition $[\underline{x_{0,i}} \quad \overline{x_{0,i}}]$ for the SOP algorithm. The overall algorithm is shown in Fig. 3.19.

The overall validation algorithm hence becomes an integrated SOH+SOC+SOP algorithm. This validation, hence, will test various inaccuracies coming from:
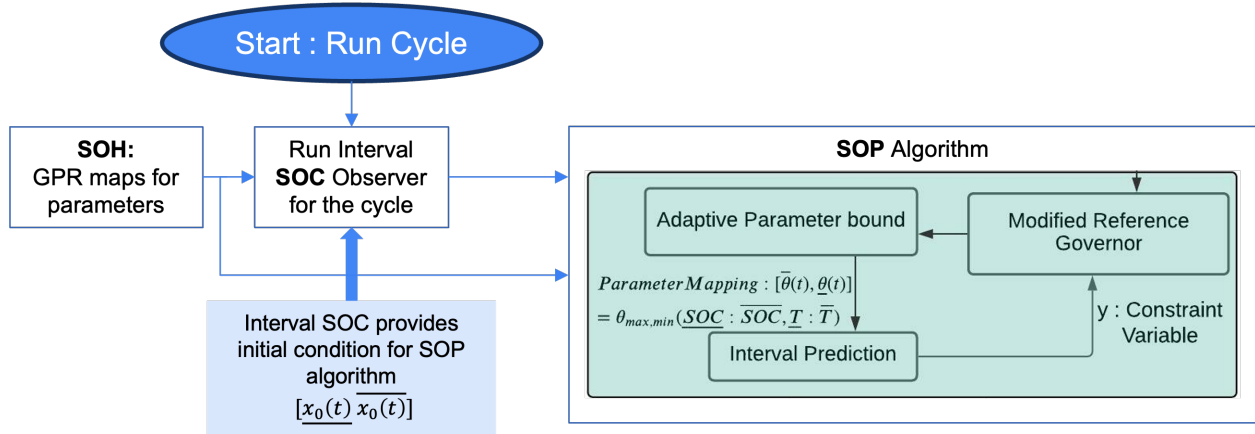
Figure 3.19: Outline of integrated SOC, SOH, and SOP algorithm

1. Error in Interval observer: Causes Inaccurate initial condition input $[\underline{x_{0,i}} \ \ \overline{x_{0,i}}]$ to SOP

2. GPR map inaccuracy: Cause Inaccurate parameter bounds $[\underline{p} \ \ \overline{p}]$ to SOP

3. Interval Prediction error: Inaccuracy in SOP prediction algorithm

4. Model inaccuracy

As detailed in section 3.2, error in interval observer is significant which can result in a high overall error. To this extent, three 3 validation metrics are proposed:

1. Run the SOP with a feed-forward observer: The interval observer in Fig. 3.19, is replaced with a feed-forward observer model on each cell. The feed-forward model provides the uncertainty in the initial condition of the state $[\underline{x_{0,i}} \ \ \overline{x_{0,i}}]$ to the SOP. As a feed-forward model is used here, the hardware in the loop framework is not needed with this approach.

2. Run the SOP with observer on each cell: The interval observer in Fig. 3.19, is replaced with an observer model for each cell. The observer on an individual cell is used to evaluate the uncertainty in the initial condition of the state $[\underline{x_{0,i}} \ \ \overline{x_{0,i}}]$, which is fed to the SOP algorithm.

3. Run the SOP with interval observer: This is the original proposed algorithm in Fig. 3.19.

Different validation approaches

The three different approaches are summarized in Table 3.3. The table also details the main sources of error in the three approaches.

Table 3.3: SOP Experimental Validation approaches

Approach	Validation Plan	Performance check
1	SOP without HIL (replacing interval observer with feed-forward model)	• Model inaccuracy • SOP Interval prediction
2	SOP with HIL (Observer on each cell)	• Observer error • SOP Interval prediction
3	SOP with HIL (Interval Observer)	• Observer error • SOP Interval prediction

Results and Discussion

The validation is done with the three different approaches proposed. As mentioned before, 2 cells (Cell 2 and Cell 5) are used in this validation. In all three validation approaches the initial SOC of the two cells i.e., Cell 2 and Cell 5 were at 0.61 and 0.64 respectively. The performance of the algorithm is quantified using the safety constraints used in the algorithm mentioned in Table 3.3. At each validation point, at the end of each SOP pulse, we check how far the battery cells are from the safety limits set. The current constraints are never violated in this study, hence from now on, we focus on voltage and SOC limits.

$$V^* = \min\left(V_{Cell2}, V_{Cell5}\right)$$
$$SOC^* = \min\left(V_{Cell2}, V_{Cell5}\right)$$

Figure 3.20, shows voltage (V^*) and (SOC^*) evolution during the SOP discharge pulse. The red points correspond to the start of the pulse and the green points mark the end of the pulse.

The error in the algorithm is quantified as:

• Absolute error

    – $V_{lim} - V_2$

    – $SOC_{lim} - SOC_2$
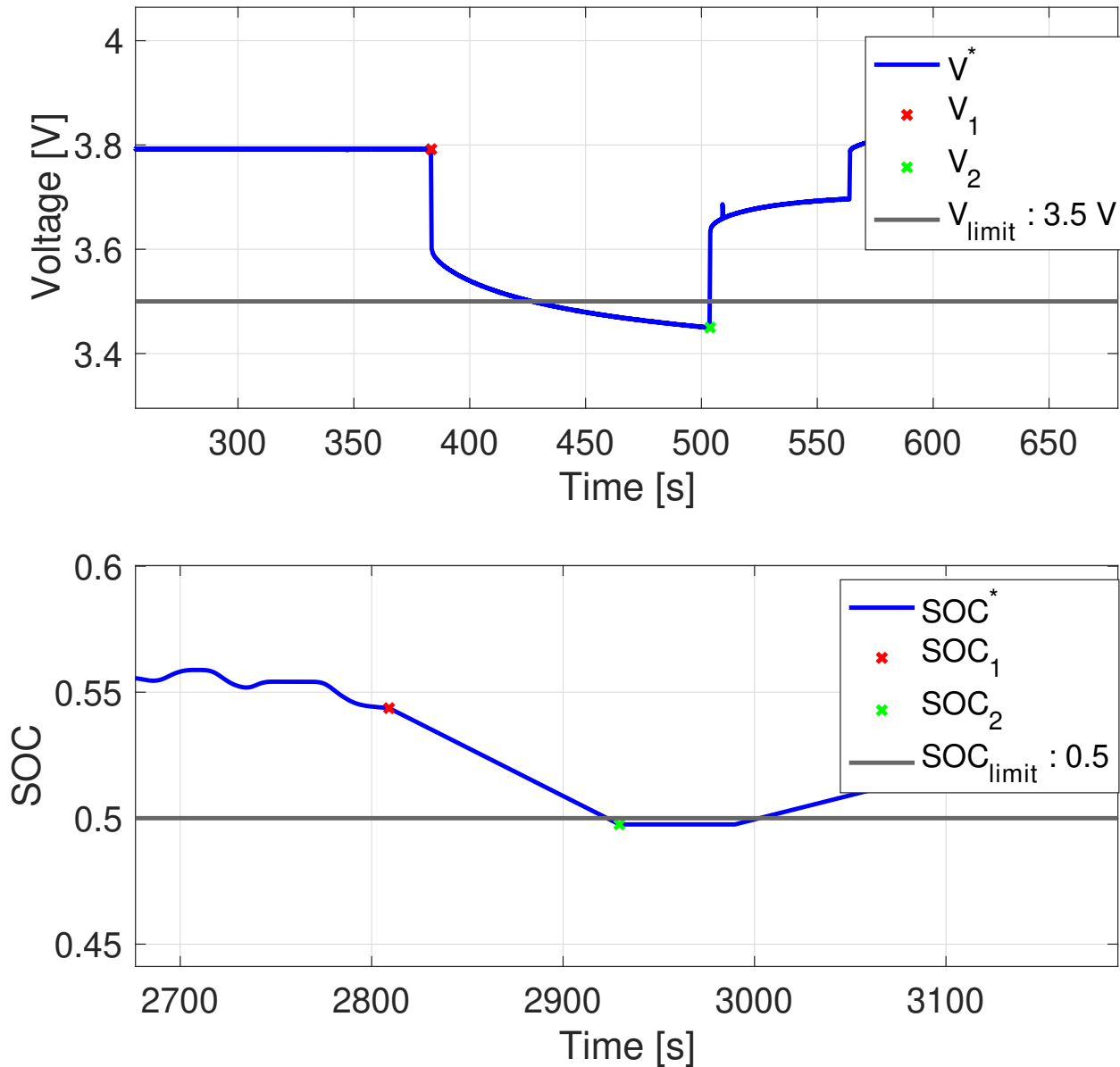
Figure 3.20: Voltage and SOC evolution during SOP testing pulse

- Percentage error

    - $\frac{V_{lim}-V_2}{V_1-V_2} * 100$

    - $\frac{SOC_{lim}-SOC_2}{SOC_1-SOC_2} * 100$

Figure 3.21, Fig. 3.22, Fig. 3.23 show the experimental validation performed using the three approaches. The figures show the current applied and the voltage and SOC evolution

of the two cells used in this study. Voltage and SOC limits used in the algorithm as also plotted for reference. The validation pulses at the 4 points are highlighted in the figures.
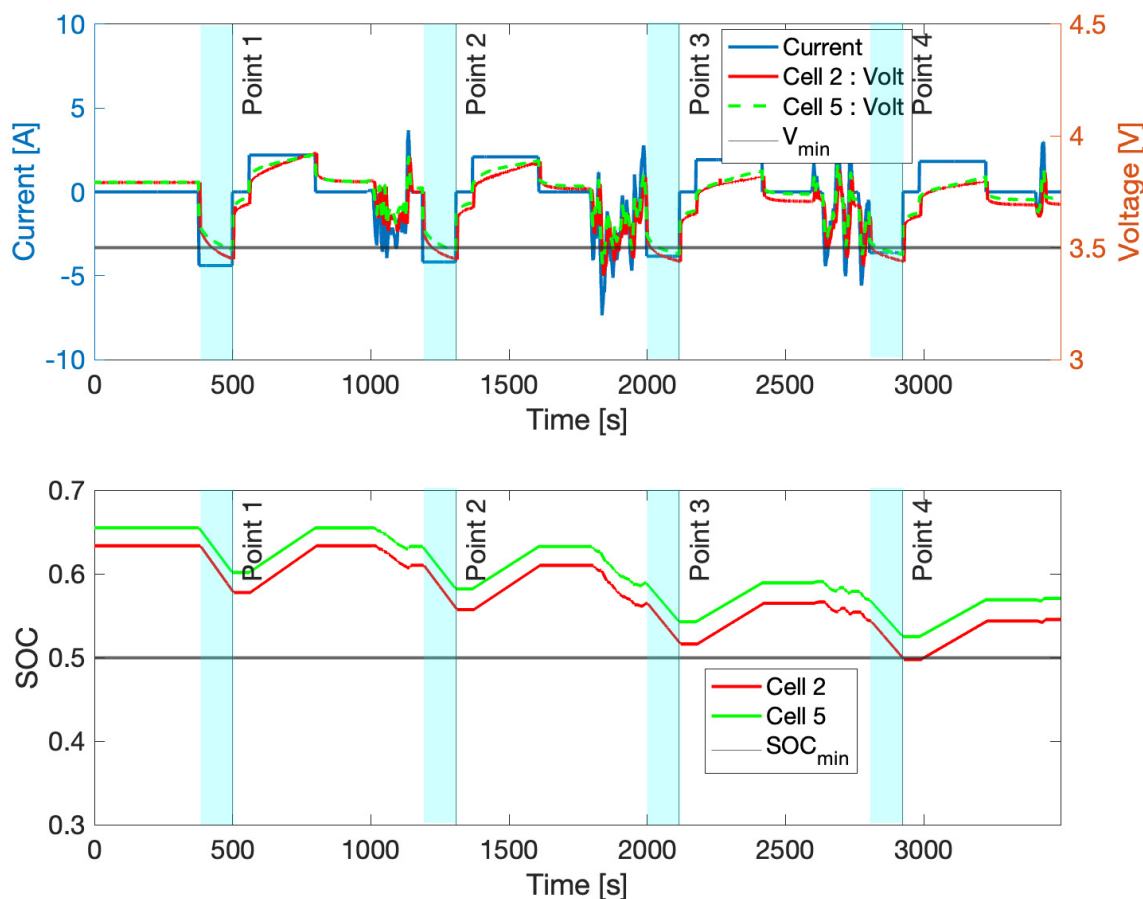
Figure 3.21: SOP Validation Approach 1 with Feedforward observer

Table 3.4, Table 3.5, Table 3.6 summarizes the validation error at each point. At point 1, point 2 and point 3 voltage is the only critical safety limit, while at point 4 both SOC and voltage limits become critical. Hence at points 1, 2, and 3 validation error is only accounted for voltage limit and at point 4 validation error is reported both for SOC and voltage limits.

The performance at point 1 is similar across the three validation approaches. This is expected as point 1 is the initial condition of the whole experiment, and the initial SOC uncertainty is fixed which is [0.61, 0.64]. Hence at point 1, the SOP algorithm performance is independent of any observer. At point 2 and point 3, it is observed that approach 3, with interval observer, performs better than approaches 1 and 2. However, at point 4, the performance of approach 3 is very poor. At point 4, approach 3 predicts 0A discharge SOP,

Table 3.4: SOP Validation with Approach 1

Error	Point 1	Point 2	Point 3	Point 4
Abs error $\Delta V : V^* - V_{limit}$	-0.0502	-0.0526	-0.0612	-0.0609
% Voltage Error	-14.67	-17.27	-23.71	-32.20
Abs error $\Delta SOC : SOC^* - SOC_{limit}$	-	-	-	-0.002
% SOC Error	-	-	-	-5.35
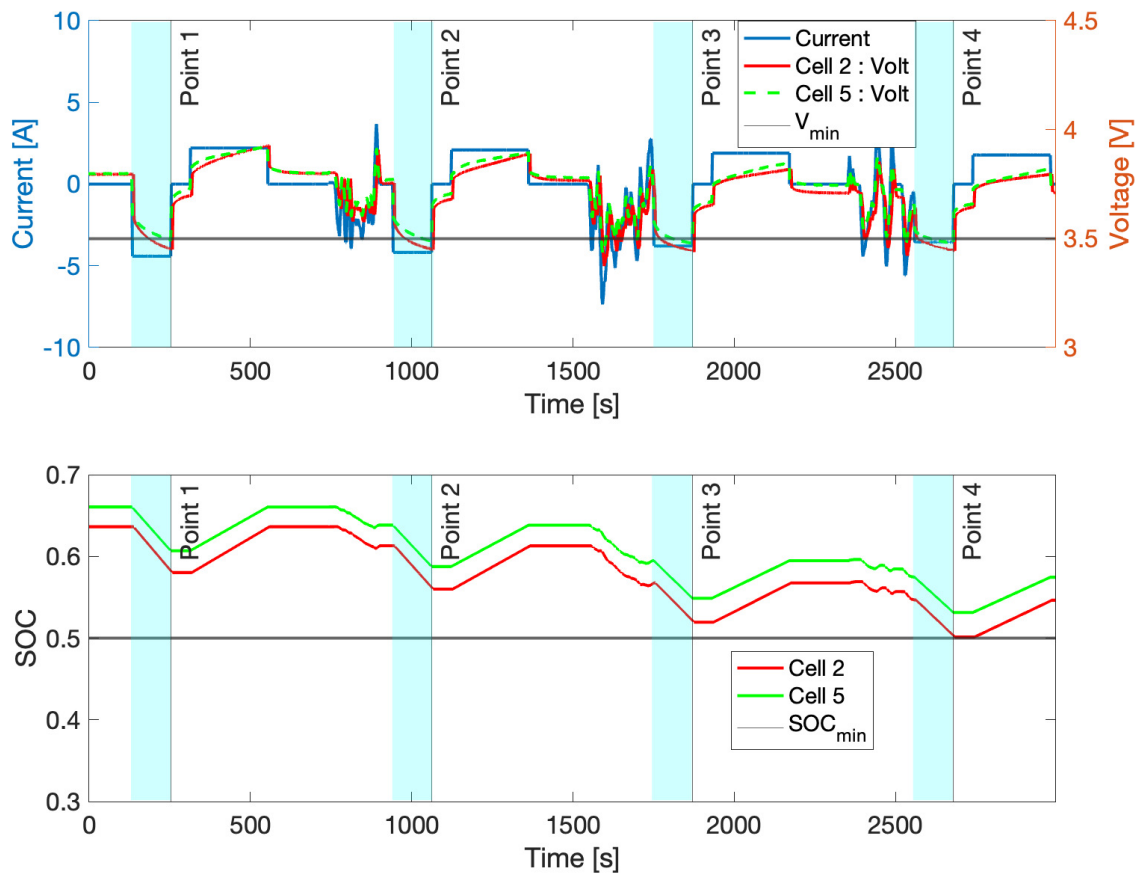
Figure 3.22: SOP Validation Approach 2 with Luenberger observer on each cell

which results in no pulse at point 4 as can be seen in Fig. 3.23. Overall, across all 4 points, it is observed that approach 2 results in better performance of the SOP algorithm. To investigate the difference in performance for approaches 2 and 3, the accuracy of the observers at points 2, point 3, and point 4 to provide initial conditions to SOP is checked.

Table 3.5: SOP Validation with Approach 2

Error	Point 1	Point 2	Point 3	Point 4
Abs error $\Delta V : V^* - V_{limit}$	-0.0496	-0.0504	-0.0576	-0.055
% Voltage Error	-14.56	-16.42	-22.15	-29.96
Abs error $\Delta SOC : SOC^* - SOC_{limit}$	-	-	-	-0.0013
% SOC Error	-	-	-	2.85
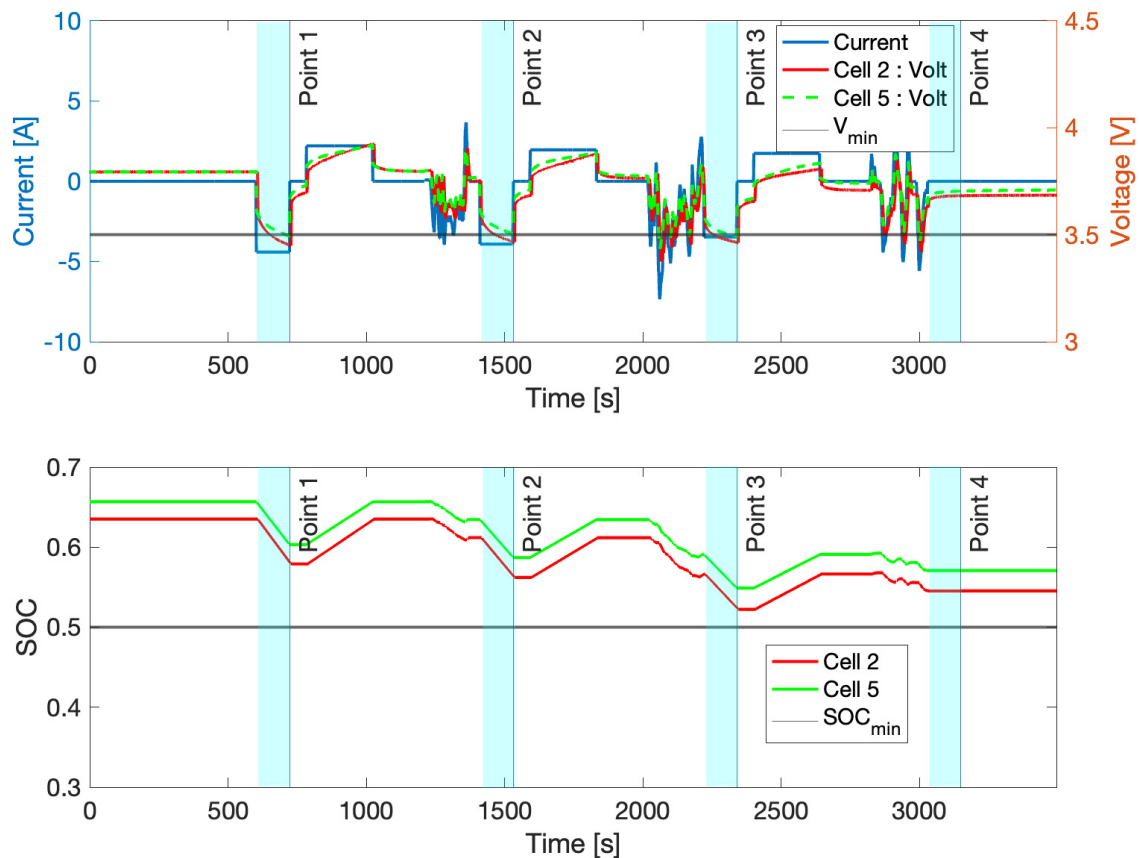
Figure 3.23: SOP Validation Approach 3 with interval observer

Figure 3.24 shows the observed SOC using Luenberger observer on each cell and Figure
3.25 shows the observed SOC intervals using interval observer. Following the discussion
in section 3.2, the interval observer poorly performs in estimating SOC intervals at most
points. Coincidentally at point 2 and point 3, the interval SOC estimates are good, thereby
providing good performance. Whereas at point 4, the interval estimates provide poor initial

Table 3.6: SOP Validation with Approach 3

Error	Point 1	Point 2	Point 3	Point 4
Abs error $\Delta V : V^* - V_{limit}$	-0.0505	-0.0338	-0.0369	0.1854
% Voltage Error	-14.65	-11.80	-15.6	*(0/0) $\sim$ 100
Abs error $\Delta SOC : SOC^* - SOC_{limit}$	-	-	-	0.0453
% SOC Error	-	-	-	*(0/0) $\sim$ 100

conditions to the SOP algorithm resulting in overall poor performance of the algorithm.
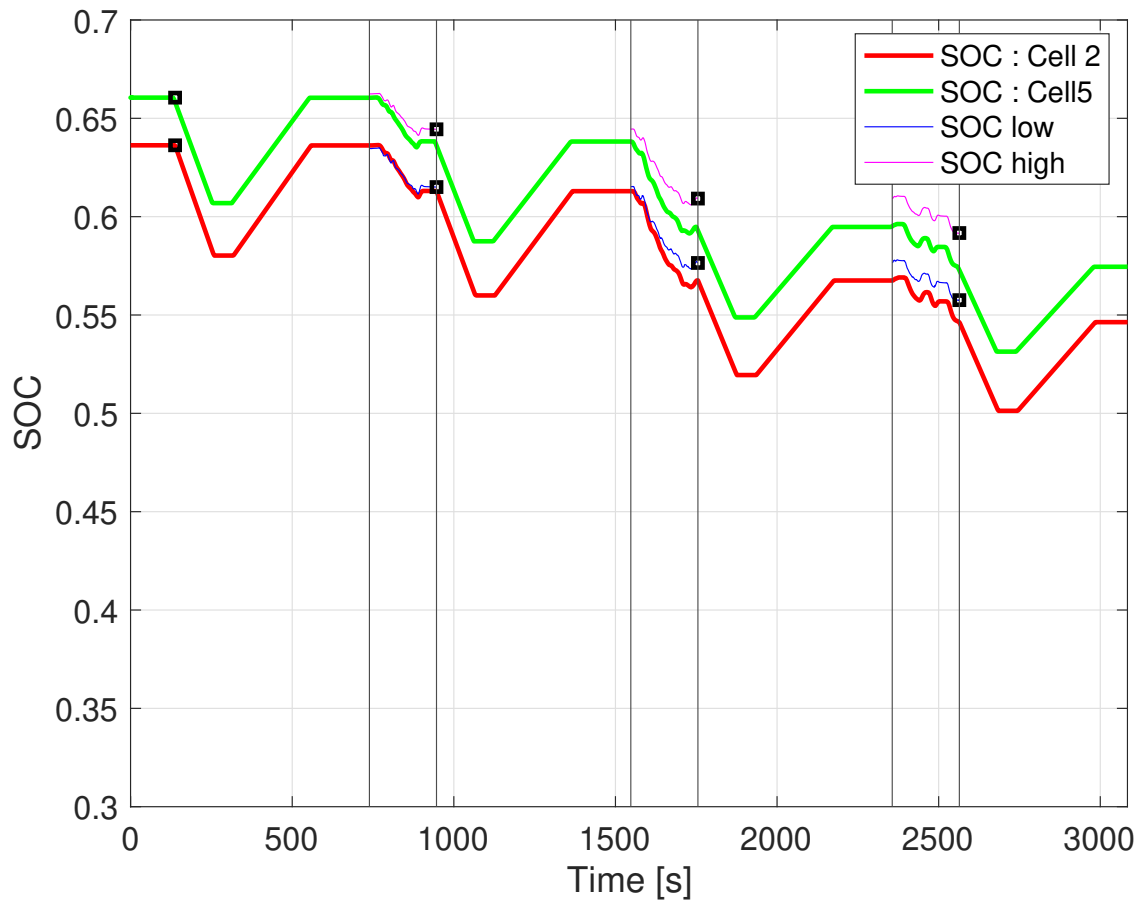
Figure 3.24: Luenberger observer performance to capture initial state uncertainty for SOP

Conclusion

This experimental validation highlights the various challenges associated with accurate SOP prediction. The performance of the SOP algorithm presented in [30] heavily relies on the
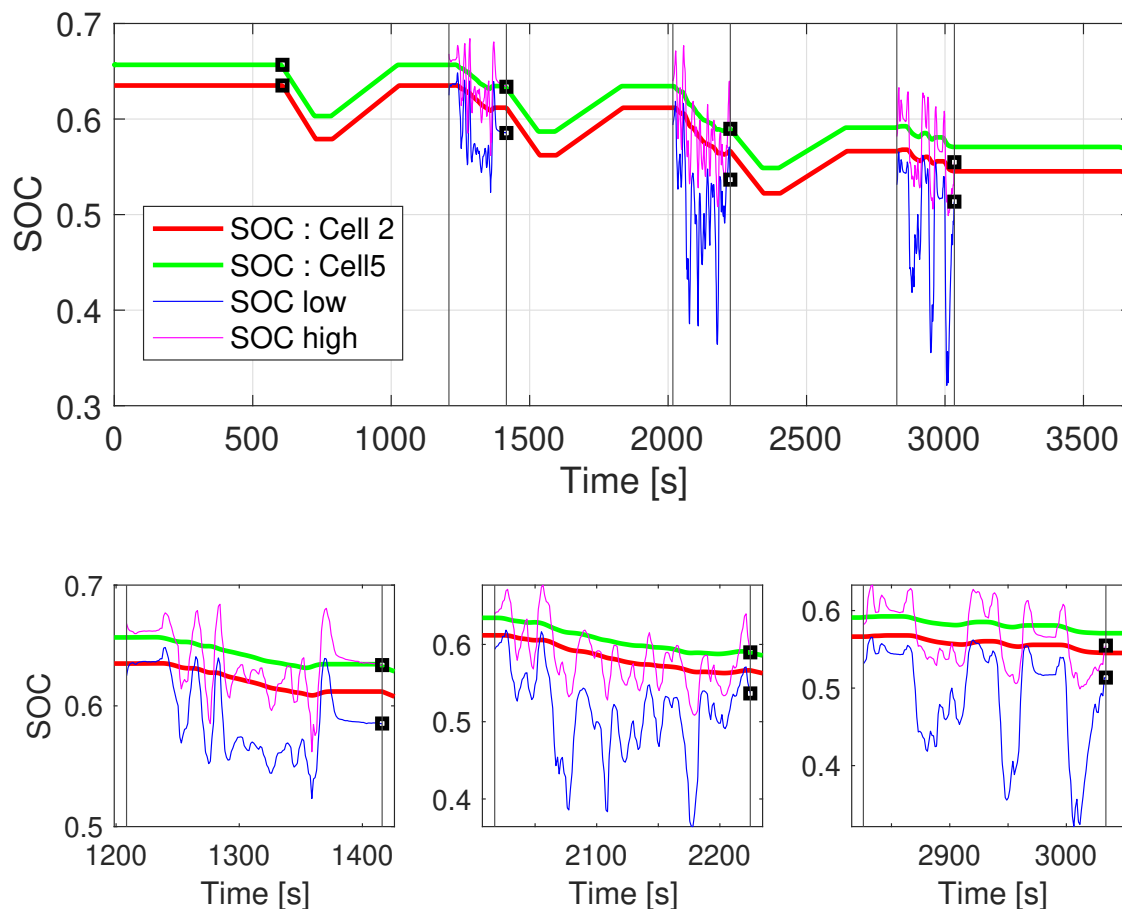
Figure 3.25: Interval observer performance to capture initial state uncertainty for SOP

accurate estimation of initial state and parameter uncertainty. In [30] interval observer algorithm is used for estimating the initial condition for state uncertainty. While performing experimental validation of the interval observer it was observed that the observer did not perform well on experimental data. Hence in this study, the algorithm was also tested by replacing the interval observer with 2 different observers (feedforward and Luenberger observe on each cell). It was observed that approach 2 (observer on each cell) performed better overall.

The validation performed here highlights the complexity involved in formulating an accurate SOP algorithm. Apart from increasing the accuracy of interval observer as proposed in section 3.2, another potential improvement is incorporating an accurate thermal model.

Chapter 4

State-of-Power for battery pack: Reachability Analysis Approach

This chapter focuses on the problem of power prediction for a battery pack with cell-to-cell heterogeneity. In Chapter 2, we delved into the initial groundwork for power prediction, focusing on the estimation of State of Power (SOP) for ECM battery models characterized by uncertain electrical parameters. In this chapter, the emphasis shifts to incorporating the impact of heterogeneity in thermal parameters into SOP estimation. The incorporation of thermal parameter heterogeneity revealed constraints in the effectiveness of the interval predictor introduced in Chapter 2. Consequently, this chapter explores accurate and robust interval prediction algorithms. Through reachability analysis for mixed monotonic systems, we attain comprehensive and narrow bounds for interval prediction of the battery thermal model.

4.1 INTRODUCTION

The paradigm shift from fossil fuels to renewable energies has placed massive gravity on the proper usage of energy storage. Research on energy storage solutions is being pushed to reach the energy and power density limits of conventional energy sources. The last few decades have seen tremendous progress in the research, development, and implementation of batteries in various applications, with a special focus on Li-ion batteries. With real-time application, accurate estimation techniques to monitor the battery is crucial. Hence, mathematical tools for battery modeling and state estimation are essential in the appropriate design of battery cells/packs.

Battery performance is typically quantified by a certain defined set of states, i.e., SO'X', where X is the performance parameter. State of charge (SOC) is the estimation of the cell's available capacity, and state of health (SOH) is the estimation of battery health. SOP is an estimation of the battery's power. The power capacity of a battery pack is a critical factor in deciding its suitability for an application, be it for Electric vehicles (EVs) or grid storage.

For an EV, the battery power governs the vehicle's performance in terms of its acceleration, braking, moving up a gradient, etc. Similarly, for grid storage applications, it determines the peak power demand that a battery storage application can provide/sustain.

For an ordinary cell, (eg. 18650) its capacity and energy are in the order of 3Ah and 10Wh [31]. A battery pack achieves the energy and power demand for an application, say an EV, by connecting a large number of these unit cells in a series-parallel fashion. The scaling of battery packs by increasing the number of cells, comes with the problem of cell heterogeneity.

Cell heterogeneity in a battery pack is always present at some level after manufacturing. The cell-to-cell heterogeneity keeps increasing as the battery ages. This could be due to several reasons, eg. non-uniform temperature distribution across the battery pack, uneven current distribution, increase in cell resistances, etc. This makes the heterogeneous battery pack estimation a crucial problem. The work done in this paper deals with the power estimation of a battery pack considering the cell heterogeneity.

SOP estimation in most literature focuses on cell-level power prediction. Both model-based estimation and characteristic map-based methods are used for SOP prediction. The latter method, although straightforward and easy to implement, lacks the accuracy of model-based methods [10]. For achieving a good balance between desired accuracy and computational efficiency, equivalent circuit models (ECMs) are predominately used [10]. SOP estimation is closely related to the defined safety constraints of the system. The most common safety limits seen in the literature for estimating SOP are based on voltage, current, and SOC. References [10], [12], [11, 14–20] uses Taylor's approximation in OCV equation to simplify the SOP evaluation, which although is simple to implement suffers two main inaccuracies. One arises from Taylor's approximation and the other from the lack of inclusion state dependency of ECM parameters. Reference [10] uses genetic algorithm approach to compute SOP and highlights the inaccuracies of Taylor's method especially over longer time horizons. Reference [21] uses an MPC-based algorithm for SOP computation and accounts for the state-dependent ECM parameters in computation by considering the ECM as a linear parameter-varying (LPV) system. Only a few literature include temperature as the safety constraint for SOP estimation [13], [17], [21]. In addition, most of these cell-level power predictions is scaled for a battery pack assuming uniformity across all the cells in the pack. The battery pack then, as a whole is characterized by a series/parallel combination of identical cells with identical operating conditions. This assumption restricts the application of SOP algorithms to packs with known negligible parameter heterogeneity and operating with uniform temperature distribution.

Addressing cell heterogeneity for SOP in the existing literature is either based on a 'straight-forward method' or 'identification of the weakest set of cells. In the 1st method, all the cells in a pack are considered for power prediction [16]. The maximum allowable charge and minimum allowable discharge current for each cell are calculated in the process, thereby requiring substantial computation power and memory, which increases as the number of cells is increased [16]. The 2nd method is based on the identification of the 'weakest cell' or 'weakest set of cells' which limits the power of the overall battery pack [18], [20].

These 'weakest set of cells' are the ones that first reach the predefined voltage, current, or temperature limits during charging or discharging the battery. This way not all the cells are considered for power computation, thereby reducing the computation demand compared to the straightforward method. However, the 'weakest cell' is a misnomer, as the limiting cell in the pack can change during operation and importantly, isn't necessarily the cell with the most extreme parameter values. Therefore, even if one identifies some cell and labels it as 'weakest', that cell may not dictate the state-of-power.

In this work, the heterogeneity of the cells in the pack is tackled using the concept of interval prediction. The battery pack is considered an uncertain parametric system, and the bounds of the cell's states are estimated using interval prediction. Reachability analysis approach [22], [24] is used here for state interval prediction. Reachability deals with computing the set of states that a system can reach from a given initial condition in finite time. Generally, for most systems, (with the exception of extremely specific and simplistic systems), the exact computation of the reachable set is unfeasible [22], [24]. Hence, several techniques for over-approximating the reachable set are used. Various techniques ranging from mathematical approximations like level sets [32], interval analysis [33], Taylor's approximations [34], to the use of different geometrical over approximations like zonotopes [24],[35], hyper-rectangles [36], ellipsoids [37], polytopes [38] are proposed in literature. Some of the techniques are specific to the type of systems, i.e., linear, non-linear, parameter varying, continuous time, discrete, hybrid etc. Although these techniques are dependent on the system under study, the major factor considered in deciding the over-approximation technique is the compromise between the required accuracy of over-approximation and the involved computation complexity. Considering all these factors into account, for the battery pack model analysis under study, the reachability problem is addressed by using the property of mixed monotonicity [22]. Reachable set can be used to predict the span of model state/output under parameter uncertainty. This makes reachability analysis critical for the SOP analysis with heterogeneous cells.

In our preliminary work in chapter 2 [30], we investigated SOP estimation for ECM battery models with uncertain electrical parameters. In this work, heterogeneity in the cells is further explored, where uncertainty in thermal parameters is also addressed. The novel contributions of this work are as follows:

- The first adoption of reachability analysis to equivalent circuit battery models for SOP prediction.

- An extended definition for state-of-power (SOP) for multi-cell heterogeneous battery packs that considers limits due to voltage, SOC, temperature, and current. The heterogeneity is considered in both the electrical and thermal parameters of the cells for more practical application.

The outline of the paper is as follows. Section 4.2 goes over the details of the battery model considered in the study. Section 4.3 describes the challenges associated with SOP
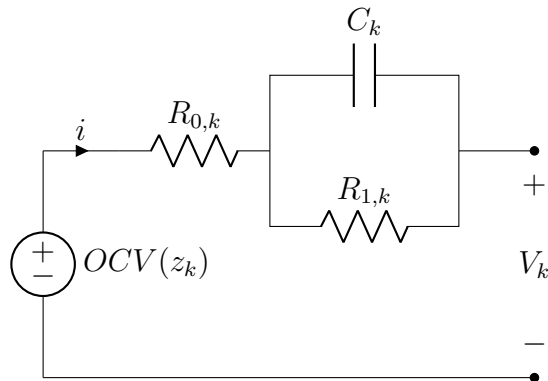
Figure 4.1: ECM with 1-RC pair

estimation and mathematically outlines the problem. Section 4.4 describes the methodology developed for estimating SOP for a battery pack with heterogeneous cells. Section 4.5 presents the results of simulation analysis done for two different applications, i.e. HEV and grid storage. Section 4.6 concludes the overall SOP study.

4.2 Battery Modelling

The cell dynamics of a battery is modeled by an ECM coupled with 2 state thermal dynamics. It should be noted that even though physics-based models have the advantage of accurately representing the system over heuristic-based models, the advantage the data driven heuristic models offers in terms of modeling simplicity, computation effort, make it ideally suited for control-oriented applications [25]. The battery ECM considered in the work is shown in Fig. 4.1, where 'k' represents the cell index. The open circuit potential (OCV) of the cell 'k' is denoted by $V_{OC}(z_k)$, the losses in the cells are modelled by using the 'ohmic resistance' $R_{0,k}$ and the RC pair.

In this study, the configuration of the battery pack considered is a set of heterogeneous cells (or modules) connected in series.

The cell model equations are further detailed in this section.

Electrical Part

The voltage dynamics of a single cell k, using ECM can be represented as follows:

$$\dot{z}_k(t) = \frac{1}{Q_k} I_k(t), \tag{4.1}$$

$$\dot{V}_{c,k} = -\frac{1}{R_{1,k}(z_k, T_k) C_k(z_k, T_k)} V_{c,k} + \frac{1}{C_k(z_k, T_k)} I_k(t), \tag{4.2}$$

$$V_k(t) = OCV(z_k(t)) - V_{c,k}(t) - R_{0,k}(z_k, T_k) I_k(t), \tag{4.3}$$

Where state of charge (z_k) and capacitance-voltage V_c represent the state of the system, and the overall cell voltage V_k is the output of the system. The parameters of the electrical part of the model are Q_k, $R_{0,k}$, $R_{1,k}$ and C_k. It should be noted that the while the cell capacity Q_k is heterogeneous in the pack, the parameters $R_{0,k}$, $R_{1,k}$ and C_k are heterogeneous as well as state dependent.

Thermal Part

The temperature dynamics is modelled by considering two thermal states for each cell, i.e., core temperature $T_{c,k}$ and surface temperature $T_{s,k}$. Thermally the cell is modelled as two point masses representing the core and surface of the cell of capacitance $C_{c,k}$ and $C_{s,k}$ respectively. The overpotentials in the cell that causes deviation of cell output voltage from its OCV, results in heat dissipation $\dot{q}_k$, which results in rise of cell temperature (4.4). The cell is being cooled by a coolant at temperature T_f. The heat exchange between core and surface and then surface and coolant is modeled using thermal resistances $R_{c,k}$ and $R_{u,k}$ respectively. The resistance R_{cc} accounts for heat exchange between neighboring cells as seen in (4.5).

The thermal dynamics of the cell is given by the following equations:

$$C_c \dot{T}_{c,k}(t) = \dot{q}_k(t) + \frac{T_{s,k}(t) - T_{c,k}(t)}{R_c} \tag{4.4}$$

$$C_s \dot{T}_{s,k}(t) = \frac{T_{f,k}(t) - T_{s,k}(t)}{R_u} - \frac{T_{s,k}(t) - T_{c,k}(t)}{R_c}$$
$$+ \frac{T_{s,k-1}(t) + T_{s,k+1}(t) - 2T_{s,k}(t)}{R_{cc}} \tag{4.5}$$

$$\dot{q}_k(t) = I_k(t)(V_k(t) - OCV(z_k(t))) \tag{4.6}$$

$$T_k(t) = \frac{1}{2}(T_{s,k}(t) + T_{c,k}(t)) \tag{4.7}$$

The coolant temperature across all the cells in assumed constant in this study. It should be noted that compared to the earlier study [30] the thermal parameters of the cells ($C_{c,k}$, $C_{s,k}$, $R_{c,k}$, $R_{s,k}$, $R_{c,k}$) are also considered heterogeneous in this study and the heat exchange between the cells is also accounted for by using contact resistance R_{cc}.

The combined ECM and thermal model is referred as ECMT in this study.

4.3 SOP definition and Challenges

In the existing literature, SOP is used as a measure to predict peak power that a battery can constantly sustain for a given time horizon without subjecting the battery/cell to any unsafe operating conditions. The most important factors in defining SOP are the 'time horizon of prediction' and the 'safe regime of operation'. The smaller the time horizon of prediction, the higher the magnitude of constant peak power the battery can withstand. The safe operating regime of the cell is guided by the safety limit of the cell defined by variables like voltage, temperature, etc. These safety limits ensure that the cells are not subjected to conditions that are detrimental to the health of the battery (e.g., overcharge, over-discharge, extreme temperatures etc.) and avoid any instantaneous battery failures like thermal runaway.

In this study, we also define SOP as peak power prediction. The power capacity of the battery is difficult to predict without any prior information about the load/cycle that the battery will undergo. In most literature for SOP, the constant peak power prediction is further simplified to constant peak current prediction as voltage remains almost constant during the majority of a constant current cycle[10–20]. Even from a practical application standpoint controlling constant current input for the battery is much more feasible.

The safety limits considered for the SOP analysis in the study are voltage, SOC, temperature and maximum current. These limits can be listed by the cell manufacturer or can be determined based on the battery application. SOP hence in this study is defined as maximum current (charge/discharge) that the battery can sustain for a given time horizon without violating any of the defined safety constraints:

1. Voltage : $V_{min} \leq V \leq V_{max}$

2. SOC : $SOC_{min} \leq SOC \leq SOC_{max}$

3. Current : $I_{min} \leq I \leq I_{max}$

4. Temperature : $T_{min} \leq T \leq T_{max}$

The two main challenges of SOP prediction when considering the battery pack are parametric heterogeneity and state dependence. As defined in section 4.2, we are dealing with a system with parametric uncertainty. The parametric uncertainty considered is both in electrical and thermal parameters. The electrical parameters (R_1, R_2, C) are not only uncertain but are also state-dependent (i.e., functions of SOC and temperature). Reference [30] shows the ECM parameters of a 2.6Ah NMC cell at different SOC and temperature. The same cells are used for analysis in this study.

In this paper, the objective is to estimate the bounds of the state/output trajectory accurately for a pack of cells. Cells in a battery pack can be placed in various series/parallel configuration. A series arrangement for a cell in a battery pack is considered for analysis in this paper. Owing to series arrangement, the current application across all the cells of the pack is equal, while the voltage response might vary depending on the cell-to-cell

heterogeneity. Each cell's thermal dynamics is also affected by the heat exchange with its
neighboring cells. The overall cell dynamics in the battery pack is given by equations (4.1)-
(4.7). The SOP estimation in this study can be stated as determining maximum constant
current magnitudes $I_{max}^{dis}, I_{max}^{ch}$ for discharge and charge respectively, over a chosen prediction
time horizon T_p. For the safety constraints considered, I_{max}^{dis}, I_{max}^{ch} can be written as:

$$\begin{cases} I_{max,t}^{dis} = \min\left\{ i_{t,T_p}^{dis,SOC}, i_{t,T_p}^{dis,V}, i_{t,T_p}^{dis,T}, i_{t,T_p}^{dis,I} \right\} \\ I_{max,t}^{ch} = \min\left\{ i_{t,T_p}^{ch,SOC}, i_{t,T_p}^{ch,V}, i_{t,T_p}^{ch,T}, i_{t,T_p}^{ch,I} \right\} \end{cases} \tag{4.8}$$

where i_{t,T_p}^{SOC}, $i_{t,T_p}^{dis,V}$, $i_{t,T_p}^{dis,T}$, $i_{max}^{dis,I}$ are the magnitude of maximum constant current that can
be applied for T_p duration, from time t, without violating the SOC, voltage, temperature
and current constrains for a given cell. For the battery pack with 'm' cells in series, these
constraints have to hold for all the cells as shown in (4.9)-(4.10).

For discharge limits $(i^{dis} \leq 0)\forall k = \{1, ..., m\}, \tau \in [t, t + T_p]$:

$$\begin{cases} i_{t,T_p}^{dis,SOC} = \max_{k,\tau}\{|i^{dis}| \mid SOC_k(\tau) \geq SOC_{min}\} \\ i_{t,T_p}^{dis,V} = \max_{k,\tau}\{|i^{dis}| \mid V_k(\tau) \geq V_{min}\} \\ i_{t,T_p}^{dis,T} = \max_{k,\tau}\{|i^{dis}| \mid T_k(\tau) \leq T_{max}\} \\ i_{t,T_p}^{dis,I} = |i_{max}^{dis}| \end{cases} \tag{4.9}$$

Similarly for charge limits $(i^{ch} \geq 0)$:

$$\begin{cases} i_{t,T_p}^{ch,SOC} = \max_{k,\tau}\{|i^{ch}| \mid SOC_k(\tau) \leq SOC_{max}\} \\ i_{t,T_p}^{ch,V} = \max_{k,\tau}\{|i^{ch}| \mid V_k(\tau) \leq V_{max}\} \\ i_{t,T_p}^{ch,T} = \max_{k,\tau}\{|i^{ch}| \mid T_k(\tau) \leq T_{max}\} \\ i_{t,T_p}^{ch,I} = |i_{max}^{ch}| \end{cases} \tag{4.10}$$

It can be noted that discharge current is constrained by minimum limits on SOC and
voltage while charging current is constrained by maximum limits on SOC and voltage. High-
magnitude charging and discharging are both exothermic processes and, hence are limited
by maximum limits on temperature.

SOP can hence be estimated for the battery pack with m cells in series:

$$SOP : \begin{cases} P^{dis} = m \cdot I_{max,t}^{dis} \cdot \underline{V}(I_{max,t}^{dis}) \\ P^{ch} = m \cdot I_{max,t}^{ch} \cdot \underline{V}(I_{max,t}^{ch}) \end{cases} \tag{4.11}$$

where $I_{max,t}^{dis}$, $I_{max,t}^{ch}$ are defined in (2.9) and $\underline{V}(\cdot)$ is calculated from bounds on the state
trajectories, defined later in (2.16).

4.4 SOP PREDICTION ALGORITHM

Owing to uncertain parameters and the initial condition of the cells, the state of all the cells in a pack can be different, which implies that the operating voltage and temperature of the cells are not uniform. Hence for battery SOP prediction, we want to predict the minimum constant current that can take any cell/module in the battery pack to unsafe condition (SOC, Voltage, or temperature). The method presented in this study circumvents the problems related to heterogeneity in the approaches mentioned in section 4.3 by focusing on the evaluation of bounds of state trajectories associated with the cells of the pack, rather than the evaluation of states of all/any of the cells. The system is defined by the ODE:

$$\dot{x} = f(t, x, p), \tag{4.12}$$

where $x \in \mathbb{R}^n$ represents the states and $p \in \mathbb{R}^{n_p}$ represents the parameter. Let the trajectory of the system be denoted by Φ. $\Phi(t; t_0, x_0, p)$ will indicate the state of the system at time $t \geq t_0$, given the initial condition x_0.

For the ECMT system defined similarly to (4.12), we have uncertainty in the initial condition of state and parameters. The initial condition uncertainty and parameter uncertainty are defined using the interval of initial states $[\underline{x_0}, \overline{x_0}]$ and interval of parameters $[\underline{p}, \overline{p}]$. The intervals of vector for $x_0 \in \mathbb{R}^x$ and $p \in \mathbb{R}^n_p$ are defined using componentwise inequality in a n-dimensional and n_p-dimensional Euclidean space such that:

$$[\underline{x_0}, \overline{x_0}] = \{x_0 \in \mathbb{R}^n \mid \underline{x_0} \leq x_0 \leq \overline{x_0}\} \tag{4.13}$$

$$[\underline{p}, \overline{p}] = \{p \in \mathbb{R}^{n_p} \mid \underline{p} \leq p \leq \overline{p}\} \tag{4.14}$$

For a system defined by (4.12), starting from t_0, with initial state interval $[\underline{x_0}, \overline{x_0}]$, parameter bound $[\underline{p}, \overline{p}]$, reachable set R, at time t_f is given by set of all states the system can take:

$$R = \{\Phi(t_f; t_0, x_0, p) \mid x_0 \in [\underline{x_0}, \overline{x_0}], \ p \in [\underline{p}, \overline{p}]\} \tag{4.15}$$

The reachable set prediction is done by predicting the bound of trajectories of the states $[\underline{\Phi}(t), \overline{\Phi}(t)]$:

$$\Phi(t; t_0, x_0, p) \subseteq [\underline{\Phi}(t), \overline{\Phi}(t)] \tag{4.16}$$

We have the following states bounds for ECMT:

$$\begin{cases} \underline{SOC}(t) \leq SOC_k \leq \overline{SOC}(t); & \underline{V_c}(t) \leq V_{c,k} \leq \overline{V_c}(t) \\ \underline{T_c}(t) \leq T_{c,k} \leq \overline{T_c}(t); & \underline{T_s}(t) \leq T_{s,k} \leq \overline{T_s}(t) \end{cases} \tag{4.17}$$

As the OCV is a monotonic function of SOC, the following can also be implied for voltage:

$$\overline{V}(t) = OCV(\overline{SOC}(t)) + \overline{V_c}(t) + I(t)R_{0,max}, \tag{4.18}$$

$$\underline{V}(t) = OCV(\underline{SOC}(t)) + \underline{V_c}(t) + I(t)R_{0,min}, \tag{4.19}$$

$$\overline{T}(t) = \frac{1}{2}(\overline{T_c}(t) + \overline{T_s}(t)), \quad \underline{T}(t) = \frac{1}{2}(\underline{T_c}(t) + \underline{T_s}(t)). \tag{4.20}$$

For SOP evaluation during charging, the following constraints will be enforced:

$$I_{max} \colon \overline{V}(t) \leq V_{max}; \quad \overline{SOC}(t) \leq SOC_{max}; \quad \overline{T}(t) \leq T_{max}. \tag{4.21}$$

Similarly for discharging:

$$I_{max} \colon V_{min} \leq \underline{V}(t); \quad SOC_{min} \leq \underline{SOC}(t); \quad \overline{T}(t) \leq T_{max}. \tag{4.22}$$

Both high current charging and discharging processes are generally exothermic processes, hence thermal constraint is focused on $\overline{T}(t)$. It is assumed that coolant temperature T_f is higher than T_{min}, thereby implying that $T_{min} \leq \underline{T}(t)$ is satisfied at all times.

Evaluation of these bounding system trajectories simplifies the SOP prediction with heterogeneity substantially, as the focus is only on the evaluation of bounding state trajectories that encompass all the cells rather than the state determination of any individual cell. This is a huge advantage in terms of the number of cell scaling, as increasing the no of heterogeneous cells has no impact on the computation effort or memory required for SOP evaluation.

The SOP algorithm developed consists this study consists of four different components described further in this section. The reachability analysis in combination with the Modified reference governor (MRG) is used to predict the SOP. The reachability algorithm predicts the state bounds for a given input current, while MRG iteratively computes the maximum current that keeps the state/output bounds in the safe operating window. Fig. 4.4 shows the interaction of reachability with MRG. The two other components, i.e. interval observer and adaptive parameter bounding is used to increase the overall accuracy of the algorithm. Fig. 4.5 shows the overall SOP algorithm. The connection with the different sub-components is similar to the earlier work [30]. The main difference between [30] and this work is the state prediction algorithm. The earlier work uses Leurent's method [23] for predicting state bound whereas in this work we use reachability analysis [22].

Reachability Analysis

Reachability deals with the prediction of states that a given system can attain in a finite time horizon from a given initial condition. As stated, the ECMT model in our study is a system with uncertainty in its parameters as well as initial conditions. The prediction of tight estimates state bounds is essential for accuracy. Unlike state observers where control over observer gain gives the flexibility to have a stable as well as robust state estimate, state predictor's stability, robustness and accuracy are immensely algorithm dependent [23][27].

Monotonic and Mixed monotonic system Background Monotonic systems are simplified 'cooperative' systems, whose state trajectories preserve a partial order[22]. A system defined by (4.12) can be considered a monotonic system if the following inequalities hold for any pair of vectors $x_0, \hat{x}_0 \in \mathbb{R}^x$ and $p, \hat{p} \in \mathbb{R}^p$:

$$x_0 \leq \hat{x}_0, \ p \leq \hat{p} \Rightarrow \Phi\left(t_f; t_0, x_0, p\right) \leq \ \Phi\left(t_f; t_0, \hat{x}_0 \, \hat{p}\right) \tag{4.23}$$

The above equation signifies component-wise inequality between the vectors.

For the above condition to hold, there are strict conditions on the sign-stability and structure of the Jacobian of the system [22], which limits the classification of a number of systems into the monotonic category. The ECMT system under study also does not satisfy the conditions of a monotonic system.

A mixed monotone system is a generalized version of a monotonic system, which can be decomposed into a monotonically increasing part and a monotonically decreasing part. A wider class of system, which generally is any continuous-time dynamical system with a Lipschitz continuous vector field, falls under the category of mixed monotonic. This facilitates the application of valuable and robust reachability set theorems of monotonic systems to a broader variety of systems.

Definition 1 [22]: The system defined, is called a mixed monotone, if the mapping $f : \mathbb{R} \times \mathbb{R}^x \times \mathbb{R}^p \to \mathbb{R}^x$ can be decomposed into $g : \mathbb{R} \times \mathbb{R}^x \times \mathbb{R}^p \times \mathbb{R}^x \times \mathbb{R}^p \to \mathbb{R}^x$ such that the following conditions are satisfied[22]:

1. For all $x \in \mathbb{R}^x$ and $p \in \mathbb{R}^p$, f is embedded on the diagonal of g, i.e., $g(t, x, p, x, p) = f(t, x, p)$

2. For all $i, j \in \{1, \ldots., n_x\}, k = \{1, \ldots, n_p\}$ and $i \neq j$, g is monotonic increasing in terms of the first pair of argument, i.e., $x_1 \geq x_2 \Rightarrow g(t, x_1, p, \hat{x}_0 \hat{p}) \geq g(t, x_2, p, \hat{x}_0 \hat{p})$ and $p_1 \geq p_2 \Rightarrow g(t, x, p_1, \hat{x}_0 \hat{p}) \geq g(t, x, p_2, \hat{x}_0 \hat{p})$:

$$\frac{\partial g_i(t, x, p, \hat{x}, \hat{p})}{\partial x_j} \geq 0, \qquad \frac{\partial g_i(t, x, p, \hat{x}, \hat{p})}{\partial p_k} \geq 0, \tag{4.24}$$

3. For all $i, j \in \{1, \ldots., n_x\}$ and $k = \{1, \ldots, n_p\}$ and $i \neq j$, g is monotonic decreasing in terms of the first pair of argument, i.e., $x_1 \geq x_2 \Rightarrow g(t, x_1, p, \hat{x}_0 \hat{p}) \leq g(t, x_2, p, \hat{x}_0 \hat{p})$ and $p_1 \geq p_2 \Rightarrow g(t, x, p_1, \hat{x}_0 \hat{p}) \leq g(t, x, p_2, \hat{x}_0 \hat{p})$:

$$\frac{\partial g_i(t, x, p, \hat{x}, \hat{p})}{\partial \hat{x}_j} \leq 0, \qquad \frac{\partial g_i(t, x, p, \hat{x}, \hat{p})}{\partial \hat{p}_k} \leq 0, \tag{4.25}$$

Mathematically, the applicability of the approach can be examined by checking the boundedness of the Jacobian matrices. If there exists matrix L_x and L_p such that adding them in the Jacobian matrices J_x and J_p respectively results in sign stable matrices over time, in state and parameter range under consideration then the system is a mixed monotone. Sign stability implies that each element of the matrix of $J_x + L_x$ (except the diagonal elements) and $J_p + L_p$, has a constant sign at any time even though its state, parameter, or input might vary. This is stated in Assumption 1.

Assumption 1 [22]: For a given state vector $x \subseteq \mathbb{R}^{n_x}$, and parameter vector $p \subseteq \mathbb{R}^{n_p}$ there exist $L_x \in \mathbb{R}^{n_x \times n_x}$, and $L_p \in \mathbb{R}^{n_x \times n_p}$ such that the following conditions are satisfied.

1. For all $i, j \in \{1, \ldots, n_x\}$ with $j \neq i$, we have either

$J_{xij}(t, x, p) + L_{xij} \geq 0, \quad \forall\, t \in [t_0, t_f], \; x \in X, \; p \in [\underline{p}, \bar{p}]$

Or

$J_{xij}(t, x, p) + L_{xij} \leq 0, \quad \forall\, t \in [t_0, t_f], \; x \in X, \; p \in [\underline{p}, \bar{p}]$

2. For all $i \in \{1, \ldots, n_x\}$ and $k \in \{1, \ldots, n_p\}$ we have either:

$J_{pik}(t, x, p) + L_{pik} \geq 0, \quad \forall\, t \in [t_0, t_f], \; x \in X, \; p \in [\underline{p}, \bar{p}]$

Or

$J_{pik}(t, x, p) + L_{pik} \leq 0, \quad \forall\, t \in [t_0, t_f], \; x \in X, \; p \in [\underline{p}, \bar{p}]$

Given Assumption 1 is satisfied, the decomposition function g is defined as:

$$g_i(t, x, p, \hat{x}, \hat{p}) = f_i\left(t, \; \xi^i, \pi^i\right) + |L_{xi*}|\,(x - \hat{x}) + |L_{pi*}|\,(p - \hat{p}) \tag{4.26}$$

where each component of g_i is defined by a transformed state $\xi^i \in \mathbb{R}^{n_x}$ and parameter $\pi^i \in \mathbb{R}^{n_p}$. The transformed state ξ^i and parameter π^i definition depends upon the sign of components in matrices L_x and L_p respectively (4.27-4.28).

$$\xi^i_j : \begin{cases} x_j & if\ L_{xij} \geq 0, \\ \hat{x}_j & if\ L_{xij} \leq 0 \end{cases} \tag{4.27}$$

Similarly:

$$\pi^i_j : \begin{cases} p_k & if\ L_{pik} \geq 0, \\ \hat{p}_k & if\ L_{pik} \leq 0 \end{cases} \tag{4.28}$$

L_{xij} and L_{pik} are the elements of matrices L_x and L_p defined in Assumption 1. The elements of transformed state $\xi^i = [\,\xi^i_1; ...; \; \xi^i_{n_x}]$ and parameter $\pi^i = [\,\pi^i_1; ...; \; \pi^i_{n_p}]$ are either $[x$ or $\hat{x}]$; $[p$ or $\hat{p}]$ depending on sign of L_{xij} and L_{pik} respectively.

The resulting embedded system becomes a new dynamical system in $\mathbb{R}^{2n_x}$:

$$\begin{pmatrix} \dot{x} \\ \dot{\hat{x}} \end{pmatrix} = h(t, x, p, \hat{x}, \hat{p}) = \begin{pmatrix} g(t, x, p, \hat{x}, \hat{p}) \\ g(t, \hat{x}, \hat{p}, x, p) \end{pmatrix} \tag{4.29}$$

Proposition 1 [22]: Under Assumption 1, and the system definition according to (4.26-4.29), the overapproximation of the reachable set $R(t_f; t_0, [\underline{x_0}, \overline{x}_0], [\underline{p}, \bar{p}])$ in (4.15) can be defined by interval

$[\Phi^h_{1...n_x}(t_f; t_0, x, p, \bar{x}, \bar{p}), \quad \Phi^h_{n_x+1...2n_x}(t_f; t_0, x, p, \bar{x}, \bar{p})]$

where $\Phi^h_{1...n_x}$ and $\Phi^h_{n_x+1...2n_x}$ represent the first and last n_x component of Φ^h respectively.

Reachability analysis for battery power prediction

For the ECMT model described in the section 4.2, power prediction is done utilizing the reachability analysis method described for the mixed monotonic system. From the model equations, it can be observed that there are two states, i.e., $\{SOC,\ V_c\}$ that represent the electric part of the model for each cell. The thermal part on the other hand, though, is also represented by two states T_c, T_s, but the dynamics for each cell $T_{s,k}$ is linked with the dynamics of the neighboring cells in contact $(T_{s,k-1}, T_{s,k+1})$, as seen by (4.5). This complicates the analysis as the objective is to have one single representation of the state of all the cells in the pack and avoid the state prediction for individual cells. To this extent, therefore the following approximation is introduced.

The term $\frac{T_{s,k-1}(t) + T_{s,k+1}(t) - 2T_{s,k}(t)}{R_{cc}}$ represents conductive heat transfer between cells, which can be eliminated considering the following:

1. For the hottest cell in the pack, this term would only provide cooling, thereby lowering its temperature. Assuming the hottest cell, to be surrounded by cells equally hot i.e. $(T_{s,k-1} = T_{s,k+1} = T_{s,k})$, is an over-approximation in the calculation of the upper-temperature limit of the cells.

2. For the coldest cell in the pack, this term would only provide heating, thereby increasing its temperature. Assuming the coldest cell, to be surrounded by cells equally cold i.e. $(T_{s,k-1} = T_{s,k+1} = T_{s,k})$ is an under approximation in the calculation of the lower temperature limit of the cells.

The above approximation $(T_{s,k-1} = T_{s,k+1} = T_{s,k})$ eliminates the cell to cell conductive term. By eliminating the conductive term, which tries to bring all cells to the same temperature, we over-predict and under-predict the highest and lowest temperature of the cells respectively in the battery. Hence considering the above approximations, the ECMT model (4.1-4.6) can be reduced to a simpler form (4.30) which bound the temperature of all the cells.

$$
\begin{bmatrix} \dot{SOC_k} \\ \dot{V_{c,k}} \\ \dot{T_{c,k}} \\ \dot{T_{s,k}} \end{bmatrix} = \begin{bmatrix} \frac{I}{Q_k} \\ -\frac{1}{R_{1,k}C}V_c + \frac{1}{C_k}I \\ \frac{1}{C_{c,k}}\left(I_k * (V_c + I_k R_{0,k})\right) + \frac{1}{R_{c,k}C_{c,k}}(T_{s,k} - T_{c,k}) \\ \frac{1}{R_{u,k}C_{s,k}}(T_f - T_s) - \frac{1}{R_{c,k}C_{s,k}}(T_s - T_c) \end{bmatrix} \tag{4.30}
$$

The states considered in the model for each cell 'k' are, $x = [SOC,\ V_c,\ T_c,\ T_s]$. The cell-to-cell variation is caused by:

1. Parametric uncertainty in electric model i.e. $R_{0,k}$, $R_{1,k}$, C_k, Q_k, leading to cells operating at different states. Further, the parameters R_0, R_1, C are state-dependent which causes additional enhancement in state variations across the cells.

2. The temperature variation in cells is caused by firstly, because of heterogeneity in thermal parameters i.e. $\{R_c, R_u, C_c, C_s\}$. Secondly, variation in electric dynamics

due to ohmic and overpotential losses, produces non-uniform heat generation further
increasing temperature differences.

ECMT has uncertainty in 8 model parameters as stated above, the uncertain parametric
set considered for the reachability analysis is taken as follows:

$$p = [\frac{1}{Q} \quad \frac{1}{RC} \quad \frac{1}{C} \quad R_0 \quad \frac{1}{R_cC_c} \quad \frac{1}{R_uC_s} \quad \frac{1}{R_cC_s} \quad \frac{1}{C_c}] \in \mathbb{R}^8 \tag{4.31}$$

The model parameters are combined and the resulting uncertain set of parameters con-
sidered for the reachability analysis is stated above. The reason behind combining model
parameters into the set of parameters mentioned above is that the resulting system can be
represented as mixed monotonic. The resulting equations can be written as:

$$\begin{bmatrix} \dot{x}_1 \\ \dot{x}_2 \\ \dot{x}_3 \\ \dot{x}_4 \end{bmatrix} = \begin{bmatrix} p_1 \cdot I \\ -p_2 \cdot x_2 + p_3 \cdot I \\ p_8 \left(I \cdot (x_2 + I \cdot p_4) \right) + p_5 \left(x_4 - x_3 \right) \\ p_6 \left(T_f - x_4 \right) - p_7 \left(x_4 - x_3 \right) \end{bmatrix} \tag{4.32}$$

To check the application of the mixed monotonicity reachability method in the ECMT
system, the focus is on finding matrix L_x and L_p such that $J_x + L_x$(apart from diagonal
element) and $J_p + L_p$ are sign stable (constant sign) at all time, in range of states and input
considered. This translates to checking the boundedness of the Jacobian matrixes.

$$J_x = \begin{bmatrix} \frac{\partial f_1}{\partial x_1} & \frac{\partial f_1}{\partial x_2} & \frac{\partial f_1}{\partial x_3} & \frac{\partial f_1}{\partial x_4} \\ \frac{\partial f_2}{\partial x_1} & \frac{\partial f_2}{\partial x_2} & \frac{\partial f_2}{\partial x_3} & \frac{\partial f_2}{\partial x_4} \\ \frac{\partial f_3}{\partial x_1} & \frac{\partial f_3}{\partial x_2} & \frac{\partial f_3}{\partial x_3} & \frac{\partial f_3}{\partial x_4} \\ \frac{\partial f_4}{\partial x_1} & \frac{\partial f_4}{\partial x_2} & \frac{\partial f_4}{\partial x_3} & \frac{\partial f_4}{\partial x_4} \end{bmatrix} = \begin{bmatrix} 0 & 0 & 0 & 0 \\ 0 & -p_2 & 0 & 0 \\ 0 & p_8I & -p_5 & p_5 \\ 0 & 0 & p_7 & -(p_6 + p_7) \end{bmatrix} \tag{4.33}$$

It can be observed that the matrix J_x is always sign stable both for charge and discharge
cases. All parameters are non-negative i.e. $p \geq 0$, hence

$$\text{when } I \geq 0, \quad sign\left(J_x\right) = \begin{bmatrix} 0 & 0 & 0 & 0 \\ 0 & - & 0 & 0 \\ 0 & + & - & + \\ 0 & 0 & - & - \end{bmatrix}$$

$$\text{when } I \leq 0, \quad sign\left(J_x\right) = \begin{bmatrix} 0 & 0 & 0 & 0 \\ 0 & - & 0 & 0 \\ 0 & - & - & + \\ 0 & 0 & - & - \end{bmatrix}$$

Similarly,

$$
J_p = \begin{bmatrix}
\frac{\partial f_1}{\partial p_1} & \frac{\partial f_1}{\partial p_2} & \frac{\partial f_1}{\partial p_3} & \frac{\partial f_1}{\partial p_4} & \frac{\partial f_1}{\partial p_5} & \frac{\partial f_1}{\partial p_6} & \frac{\partial f_1}{\partial p_7} & \frac{\partial f_1}{\partial p_8} \\
\frac{\partial f_2}{\partial p_1} & \frac{\partial f_2}{\partial p_2} & \frac{\partial f_2}{\partial p_3} & \frac{\partial f_2}{\partial p_4} & \frac{\partial f_2}{\partial p_5} & \frac{\partial f_2}{\partial p_6} & \frac{\partial f_2}{\partial p_7} & \frac{\partial f_2}{\partial p_8} \\
\frac{\partial f_3}{\partial p_1} & \frac{\partial f_3}{\partial p_2} & \frac{\partial f_3}{\partial p_3} & \frac{\partial f_3}{\partial p_4} & \frac{\partial f_3}{\partial p_5} & \frac{\partial f_3}{\partial p_6} & \frac{\partial f_3}{\partial p_7} & \frac{\partial f_3}{\partial p_8} \\
\frac{\partial f_4}{\partial p_1} & \frac{\partial f_4}{\partial p_2} & \frac{\partial f_4}{\partial p_3} & \frac{\partial f_4}{\partial p_4} & \frac{\partial f_4}{\partial p_5} & \frac{\partial f_4}{\partial p_6} & \frac{\partial f_4}{\partial p_7} & \frac{\partial f_4}{\partial p_8}
\end{bmatrix}
= \begin{bmatrix}
I & 0 & 0 & 0 & 0 & 0 & 0 & 0 \\
0 & -x_2 I & 0 & 0 & 0 & 0 & 0 & 0 \\
0 & 0 & 0 & p_8 \cdot I^2 & (x_4 - x_3) & 0 & 0 & I(x_2 + I.p_4) \\
0 & 0 & 0 & 0 & 0 & (T_f - x_4) & -(x_4 - x_3) & 0
\end{bmatrix}
$$

$$(4.34)$$

To check the sign of J_p matrix, a closer analysis is required as now state values are involved in sign calculation.

For SOP estimation we are predicting the maximum constant charging or discharging current that a battery can sustain. During high constant current charging, $I \geq 0$, $V_c = x_2 \geq 0$ and $\dot{Q} = I(V_c + IR_0) \geq 0$. Similarly for constant current discharging process, $I \leq 0$, $V_c = x_2 \leq 0$ and $\dot{Q} = I(V_c + IR_0) \geq 0$. As $\dot{Q} \geq 0$ both for high current charging and discharging conditions, the cell is always generating heat, therefore the core temperature of the cell is going to be higher than the surface temperature which in turn is higher than the temperature of the coolant, i.e. $T_c > T_s$ ($x_3 > x_4$) and $T_s \geq T_f$ ($x_4 > T_f$).

When:

$$
I \geq 0 \quad sign(J_p) = \begin{bmatrix}
+ & 0 & 0 & 0 & 0 & 0 & 0 & 0 \\
0 & - & + & 0 & 0 & 0 & 0 & 0 \\
0 & 0 & 0 & + & - & 0 & 0 & + \\
0 & 0 & 0 & 0 & 0 & - & + & 0
\end{bmatrix}
$$

$$
I \leq 0 \quad sign(J_p) = \begin{bmatrix}
- & 0 & 0 & 0 & 0 & 0 & 0 & 0 \\
0 & + & - & 0 & 0 & 0 & 0 & 0 \\
0 & 0 & 0 & + & - & 0 & 0 & + \\
0 & 0 & 0 & 0 & 0 & - & + & 0
\end{bmatrix}
$$

As the Jacobians J_x and J_p itself are sign stable, in both charging and discharging conditions respectively, the reachability method for the mixed monotone system can be applied here. Following the interval prediction algorithm mentioned above, proposition 1 is used for reachability set evaluation. This is done utilizing the Matlab toolbox, TIRA [39]. The TIRA toolbox developed by Meyer [22],[39] contains different reachability algorithms, for the purpose of this study we used the mixed monotonicity method.

Figure 4.2 and 4.3 shows the results of interval prediction for the ECMT states, starting from the given initial condition for a constant current magnitude of +/-10A (3.8C), with the following:

1. $\pm 10\%$ heterogeneity in capacity

2. $\pm 20\%$ heterogeneity in electrical parameters

3. $\pm 5\%$ heterogeneity within thermal parameters

The results show the state evolution over 200 sec. The solid blue lines in Fig. 4.2, Fig. 4.3 represent the state's upper and lower bounds predicted over the time horizon. To verify the accuracy and tightness of the predicted bounds, simulations are also performed with a random set of parameters chosen within the defined uncertainty window. The solid black lines in Fig. 4.2, Fig. 4.3 are the resulting state evolution when a random set of parameters is chosen for simulation. Fig. 4.2, Fig. 4.3 thus verifies the tightness and accuracy of state bounds, against state evolution observed for 1000 random parameter simulations.
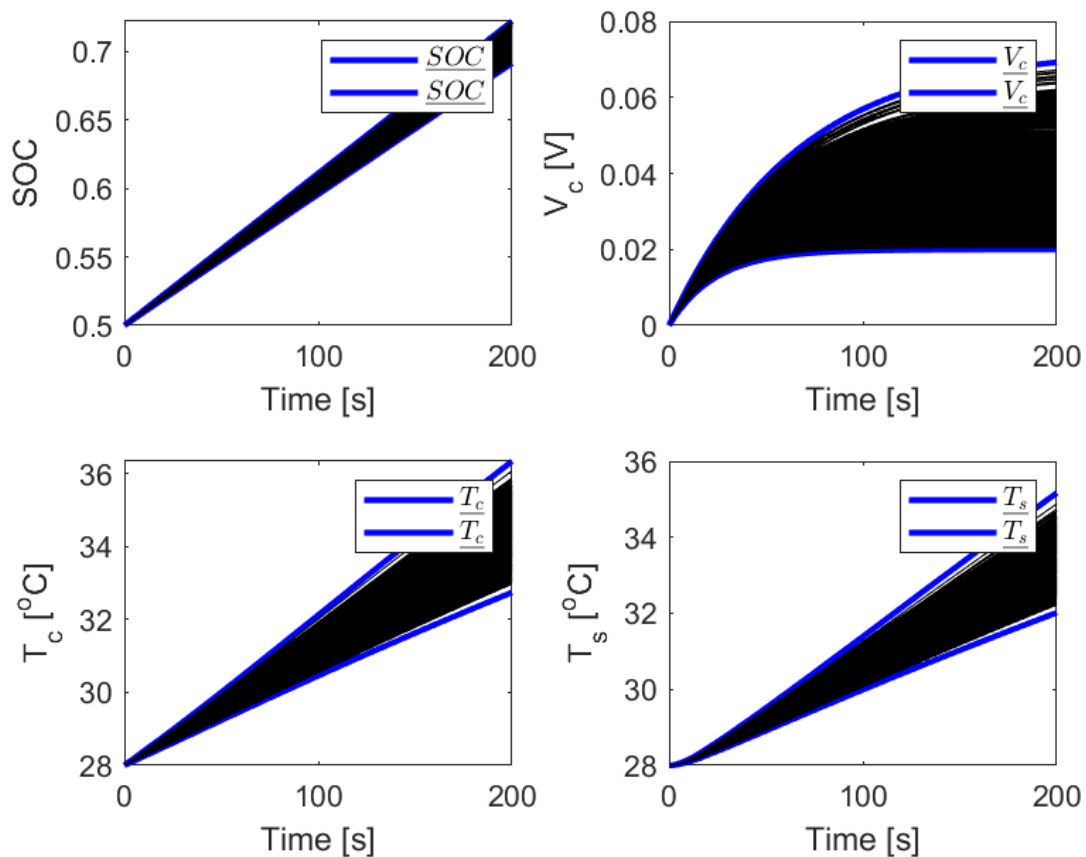
Figure 4.2: State interval prediction for constant charge current

Now that we can fairly accurately predict the state bound for the uncertain LPV (ECMT) system, for a given current magnitude, with tight over approximations, the remaining link for SOP estimation is maximum safe current prediction. This is accomplished using the MRG, as explained in the section below.
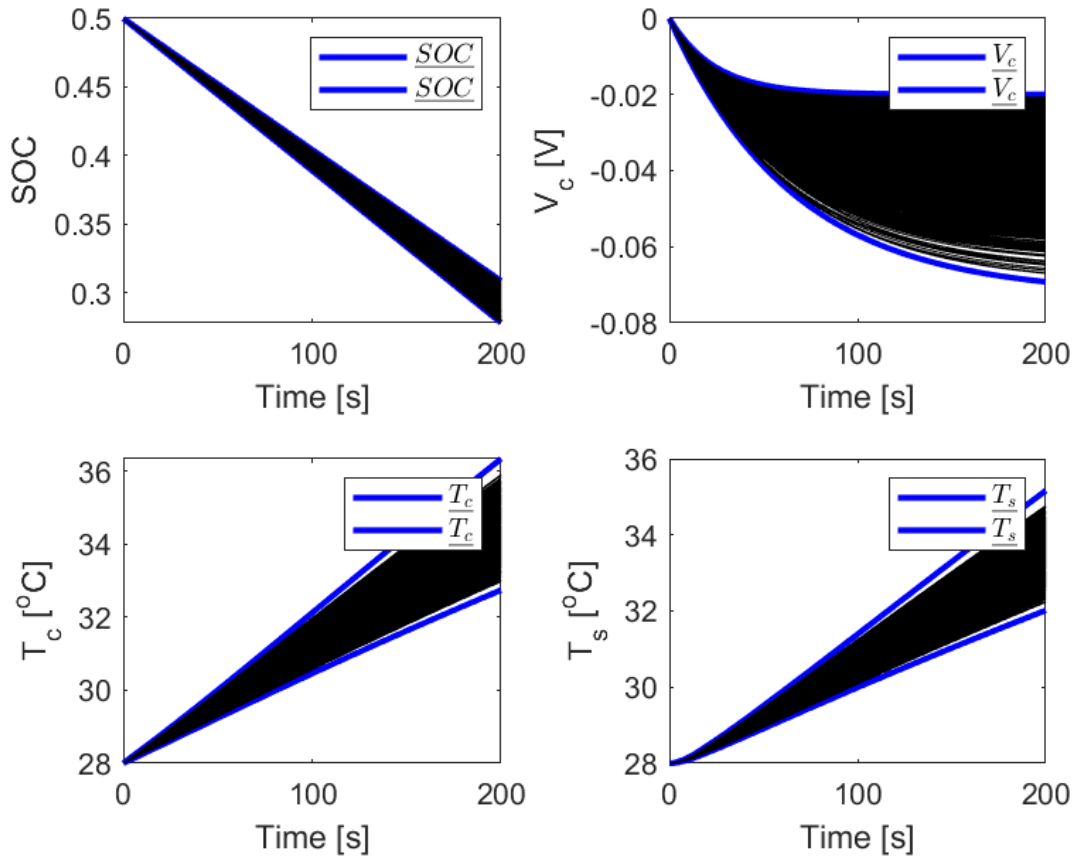
Figure 4.3: State interval prediction for constant discharging current

Modified Reference Governor

The MRG is used in this study to compute the maximum current, that keeps the predicted state bounds in the safe operating region, for the chosen time horizon. Integration of MRG with reachability analysis is shown in Fig. 4.4. The input to MRG is reference current I_r, which is chosen as the maximum current limit of the cell. The output of MRG is an attenuated current signal $I(t)$, which becomes the input of the reachability algorithm. For the given input current $I(t)$, the reachability algorithm predicts the bounds of state and output trajectories. The bounds of state and output trajectories are then checked with the safety constraints of the cell and are fed back to the MRG. The MRG then based on the feedback signal evaluated $I(t)$. The goal of MRG is to evaluate $I(t)$, as close as possible to I_r, such that the safety constraints of the system are satisfied. The way MRG computes $I(t)$ is similar to the bisection algorithm implemented in [12]. Equation (4.35) shows the evaluation of $I(t)$, where I_r is reference input current as α is the scaling factor that is
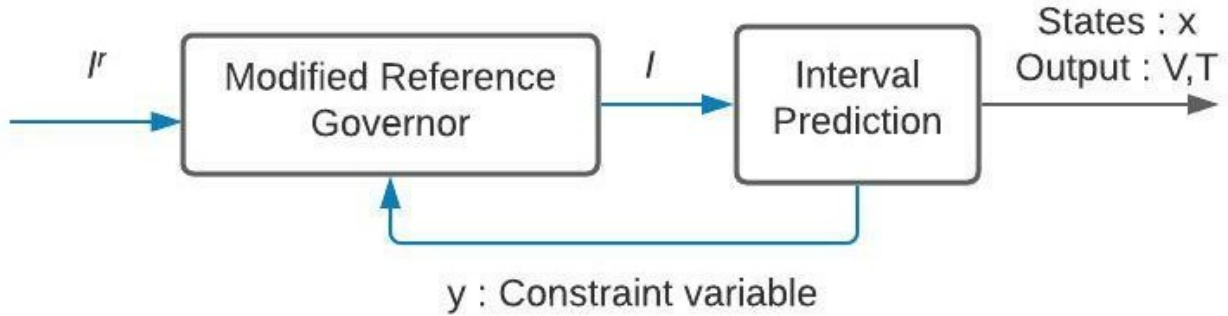
Figure 4.4: MRG and reachability integration

computed iteratively based on the feedback constraint variable y.

$$I(t) = \alpha I^r(t) \quad \forall\ t \in [t,\ t+T_p]. \tag{4.35}$$

The scaling factor α hence can be written as (4.36), where Y is the admissible set of states/output and y is the output of reachable state bounds.

$$y = R(t_f; t_0, [\underline{x}_0, \overline{x}_0], [\underline{p}, \bar{p}]) = [\underline{\Phi}(t),\ \overline{\Phi}(t)]$$

$$\alpha = \max\left\{\alpha \in [0,1]\ :\ y \in Y, \quad t \in [t, t+T_p]\right\}. \tag{4.36}$$

Interval Observer

The accuracy of SOP prediction is measured by the tightness of the predicted state bounds. Two important factors affecting the tightness of predicted state bounds are over-approximations in the interval prediction method and over-approximations in the initial conditions. As can be observed in (4.15), the reachable set is defined by an interval on the initial conditions for the state. Any slack in the initialization of state interval bounds at the moment of SOP prediction will be translated into overapproximations in the entire state trajectories. However, we don't have any measurement of the initial set of states of the battery pack, hence the bounds on initial states need to be estimated precisely. To this end, we use the concept of interval state observer from previous work [6], [30].

Adaptive Parameter bounding

Adaptive parameter bounding is a feature added to the SOP algorithm to increase the accuracy of the algorithm. One of the inputs of the reachability algorithm is parameter bounds. As mentioned before the ECM parameters are uncertain as well as state-dependent. Hence setting proper parameter bounds is convoluted. Taking the extreme values of parameters from the entire ECM parameter map would result in conservative state bounds. Adaptive
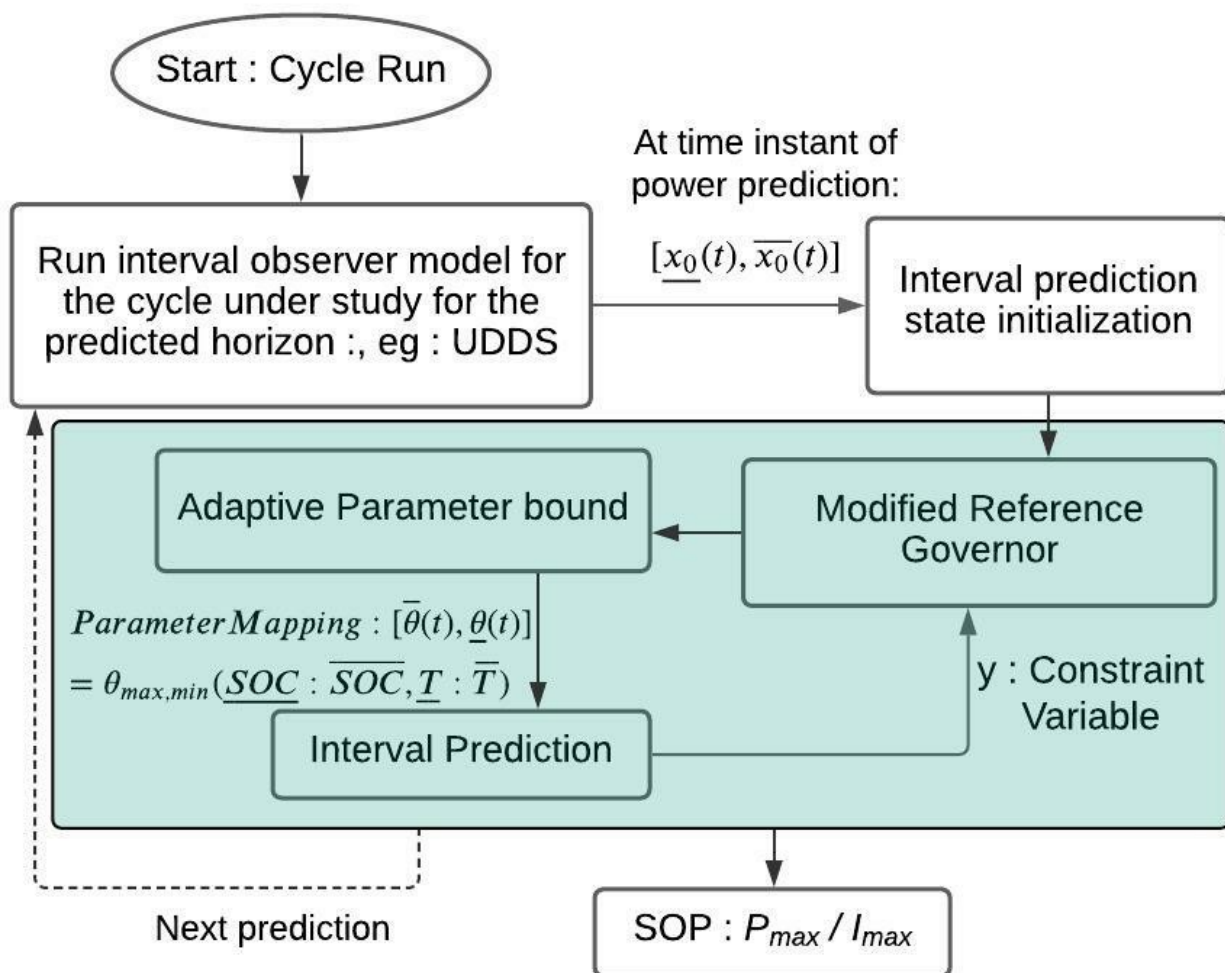
Figure 4.5: SOP prediction using MRG and interval prediction

parameter bounding is a way of choosing the appropriate tighter parameter bound that
would be the input to state bound prediction model i.e. reachability. Further details about
the adaptive parameter bounding can be found in [30].

4.5   Results

The power prediction accuracy of the SOP algorithm presented is validated for different
profiles and applications. The application can range from small HEV battery packs to large
stationary grid storage. In both cases, accurate power prediction is critical. For HEV,

getting instantaneous power estimates determines the accelerating capability of the vehicle, while for grid energy storage it determines the capacity of the energy storage system to keep up with energy demand. Even though the definition of SOP remains the same in both these applications, the way SOP determination would be done varies immensely. In HEV application, the number of cells in a series is far less than the no of cells that make up the grid storage. HEVs are built to be power intensive, hence the cycle that an HEV battery goes through is high C-rate, high-frequency currents [40]. Grid energy storage on the other hand deals with low to moderate C-rate, with low current fluctuations. The power prediction of HEV is done for the prediction horizon of 10 sec- 120 sec (instant vehicle acceleration), while for grid application the prediction horizon would be in the range of 0.5 hr – 1hr (hourly power demand). The SOP algorithm developed for the heterogeneous series cell system is tested for both the applications (HEV and grid) to confirm its robustness and versatility across wide-ranging applications. In this section, we go through both cases. For both applications we assume the battery pack to be made up of the same type of cells, i.e. an NMC cell with 2.6Ah nominal capacity.

Case 1: Small HEV pack
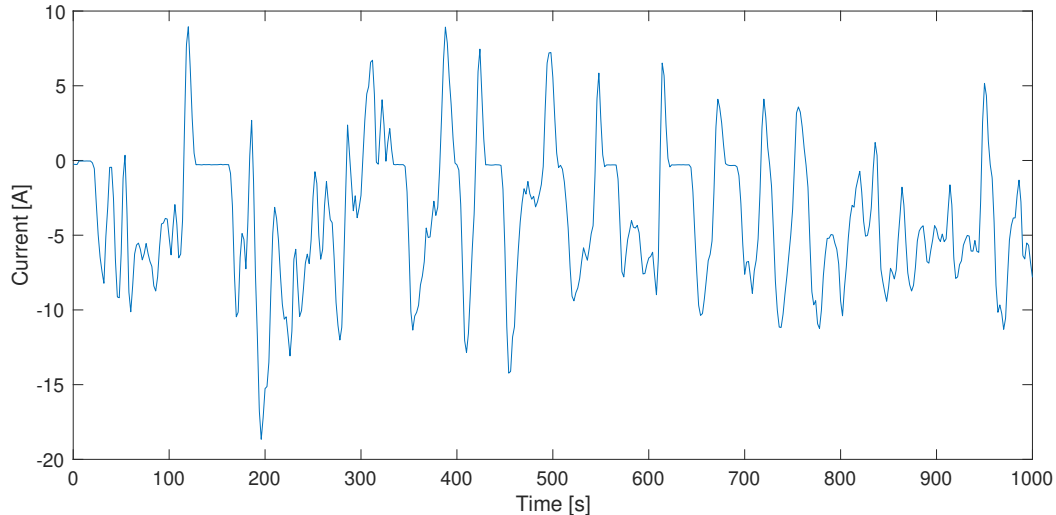
Figure 4.6: Current profile for analysis in Case 1

In the 1st case study, a battery pack that consists of 5 cells in series is chosen to replicate a small HEV battery pack. A real-world HEV battery pack is composed of many more cells. However, we limit our case study to five cells to avoid confusion and clutter when attempting to interpret the results. We use nominal data of the NMC cell [30] to construct the pack. The parametric heterogeneity is considered uniformly distributed around its nominal values.
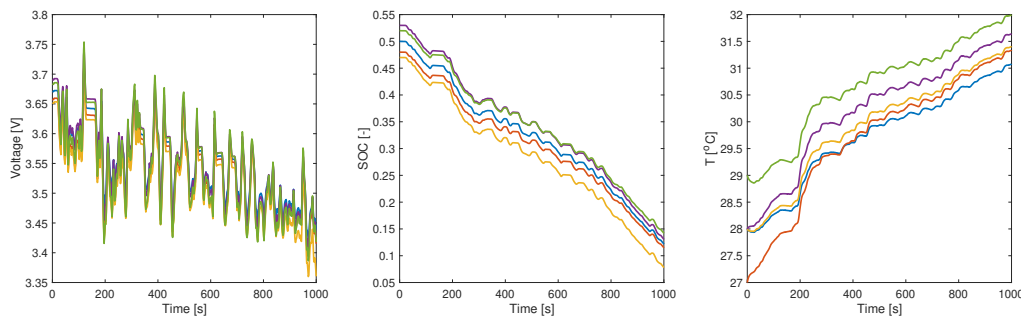
Figure 4.7: State and output profile for individual cells

20% variation is considered in the ECM parameters R_0,R_1 and C, while 10% variation is considered cell capacity (Q) and 5% variation is considered in thermal parameters R_u, R_c, C_c and C_s.

For automotive applications, the prediction time horizon is in the range of 30sec -120 sec. For this case study, we chose 120 sec as the prediction time horizon to validate that the algorithm remains accurate at higher prediction horizons. The maximum safe current application considered is taken as 10C i.e. 26A for the cells. This value i.e. 10C is chosen as I_r in the MRG. The battery pack is simulated for a dynamic input current profile as shown in Fig. 4.6. Due to the heterogeneity considered, the state of the cells in the pack is different from one another. The voltage, SOC, and temperature of the individual cells of the pack are shown in Fig. 4.7. As the input cycle considered is an overall discharging cycle, the SOC and voltage have a generally decreasing trend. The SOP (charge and discharge)current, of the battery cells is shown in Fig.4.8 by solid lines, while the bounds of charge/discharge current obtained using reachability analysis are shown by dashed lines. It can be observed that the SOP charge current predicted has an increasing trend while the SOP discharge current has a decreasing trend. This is because the cells are going an overall discharging cycle as seen in Fig.4.7. Note that even though both upper and lower bounds of SOP current magnitudes are obtained in this process, the lower bound is what we use to define SOP. This is because according to the defined SOP for the pack, SOP is the maximum current that all the cells in a pack can sustain without violating any safety constraints. Hence the lower predicted bound will be the maximum safe current for the entire battery pack. The tightness of the lower bound prediction for SOP shows the preciseness of the algorithm.

Case 2: Grid application

The algorithm is also tested for the case of grid energy storage, where the prediction problem is scaled up by considering the large no of cells connected in a series-parallel arrangement. We use Tesla Powerwall [41], as the specification for the stationary energy storage system. The Powerwall also uses NMC chemistry, though the cell specification might be different. We
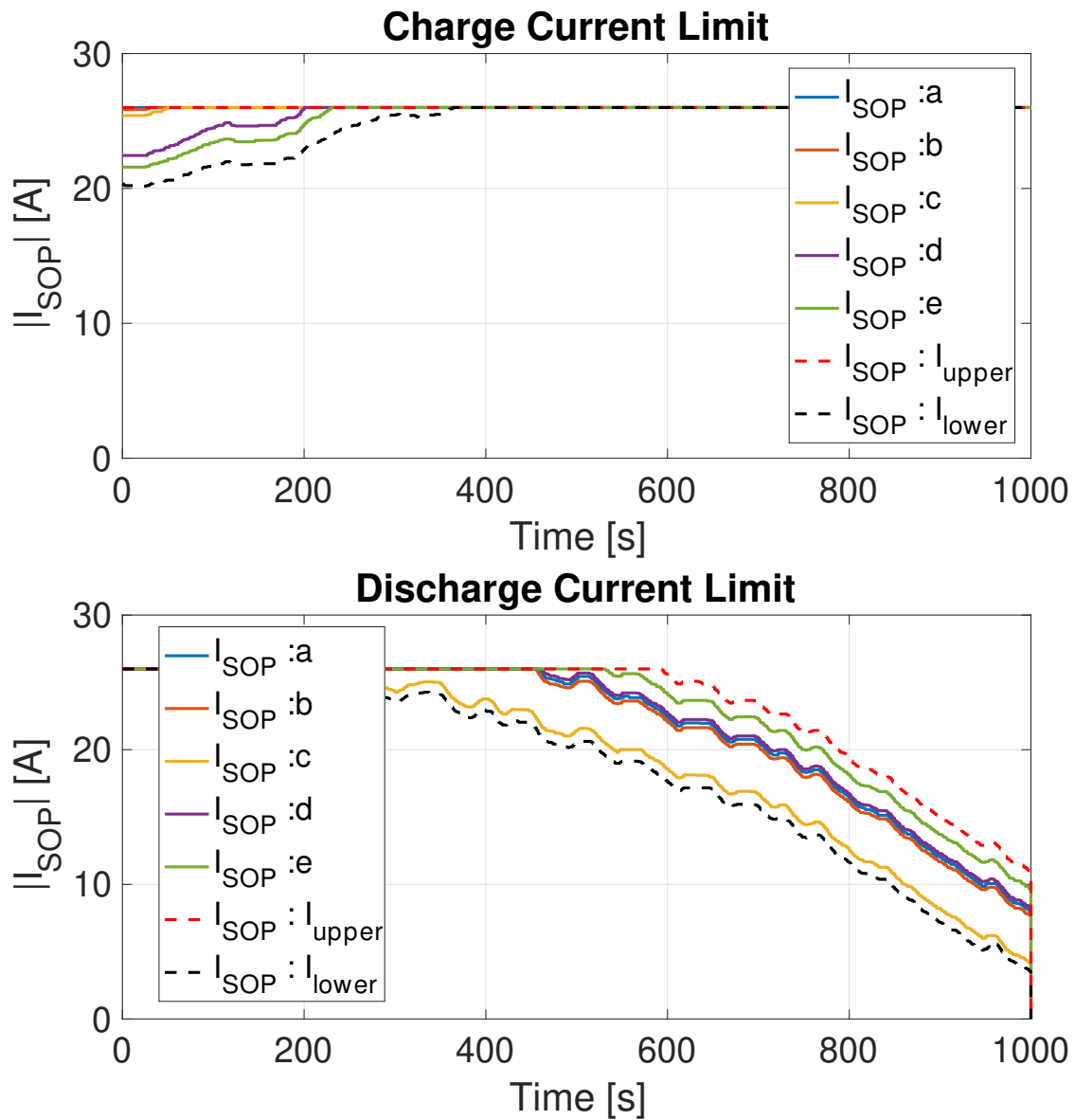
Figure 4.8: SOP: Charging and discharging current prediction

assume the Powerwall is made of the same 2.6Ah nominal capacity NMC cells, with similar
heterogeneity that we used in Case 1(HEV). Powerwall's energy capacity and internal battery
voltage are specified to be 13.5kWh and 50 V respectively. To meet this specification we
assume the powerwall to be made of 14 modules connected in series, where each module is
made up of 107 cells in parallel (14s107p, cell configuration). For the analysis, we assume

1 module (107p cells) as 1 unit and focus on the heterogeneity in the modules rather than
the cells. The parameters of the module are scaled considering 107 2.6Ah cells connected in
parallel [42]. As the study is for grid application, the prediction horizon is chosen in hours
rather than in seconds, as done for HEV. The problem hence scales to:

1. 14 modules/units in series

2. Module capacity : 278.2Ah (heterogeneous cells)

3. 1 hour prediction horizon
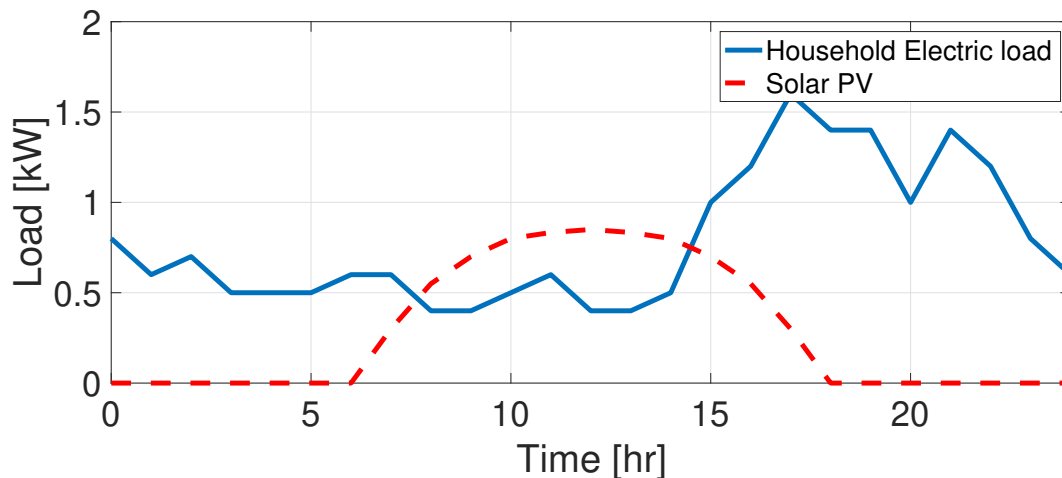
Figure 4.9: Household load and solar PV generation

The Powerwall study is done for a residential household load that has solar PV installed.
The load profile obtained is by using the household electric load data [43] and the solar PV
power production data for an average day for California [44]. Figure 4.9 shows the electric
load demand and PV electric generation considered. It is assumed the total overall load of the
household (household electric load – PV production) is sustained by the Powerwall. Given
the specification of the powerwall, Fig.4.10 shows the current profile that the powerwall will
undergo for the load profile shown in Fig.4.9. When solar PV produces electricity higher
than the energy consumption of the household, the Powerwall is charging, the rest of the
time the Powerwall discharges to sustain the electric demand of the household. Fig.4.11
shows the evolution of voltage SOC and temperature of the cells. As expected the SOC and
corresponding voltage of the cells increase whenever the Powerwall goes through a charging
current, and decreases when discharging. Fig.4.12 shows the corresponding SOP current
values obtained for the powerwall. The simulation study is done for the entire 24-hour load
profile. Solid lines show the SOP for individual modules while the red and black dashed lines
show the safety current bound for the entire Powerwall. The SOP current is defined by the
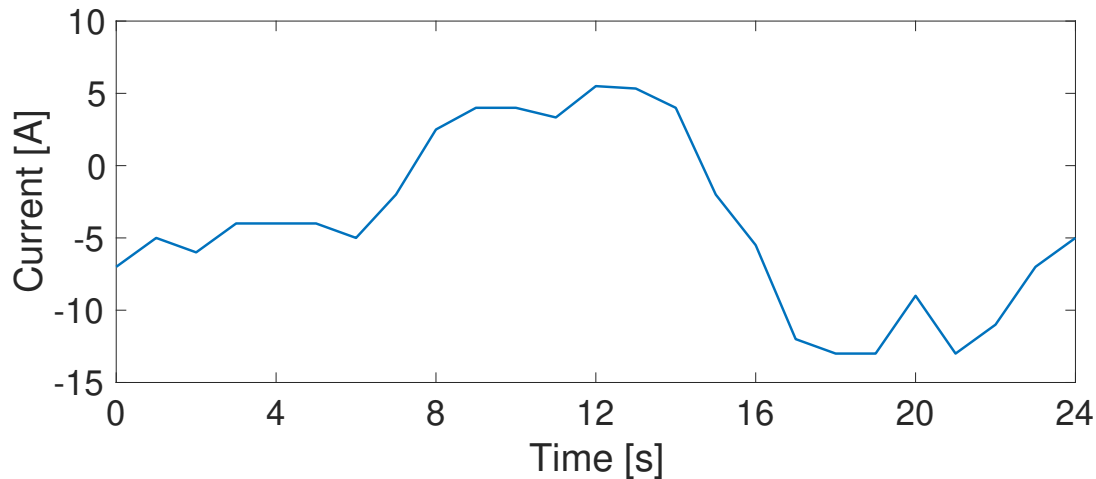
Figure 4.10: Current profile for Case 2 analysis

black dashed as that is the maximum current that the entire pack can sustain safely. It can be observed that the prediction of the lower bound i.e. SOP is accurate in this case as well, even with a large prediction horizon of 1 hour. This validates the robustness and accuracy of the algorithm across different cell parameters, numbers of cells, and prediction horizons.
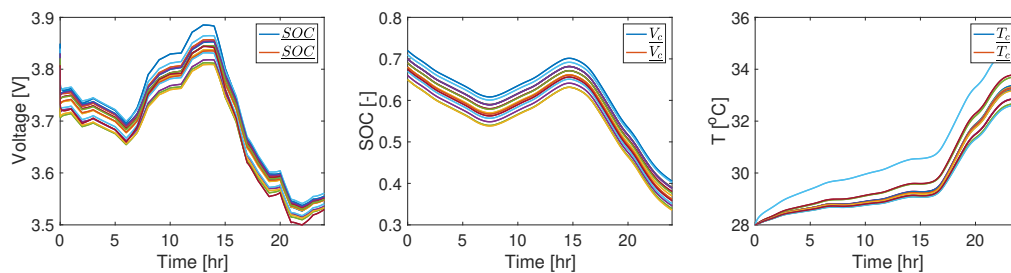
Figure 4.11: State and output profile for individual modules

4.6 CONCLUSIONS

The paper provides a methodology for SOP prediction for a battery pack consisting of heterogeneous cells. The problems related to SOP prediction are discussed in the paper and the shortcomings in the literature are highlighted. The focus of this work is SOP prediction for a pack-level system. The complexity of SOP prediction for a battery pack is solved using the concept of reachability analysis for the prediction of state intervals. Determining state

interval bounds that encompass the state of all the individual cells in a pack makes the algorithm scalable to any number of cells in a battery pack.

The battery cell in this study is modeled as ECM with two-state thermal dynamics. Heterogeneity within the cell is dealt by considering the battery as an uncertain parameter-varying system. Reachability analysis for state interval prediction is combined with a modified reference governor for estimating the SOP. The designed SOP algorithm is validated for two case studies i.e. a small HEV and a Tesla Powerwall storage. Both these applications were chosen as they are immensely different in terms of the number of cells in the pack and the prediction time horizon. The results show accurate SOP prediction in both the case study thereby validating the robustness of the algorithm.
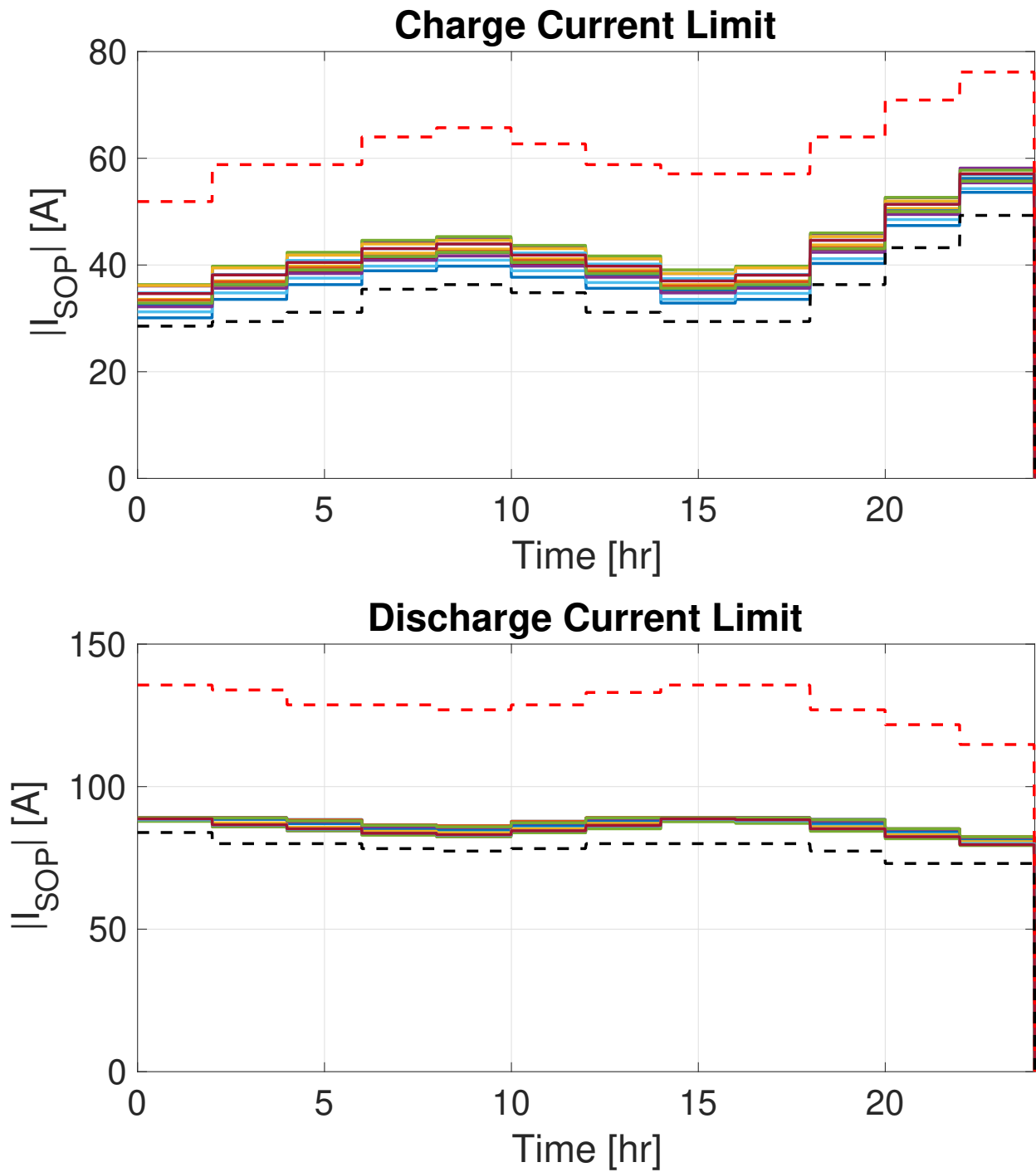
Figure 4.12: SOP: Charging and discharging current prediction for Grid battery pack

Chapter 5

Global Sensitivity Analysis of 0-D Lithium Sulfur Electrochemical Model

5.1 INTRODUCTION

With an increasing push for electrification, research on higher energy-density battery chemistry has gained momentum, especially in applications where energy density is critically important. Research on Lithium sulfur batteries has gained traction due to their high theoretical energy density, which is expected to be 2-3 times greater than current Li-ion batteries [3, 45]. The abundant supply and low cost of sulfur adds to the commercial interest in Li-S batteries. Even though the chemistry is promising due to higher energy densities, its commercialization is hindered by the limited utilization of sulfur, poor rate capability, self-discharge, and capacity degradation. Most of the research on Li-S batteries focuses on materials [46], chemical development, and understanding the reaction fundamentals [47, 48]. However, less work has been done to develop BMS systems based on mathematical models, including state and parameter estimation algorithms that monitor performance and health [3, 49, 50].

A key aspect in model development is parameter identification ([45]). In the case of Li-S, complex reaction mechanisms make both modeling and parameter identification a daunting challenge. Mathematical models with large numbers of parameters are generally associated with more complex parameter identification. In this regard, efforts are made on reducing model complexity, experimental identification of parameters, and investigating parameter sensitivities.

Sensitivity analysis uncovers the effect of parameters on model response. It guides parameter identification by revealing information about parameter relevance and interdependence, which helps in grouping and ordering the parameters during the identification process ([51]). It also provides help to optimally design experiments for parameter estimation.

The literature on parameter sensitivity analysis for Li-S batteries is limited. Ghaznavi and Chen, in a series of three papers, explore the sensitivity of parameters for a 1-D electrochemical model ([52]) with different set values of parameters. The study performed in these

three papers ([53–55]) can be used to optimally design the cell by understanding the influence of parameter values on cell performance. The parameter sampling technique in these works faces two major challenges. First, the parameters are varied one at a time and therefore do not capture the effect of parameter interaction on the output. Second, the parameters are sampled from an assumed set, which does not necessarily signify actual physical values of parameters. This motivates using techniques that explore the interaction of parameters and systematic sampling of parameter values, such as global sensitivity analysis. In ([56]) the authors study sensitivities of the model's diffusion coefficients and cathode thickness for different current rates. Similar to ([53–55]), sensitivity of parameters is evaluated by analysing the model response at different parameter values. Choosing parameters in this way can be insightful, however it is inherently heuristic in nature and does not systematically capture how the range of these set points affect the voltage response. The study in ([9]) investigated parameter sensitivity for a 0-D Li-S model, to identify significant parameters for parameter identification. The authors in this work use local sensitivity analysis (LSA) for identifying important parameters, which are then used for identification. A key challenge of an LSA based approach is the assumption on knowledge of 'nominal' parameter values. LSA suffers from a chicken and egg problem, where to identify the parameters you assume you have a reasonable estimate of the parameter values. This motivates the use of Global sensitivity techniques which don't assume initial point estimates on parameters, and instead only assume the parameters live within a range of values.

LSA and GSA differ by the kind of information they represent. LSA evaluates first order derivatives at a specific reference point in the parameter space. Therefore, changing the 'reference point' changes the information obtained from LSA. Despite being reference point dependent, LSA is used extensively in the literature ([51], [9]) because it provides qualitative, easily interpretable information which is also computationally cheap to evaluate. On the other hand, GSA measures the magnitude of influence a parameter has on model response. It is global in the sense that it evaluates the sensitivity over a given probability distribution on the parameter ([57]). The downside of using GSA is related computational cost, which increases exponentially as the number of parameters in the analysis increases. Even though GSA is considered 'global', because a range of parameters are considered in calculating sensitives, the sensitivities obtained depend on the choice of parameter distribution ([58]).

To address this challenge, we conduct a meta-sensitivity analysis on GSA under 3 parameter distributions to understand the way GSA sensitivities change as you change the parameter distribution. To this end, we perform sensitivity analysis on a 0-D electrochemical Li-S model ([59]). A global sensitivity evaluation method, the Sobol index ([58]), is used for analyzing parameter sensitivities. In this study, we are motivated to use GSA, firstly due to lack of experimentally validated nominal parameter values ([45]), and also to explore the interaction effect of parameters. We additionally recognize that the literature lacks a definitive set of possible physical values for Li-S model parameters. To this end, we performed sensitivity analysis for three different distributions of model parameters. This is done to examine the effect information about parameters *a-priori* has on its relative importance in parameter identification. To simplify, we focus on three model parameters. This study is

performed on 2 current profiles, to also emphasis the importance of experimental design on
parameter identification. The main contributions of this paper are:

1. Analysis of a 0-D lithium Sulfur battery model using global sensitivity analysis.

2. Analysis of Global sensitivity methods and their robustness to parameter distribu-
   tions. To the authors' knowledge, this is the first work that explores how parameter
   distributions change the results of global sensitivity analysis.

   The chapter is organized as follows. Section 5.2 introduces the 0-D electrochemical Li-
S model. Section 5.3 details the GSA technique and the different parameter distributions
considered in the study.Section 5.4 presents the results and details the comparative sensitivity
analysis of different parameter distributions. Finally, Section 5.5 provides conclusions for the
overall study.

5.2   Li-S Battery Model

This section summarizes a macro level electrochemical model, i.e. the zero-dimensional
Li-S model, developed in previous work ([59]) extended to a 3 step reaction model. The
model captures the fundamental redox reaction mechanisms happening at the cathode, while
disregarding the diffusion related transport phenomena. The anode is Li metal, and is
assumed to be an unlimited source of Li ions.

$$Li \longleftrightarrow Li^+ + e^- \tag{5.1}$$

The overpotential losses at the anode side are neglected, by assuming fast reaction kinetics
(5.1) ([60]). Any side reaction happening at the anode is neglected in this study. This is
done to simplify the model, and focus on the core reactions. During discharge the Li-metal
anode goes through an oxidation reaction, liberating Li-ions. The Li-ions move across the
electrolyte towards the cathode, where they react with the sulfur species and reduce into
different Li-polysulfide species. At the cathode, the elemental sulfur S_8^0 undergoes a series of
complex electrochemical reactions, forming different polysulfide species Li_2S_n ($1 \leq n \leq 8$),
starting from high order polysufides and finally reducing to low order sulfide Li_2S. The
high order polysufides are soluble in organic electrolytes, which causes shuttling of the high
order sulfide species between the cathode and anode. This parasitic 'shuttle' effect causes
self-discharge and degradation of the anode.

   The zero-dimensional model chosen for this study is a 3-step electrochemical reaction
given by:

$$\frac{3}{8}S_8^0 + e^- \longleftrightarrow \frac{1}{2}S_6^{2-}, \tag{5.2}$$

$$S_6^{2-} + e^- \longleftrightarrow \frac{3}{2}S_4^{2-}, \tag{5.3}$$

$$\frac{1}{6}S_4^{2-} + e^- \longleftrightarrow \frac{2}{3}S^{2-} \downarrow . \tag{5.4}$$

The lowest polysulfide i.e., S^{2-} further principates.The mass evolution of sulfur species is described by the following equations (5.5) -(5.9):

$$\dot{x}_1 = -\frac{3}{8}\frac{n_{S8}M_S}{n_eF}i_{H1}-k_sx_1, \tag{5.5}$$

$$\dot{x}_2 = \frac{1}{2}\frac{n_{S6}M_S}{n_eF}i_{H1}-k_sx_2-\frac{n_{S6}M_S}{n_eF}i_{H2}, \tag{5.6}$$

$$\dot{x}_3 = \frac{3}{2}\frac{n_{S4}M_S}{n_eF}i_{H2}-\frac{1}{6}\frac{n_{S4}M_S}{n_eF}i_L, \tag{5.7}$$

$$\dot{x}_4 = \frac{2}{3}\frac{n_SM_S}{n_eF}i_L-k_px_5(x_4-S^{2-}_*), \tag{5.8}$$

$$\dot{x}_5 = k_px_5(x_4-S^{2-}_*). \tag{5.9}$$

where states $[x_1, x_2, x_3, x_4, x_5]$ represent the mass of sulfur species $[S_8^0, S_6^{2-}, S_4^{2-}, S^{2-}, S_p]$ respectively. The shuttling effect of high order polysulfides i.e. S_8^0 and S_6^{2-} is modeled by using a shuttling constant k_s. The precipitation of S^{2-} is modeled using equation with a precipitation rate constant k_p.

The standard reduction potentials associated with the 3 reactions (5.2)-(5.4) can be modeled using Nernst equation given by equations (5.10)-(5.12).

$$E_{H1} = E_{H1}^0-\frac{RT}{F}\left(-\frac{3}{8}\ln\left(\frac{x_1}{n_SM_Sv}\right)+\frac{1}{2}\ln\left(\frac{x_2}{n_{S6}M_Sv}\right)\right), \tag{5.10}$$

$$E_{H2} = E_{H2}^0-\frac{RT}{F}\left(-\ln\left(\frac{x_2}{n_{S6}M_Sv}\right)+\frac{3}{2}\ln\left(\frac{x_3}{n_{S4}M_Sv}\right)\right), \tag{5.11}$$

$$E_L = E_L^0-\frac{RT}{F}\left(-\frac{1}{6}\ln\left(\frac{x_3}{n_{S4}M_Sv}\right)+\frac{2}{3}\ln\left(\frac{x_4}{n_SM_Sv}\right)\right). \tag{5.12}$$

The current associated with the 3 reactions (5.2)-(5.4) is modeled by using Butler-Volmer equations (5.13)-(5.15).

$$i_{H1} = -i_{H1}^0a_r$$
$$\cdot\left[\left(\frac{x_1}{x_1^0}\right)^{-\frac{3}{8}}\left(\frac{x_2}{x_2^0}\right)^{\frac{1}{2}}e^{\frac{F\eta_{H1}}{2RT}}-\left(\frac{x_1}{x_1^0}\right)^{\frac{3}{8}}\left(\frac{x_2}{x_2^0}\right)^{-\frac{1}{2}}e^{-\frac{F\eta_{H1}}{2RT}}\right] \tag{5.13}$$

$$i_{H2} = -i_{H2}^0a_r$$
$$\cdot\left[\left(\frac{x_2}{x_2^0}\right)^{-1}\left(\frac{x_3}{x_3^0}\right)^{\frac{3}{2}}e^{\frac{F\eta_{H2}}{2RT}}-\left(\frac{x_2}{x_2^0}\right)\left(\frac{x_3}{x_3^0}\right)^{-\frac{3}{2}}e^{-\frac{F\eta_{H2}}{2RT}}\right] \tag{5.14}$$

$$i_L = -i_L^0a_r$$
$$\cdot\left[\left(\frac{x_3}{x_3^0}\right)^{-\frac{1}{6}}\left(\frac{x_4}{x_4^0}\right)^{\frac{2}{3}}e^{\frac{F\eta_L}{2RT}}-\left(\frac{x_3}{x_3^0}\right)^{\frac{1}{6}}\left(\frac{x_4}{x_4^0}\right)^{-\frac{2}{3}}e^{-\frac{F\eta_L}{2RT}}\right] \tag{5.15}$$

The total current flowing in the battery is the sum of the current across the three reactions.

$$I = i_{H1} + i_{H2} + i_L. \tag{5.16}$$

The precipitated sulfide S_p reduces the active reaction area a_r, and is hence modeled as a function of the precipitated species as:

$$a_r = a_r^0 (1 - \omega \cdot x_5)^\gamma. \tag{5.17}$$

The output voltage is related to the standard reduction potential and overpotential of each of the three reactions.

$$\eta_i = V - E_i \tag{5.18}$$

where $i = \{H1, H2, L\}$. The equations above collectively form a differential algebraic equation (DAE) system, where (5.5)-(5.9) are the differential equations and (5.10)-(5.17) are the algebraic constraints of the system. The 0-D electrochemical DAE model chosen is of moderate fidelity and works well for low current discharge profiles. Because it has far fewer parameters and is computationally cheaper than a model like DFN ([61]), it is suitable for GSA.

Further information about model parameters can be found in ([59]).

5.3 Parameter Sensitivity

This section focuses on the parameter sensitivity information evaluated from GSA, for different parametric distributions.

In the 0-D model considered in this study, there are 11 model parameters in total. In this study we focus on 3 parameters due of the constraints on computational time required for GSA calculations. The parameters considered in the sensitivity analysis are: E_{H01}, i_{H01} and k_p.These 3 parameters are chosen in this study, as ranges of their respective distribution can vary significantly. This makes the analysis on the effect of parameter distribution in GSA interesting.

Global Sensitivity Analysis

GSA quantifies the variation of model response by varying the parameters along the entire parameter domain. A variance-based GSA tool, the Sobol index, is used in this study ([58]). The Sobol index is a measure of the percentage of variance in model output caused by a particular parameter and its interaction with other parameters. The variance in model output as a function of its parameter is decomposed as:

$$\text{var}(y(p)) = \sum_{i=1}^{n_p} \text{var}(y_i(p_i)) + \sum_{i<j}^{n_p} \text{var}(y_{ij}(p_i, p_j)) + \cdots$$
$$+ \text{var}(y_{1,2,\cdots,n_p}(p_1, p_2, \cdots, p_{n_p})) \tag{5.19}$$

where y is the model output, p_i is the ith model parameter, and n_p is the number of parameters in the model. Each term in the decomposition above is orthogonal and we assume model parameters are mutually independent. Next we define each term.

The first term in the decomposition is the output variance caused by parameter p_i alone and is calculated as:

$$\text{var}(y_i(p_i)) = \text{var}_{p_i}\left(\mathop{\mathbb{E}}_{p \sim i}(y \mid p_i)\right) \tag{5.20}$$

where the conditional expectation is taken over the joint distribution of random vector p, marginalized with respect to parameter i, and given p_i.

The second and the following terms capture the effect of varying parameters simultaneously, and are called second order interactions, and corresponding higher order interactions. These decomposed partial variances are normalized w.r.t. the total variance. This is termed as the corresponding Sobol index. In this study, we use the 1st order Sobol index, defined in (5.21) for analysing the independent effect of parameters on the model response.

$$S_{1,i} = \frac{\text{var}(y_i(p_i))}{\text{var}(y)} \tag{5.21}$$

In this study we use the Sobol index for analyzing global sensitivities of 3 parameters: E_{H1}^0, i_{H1}^0 and k_p.

Sobol Implementation

To compute the Sobol indices we conduct a Monte Carlo analysis. We use `CasADi` ([62]) to simulate the model and voltage response for parameters sampled randomly from the three distributions. Sobol' sequence ([63]) is used to efficiently generate parameter samples. We then use the package `SALib` ([64]) to compute Sobol indices over these simulations. We run 512 Monte Carlo simulations for each parameter distribution.

We analyze the global sensitives under 3 different parametric distributions, defined in Table 5.1.

Table 5.1: Distribution of parameters

Param.	Distribution 1	Distribution 2	Distribution 3
E_{H1}^0	5% (Uniform)	5% (Uniform)	5% (Uniform)
i_{H1}^0	5% (Uniform)	20% (Uniform)	1 order (Log-norm)
k_p	5% (Uniform)	20% (Uniform)	2 order (Log-norm)

The parameter distributions analyzed are either uniform or lognormal. All three distribution sets consider a 5% variation in E_{H1}^0 only because the standard reduction potential varies due to non-ideal solvent interactions only within a limited range, as consistent with variations observed in literature ([8, 9]). The other parameters i_{H1}^0 and k_p, however, do not
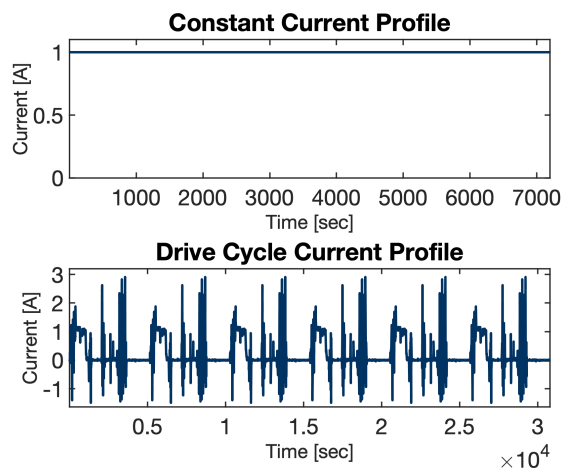
Figure 5.1: Input current profiles

have a defined nominal range of values. In literature, the estimated values of these parameters vary by 1 or 2 orders of magnitude ([8, 9]). Hence these 3 parameter distribution sets are considered in the analysis, with different degrees of parametric variation.

5.4 Results

In this section we analyze the results of GSA for the following input profiles plotted in Fig. 5.1:

- 1A constant current (C/3) discharge

- A dynamic current input

For each current profile, we show the GSA results for the 3 model parameters $\{E_{H01}, i_{H01}, k_p\}$ and 3 probability distributions on those parameters. For each parameter distribution set (Table 5.1), we also analyze the resulting distribution on the state trajectory. GSA on the first parameter distribution set, is qualitatively close to LSA, since the distribution is relatively narrow. We use 1st order Sobol indices as a measure of parameter sensitives. We find that, for certain parameters, the 1st order Sobol indicies are strongly impacted by the parameter distribution.

Constant Current Analysis

Figure 5.2 shows the output voltage distribution for constant current discharge for 3 different distributions, plotted is the respective subplots. The blue and yellow lines represent the mean voltage and its corresponding plus/minus one standard deviation, respectively, for

each distribution. We observe that voltage variance is large in the first 3000 seconds for all distribution sets, and distribution set 3 specifically shows higher variation after 4500 seconds. The model remains relatively insensitive between 3500-4500 seconds across all three parameter distributions.
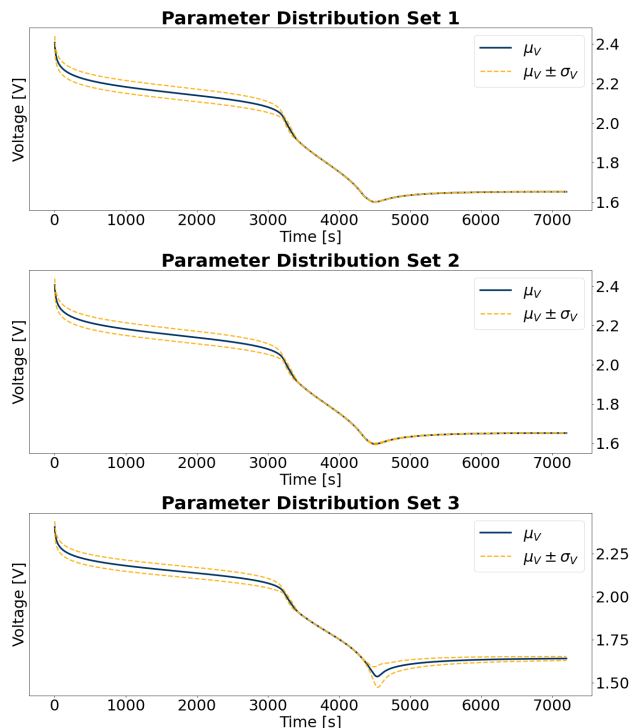
Figure 5.2: Voltage response for the 3 parameter distribution sets at constant current

Sobol indicies for the constant current input are shown in Fig 5.3. Observe that for all the distributions, parameter E_{H1}^0 remains sensitive in the initial 4000 seconds, while parameter k_p only becomes significant in the latter part of the profile. It is also interesting that parameter i_{H1}^0 has very low sensitivity for distribution set 1 and 2, while for distribution set 3 its sensitivity increases. The explanation for greater variance for distribution set 3 after 4500 seconds, and corresponding sensitivity profiles, can be inferred by analyzing the state evolution of sulfur species in Fig. 5.4. The figure shows the evolution of sulfur species for 1A constant current for the three parameter distributions.

The solid and the dotted lines in the figure denote mean and min/max evolution of the sulfur species using the parameters from the three distribution sets. It should be noted that the plots of species in the figure are normalized by maximum of each state over all three distributions. These normalizing constants are shown in table 5.2. Note that species S_8 and S_6, which are affected by parameters E_{H1}^0 and i_{H1}^0 according to (5.10) and (5.13), are only present in the initial 4000 secs. Once S_8 is exhausted around 3000 sec and S_6 starts decreasing, the variance caused by parameter E_{H1}^0 on model output decreases significantly.
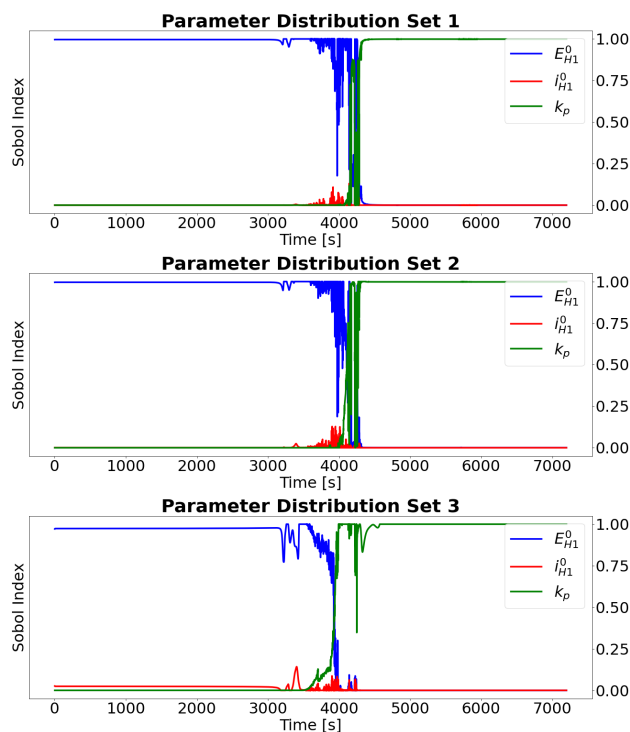
Figure 5.3: 1st order Sobol index for each parameter E_{H1}^0, i_{H1}^0, k_p, under each distribution set in Table 5.1.

Table 5.2: Normalizing constants for state plots

States	Constant Current	Drive cycle Current
x_1	2.97	2.97
x_2	2.54	2.38
x_3	2.95	1.24
x_4	0.027	4.46e-05
x_5	0.604	3e-05

As S_8 is depleted, reaction 1 is no longer a prevalent reaction, thereby (5.10) and (5.13) cease to affect voltage output.

The parameter sensitivities visualized in Fig. 5.3 highlight the relevance of parameters in different parts of the profiles. Note that after 3000 seconds, the noise in the Sobol index of E_{H1}^0 and i_{H1}^0 becomes greater, yet the variance in voltage output correspondingly decreases significantly (Fig. 5.2). This can also be understood from Fig. 5.4, where for all 3 distributions, the variation in state evolution between 3000-4500 sec becomes small.

The difference in sensitivity magnitude observed in Fig. 5.3 shows that for distribution
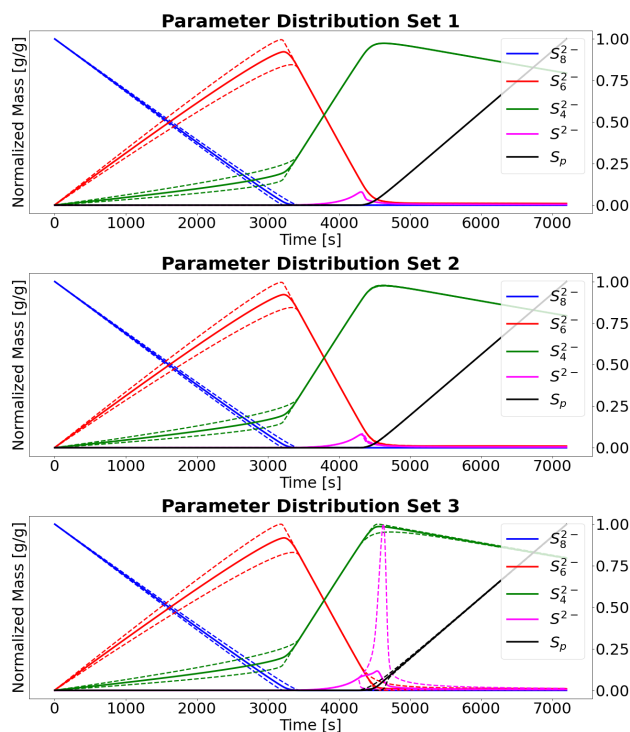
Figure 5.4: Max, min, and mean evolution of states (mass of sulfur species) for constant current.

set 1 and 2, the parameter i^0_{H1} remains relatively insignificant. Namely, most of the variance in output during the initial 4000 sec is dominated by E^0_{H1}. Only in distribution set 3, with a lognormal distribution on parameter i^0_{H1}, does its sensitivity increase to a detectable level.

Figure 5.3 shows that parameter k_p is the only significant parameter after 4000 sec, in all three distribution sets. This is because k_p affects the state evolution of S^{2-} and S_p, which are only present after 4000 seconds, as seen in Fig. 5.4. Even though k_p is the only significant parameter in the later half of the profile, the variance in output caused by k_p is significantly higher in distribution set 3, as seen in Fig. 5.2. Figure 5.4 further shows the variance in evolution of S^{2-} and S_p under different distribution sets. Notice that with a much larger parametric range in set 3, k_p significantly affects the evolution of S^{2-} and S_p. This elucidates how different parametric distributions can significantly affect the states, voltage output, and their corresponding sensitivities.

Dynamic Cycle Analysis

Next we analyse the sensitivity results for a dynamic input current representing a naturalistic drive cycle ([65]). We append multiple copies of this drive cycle normalized to discharge 2Ah of absolute current throughput. From Fig. 5.5 and Fig. 5.7, the distribution of parameters does not have a noticeable impact on the variation of voltage or state trajectories. As such,
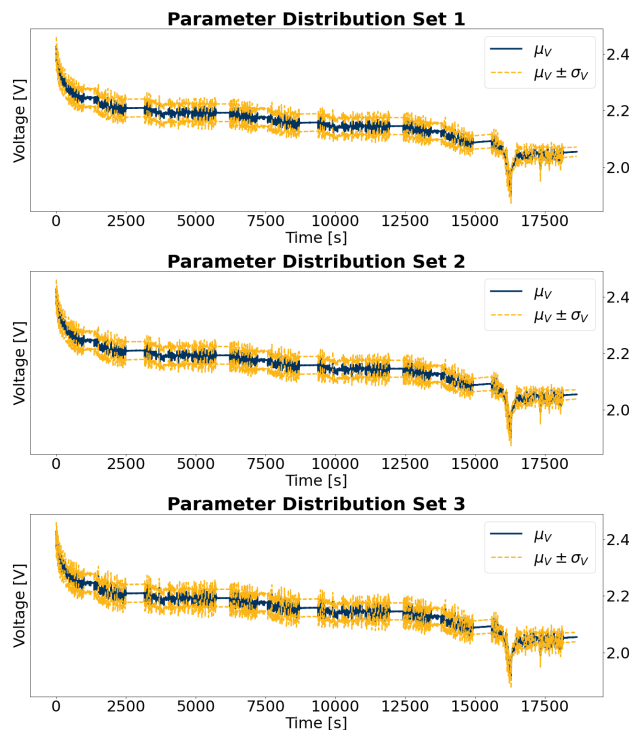
Figure 5.5: Voltage for the 3 parameter distributions for dynamic current input.

we focus our attention on Fig. 5.6 which does show a noticeable trend with distribution.

The sensitivity profiles for dynamic current input are displayed in Fig. 5.6. The most significant parameter in this profile is E_{H1}^0, across all distribution sets. Notice also that with an increased parametric range for i_{H1}^0, its sensitivity i.e. variation in voltage caused by i_{H1}^0 increases. For distribution set 3, i_{H1}^0 has a larger Sobol index, and can become a significant parameter. This information is relevant in application, since it implies that i_{H1}^0 can be significant if its range of variation is properly chosen. In contrast, even by increasing the range k_p's distribution by two orders of magnitude, its sensitivity remains small. This can be explained by looking at the state evolution of species in Fig. 5.7. Species S^{2-} and S_p remain neglible for most of the dive cycle. Thus the effect of k_p on voltage output remains negligible. This implies that for any distribution, k_p would have very low identifiability for this input profile.

In both case studies, we observe that E_{H1}^0 is a significant parameter across all the distribution sets. However, the significance of parameter i_{H1}^0 and k_p showed dependency on their distribution. It is also notable that parameter identifiability depends greatly on the input profile. In case study 1, E_{H1}^0 and k_p are the parameters significantly affecting voltage response, while i_{H1}^0 remains relatively insignificant, across all distributions. In case study 2, i_{H1}^0 becomes an important parameter, affecting the voltage response (for distribution 3), while k_p remains insignificant.
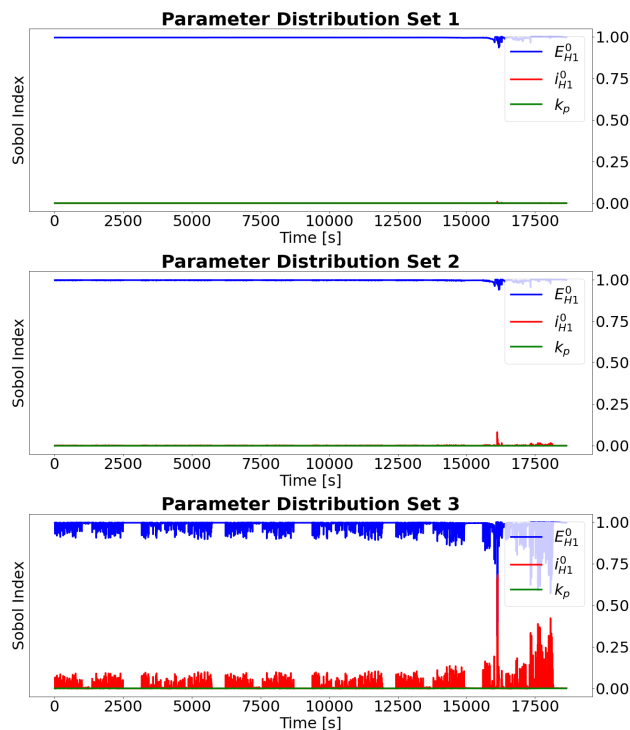
Figure 5.6: First order Sobol index for Dynamic current

This analysis demonstrates the importance of analyzing parametric sensitivity when selecting an input profile for parameter identification. It also highlights the effect that the range of parameters has when performing sensitivity analysis. Techniques like LSA, where sensitivity is highly dependent on choice of nominal value, can lead to misleading information about parameter importance. Analogously, with GSA, the range of parameter variation needs to be properly considered.

5.5 Conclusion

This chapter conducts a meta-analysis on global sensitivity of Li-S model parameters, analyzing its dependence on various parameter distributions. Two cases studies are presented, where sensitivities of three parameters are analyzed under three distribution sets. We observe that *a-priori* information about a parameter has a significant impact on its relative importance for identification. The input profile, as well as the parameter distribution, affect the impact a parameter has on voltage response.

Sensitivity analysis facilitates experimental design for effective parameter identification. This work lays the groundwork for optimal experiment design using GSA. Importantly, we discover that optimal experiments designed using conventional GSA are not robust to the
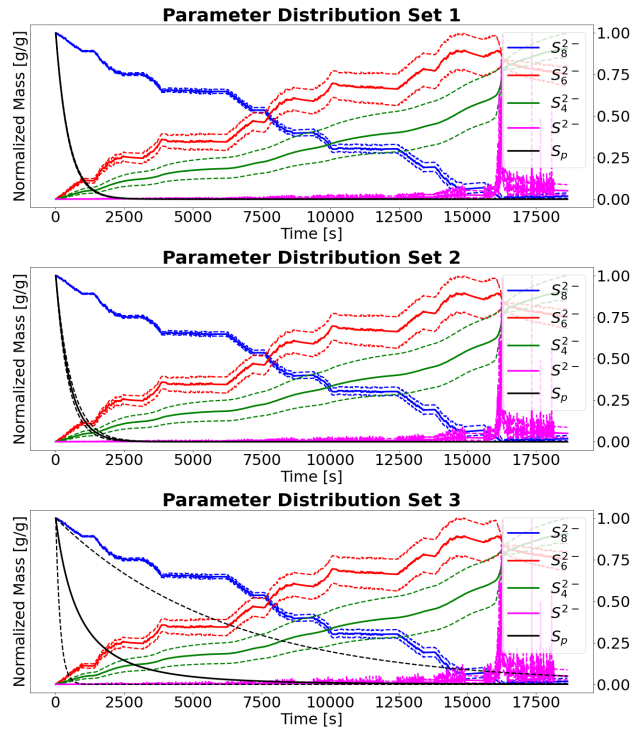
Figure 5.7: State evolutions for Dynamic current

distribution chosen on the parameters. This motivates future work in distributionally robust optimal experiment design.

Chapter 6

Physics informed Neural network modeling of state estimation of Lithium Sulfur batteries

6.1 INTRODUCTION

Recent research in the next generation of battery technologies gives hope to the development of high energy-dense and cheaper alternatives to lithium-ion batteries in the next decade. One promising alternative, lithium-sulfur (Li-S) batteries, has garnered attention due to their high theoretical energy density of 2500 Wh, making it appealing for applications where space and weight constraints are critical, such as in electric vehicles and portable electronics. Additionally, sulfur is an abundant, environment-friendly, and low-cost element, which makes Li-S batteries potentially more cost-effective and eco-friendly than lithium-ion batteries. The commercial, economic, and environmental benefits associated with Li-S batteries are significant motivations for researching Li-S batteries.

Despite the theoretical advantages, Li-S battery chemistry currently has a lot of challenges in practical applicability. The main challenges in its practical scalability are low cycle life, poor stability of both cathode and Li metal anodes, low coulombic efficiency, poor rate capability, limited sulfur utilization, and self-discharge. A lot of ongoing research is being done in the field of material development, electrode design, cell design, and electrolyte synthesis to overcome these challenges. Along with these research efforts, it is crucial to focus on its modeling and estimation challenges. To meet the demands of any commercial application, an accurate battery management system (BMS) to monitor the state and health of the battery is essential. Work done on the development of efficient BMS algorithms for Li-S batteries is limited.

The main challenge in the modeling and estimation of LiS battery is associated to the complex reaction kinetics at the cathode. In a typical Li-ion battery, the reaction at the anode and cathode can be summed by a single-step oxidation/reduction reaction. On the

other hand, in a LiS battery, both during charge and discharge the sulfur species undergoes a multistep electrochemical reaction [8], resulting in different polysulfide species. Estimating the evolution of different polysulfides adds to the modeling/estimation complexity.

The dynamics of LiS battery, even with a 1-D electrochemical model [52] results in a complex nonlinear differential algebraic equation (DAE) system that makes state estimation challenging. The numerical stability of both the model and observer becomes very sensitive to any noise in state estimates. The state estimation for Li-S is further challenged, due to its flat voltage vs capacity curve, making it a locally weak observable system.

Most model and estimation work for Li-S batteries is focused on either empirical-based equivalent circuit models (ECM's) or electrochemical models. The more simplified ECMs are widely used for BMS applications due to their simple architecture and computational efficiency. ECMs architecture for Li-S modeling and estimation are well explored in literature [3, 66]. ECMs however, do not provide any insight about the physical states or the electrochemical process happening in the battery. Furthermore, Li-S batteries exhibit self-discharging behavior due to the "shuttle effect", which is not modeled in the ECMs [66] and consequently makes methods like Coulomb counting inaccurate for SOC estimation [67]. The higher fidelity physics-based electrochemical model on the other hand provides insight into the physical phenomena happening in the battery.

Depending on the physical scales, EM Li-S models in the literature range from atomic-level DFT simulations to micro-particle level kinetics, to bulk macroscale cell-level models. Although the high-fidelity, first principal models provide insight into the physical phenomena happening in the battery, their application to BMS is limited due to their high mathematical complexity and computational costs. Even for Li-ion batteries, EM-based estimation algorithms (e.g., for the DFN model) are already challenging due to the partial differential equation architecture of the model. This challenge is further exacerbated for Li-S batteries because of complex reaction pathways, shuttle effect, and precipitation of sulfides. The electrochemical models and related estimation algorithm for Li-S battery is not as mature as for Li-ion batteries [3]. EM-based estimation methods for Li-S battery are focused around zero-dimensional models [9].

In [9] Xu reduced the 0D- DAE model to an ODE model, which was then used for state estimation using the unscented Kalman filter (UKF). The ODE framework allows for the implementation of common estimation techniques e.g., UKF, EKF, etc. However, the resulting ODE model in [9] has a very stiff structure, which makes implementing EKF infeasible and causes numerical stability in UKF due to possible infeasible sigma point generation. In [67], state estimation on the 0D-DAE model was done using EKF. Even though the algorithm shows good performance, the DAE-EKF structure in [67] involves solving algebraic equations at every step making it computationally intensive.

In this work, we propose a physics-informed neural network model architecture that replicates the 0-D DAE model. The proposed model addresses the challenges associated with neural stability and state estimation of the DAE model. In our preliminary work [68], a piecewise affine (PWA) model was explored that approximates that well approximates the discharge DAE model. The PWA structure in [68] was further integrated with moving

horizon estimation (MHE) for state estimation. The work explored [68] was limited to
discharge profiles and the resulting PWA-MHE estimator although resulted in a near-optimal
solution, was computationally expensive. In this work, we address the limitations in [68].
The main contributions of this work are summarized as follows:

- The physics-informed neural network model architecture is used to capture the elec-
trochemical dynamic of the Li-S battery.

- The model estimates a diverse range of charging and discharging profiles accurately.
Most literature in Li-S is limited to replicating the discharge performance [8, 9].

- Moving horizon estimation is used for state estimation of the Li-S neural network model
for accurate state estimation. The accuracy of the MHE state estimator is compared
with EKF.

This chapter is organized as follows. In section 6.2, we first introduce the 0-D electro-
chemical model used as the baseline to simulate the dynamics of a Li-S battery cell. Section
6.3 describes the neural network model building for this study. The architecture of the model
and the data used in training are detailed, and the accuracy of model fit is discussed. In
Section 6.4 state estimation the moving horizon framework used for state estimation is de-
scribed. Section 6.5, presents the results of state estimation by MHE and compares it with
EKF. Finally section 6.6 concludes this study.

6.2 Li-S Electrochemical Model

This section summarizes the DAE model used as the ground truth model in this study. The
model chosen is a three-step zero-dimensional model developed in the previous work [67].
The Li-S battery exhibits a distinctive voltage curve. During discharge, the voltage curve
has two distinct voltage plateaus and a voltage dip in between. The voltage profile during
charging for Li-S is quite different from the discharge profile, showing high hysteresis. Figure
6.1 shows the typical voltage curve for Li-S battery during low current charge and discharge.

The 3-step 0-D model chosen captures the characteristic voltage curve of the Li-S battery
both during charge and discharge. The model well captures the reaction kinetics, while
the transport dynamics are ignored. At fully charged conditions, the cathode consists of
elemental sulfur S_8^0. During discharge, the sulfur species present at the cathode undergoes
a series of electrochemical reactions and gets reduced to different polysulfide species. The
three-step reactions at the cathode associated with the model are:
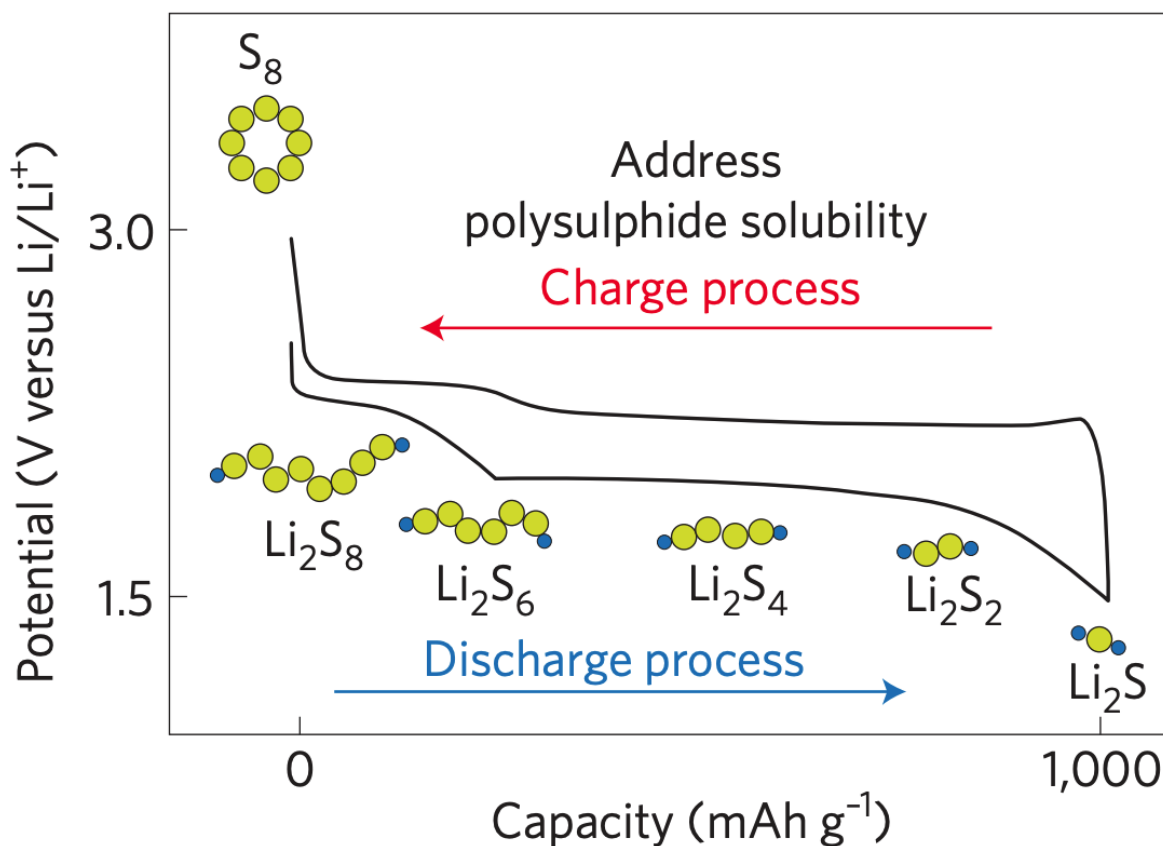
Figure 6.1: LiS: Charge and Discharge profile taken from [69]

$$\frac{3}{8}S_8^0 + e^- \longleftrightarrow \frac{1}{2}S_6^{2-}, \tag{6.1}$$

$$S_6^{2-} + e^- \longleftrightarrow \frac{3}{2}S_4^{2-}, \tag{6.2}$$

$$\frac{1}{6}S_4^{2-} + e^- \longleftrightarrow \frac{2}{3}S^{2-} \downarrow. \tag{6.3}$$

The high order polysulfide S_8^0 and S_6^{2-} are soluble in the organic electrolytes and move towards the anode, causing the infamous "shuttle effect". The low polysulfides S^{2-} on the other hand is insoluble and precipitates represented by $\downarrow$ in (6.3).

The evolution of sulfur species is described by the following equations:

$$\dot{x}_1 = -\frac{3}{8}\frac{n_{S8}M_S}{n_eF}i_{H1} - k_sx_1, \tag{6.4}$$

$$\dot{x}_2 = \frac{1}{2}\frac{n_{S6}M_S}{n_eF}i_{H1} - k_sx_2 - \frac{n_{S6}M_S}{n_eF}i_{H2}, \tag{6.5}$$

$$\dot{x}_3 = \frac{3}{2}\frac{n_{S4}M_S}{n_eF}i_{H2} - \frac{1}{6}\frac{n_{S4}M_S}{n_eF}i_L, \tag{6.6}$$

$$\dot{x}_4 = \frac{2}{3}\frac{n_SM_S}{n_eF}i_L - k_px_5(x_4 - S_*^{2-}), \tag{6.7}$$

$$\dot{x}_5 = k_px_5(x_4 - S_*^{2-}). \tag{6.8}$$

where $[x_1, x_2, x_3, x_4, x_5]$ denote the mass of sulfur species $[S_8^0, S_6^{2-}, S_4^{2-}, S^{2-}, S_p]$ respectively. S_p denotes the mass of precipitated sulfur. The shuttle of higher order polysulfides is modeled by in k_s in (6.4)-(6.5) and the precipitation of S^{2-} is modeled in (6.7) using precipitation rate constant. The current i_{H1}, i_{H2}, i_L in (6.4)-(6.7) represent the current involved in each electrochemical reaction and is modeled using Butler-Volmer kinetics as:

$$i_{H1} = -i_{H1}^0 a_r$$
$$\cdot \left[\left(\frac{x_1}{x_1^0}\right)^{-\frac{3}{8}}\left(\frac{x_2}{x_2^0}\right)^{\frac{1}{2}}e^{\frac{F\eta_{H1}}{2RT}} - \left(\frac{x_1}{x_1^0}\right)^{\frac{3}{8}}\left(\frac{x_2}{x_2^0}\right)^{-\frac{1}{2}}e^{-\frac{F\eta_{H1}}{2RT}}\right] \tag{6.9}$$

$$i_{H2} = -i_{H2}^0 a_r$$
$$\cdot \left[\left(\frac{x_2}{x_2^0}\right)^{-1}\left(\frac{x_3}{x_3^0}\right)^{\frac{3}{2}}e^{\frac{F\eta_{H2}}{2RT}} - \left(\frac{x_2}{x_2^0}\right)\left(\frac{x_3}{x_3^0}\right)^{-\frac{3}{2}}e^{-\frac{F\eta_{H2}}{2RT}}\right] \tag{6.10}$$

$$i_L = -i_L^0 a_r$$
$$\cdot \left[\left(\frac{x_3}{x_3^0}\right)^{-\frac{1}{6}}\left(\frac{x_4}{x_4^0}\right)^{\frac{2}{3}}e^{\frac{F\eta_L}{2RT}} - \left(\frac{x_3}{x_3^0}\right)^{\frac{1}{6}}\left(\frac{x_4}{x_4^0}\right)^{-\frac{2}{3}}e^{-\frac{F\eta_L}{2RT}}\right] \tag{6.11}$$

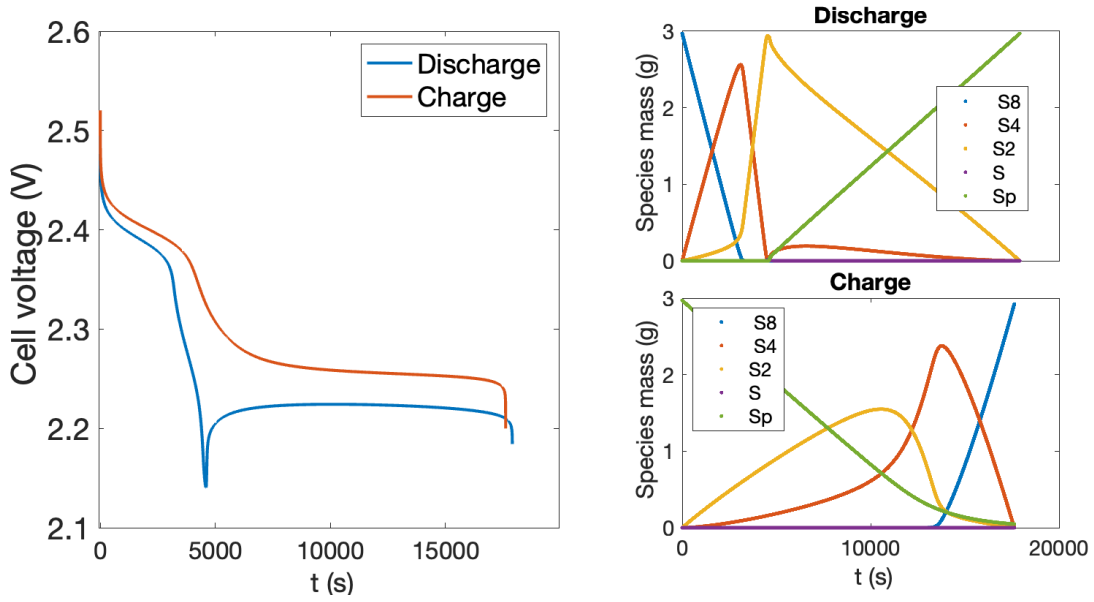The term a_r in (6.9)-(6.11) is the active reaction area, which is affected by the evolution of precipitated sulfide S_p and is modeled as:

$$a_r = a_r^0(1 - \omega \cdot x_5)^\gamma. \tag{6.12}$$

The total current flowing in the battery, which is the measured cell current is the sum of current associated with each reaction i_j

$$I = i_{H1} + i_{H2} + i_L. \tag{6.13}$$

where $i = \{H1, H2, L\}$.

Figure 6.2: DAE charge and Discharge voltage and state evolution

The overpotential term n_j of each reaction relates the output voltage and standard reduction potential of each reaction.

$$\eta_i = V - E_i \tag{6.14}$$

The standard reaction potential of each reaction is further modeled using the Nernst equation

The standard reduction potentials associated with the 3 reactions (6.1)-(6.3) can be modeled using the Nernst equation given by equations (6.15)-(6.17).

$$E_{H1} = E_{H1}^0 - \frac{RT}{F}\left(-\frac{3}{8}\ln\left(\frac{x_1}{n_S M_S v}\right) + \frac{1}{2}\ln\left(\frac{x_2}{n_{S6} M_S v}\right)\right), \tag{6.15}$$

$$E_{H2} = E_{H2}^0 - \frac{RT}{F}\left(-\ln\left(\frac{x_2}{n_{S6} M_S v}\right) + \frac{3}{2}\ln\left(\frac{x_3}{n_{S4} M_S v}\right)\right), \tag{6.16}$$

$$E_L = E_L^0 - \frac{RT}{F}\left(-\frac{1}{6}\ln\left(\frac{x_3}{n_{S4} M_S v}\right) + \frac{2}{3}\ln\left(\frac{x_4}{n_S M_S v}\right)\right). \tag{6.17}$$

The equations above collectively form a differential algebraic equation (DAE) system, where (6.4)-(6.7) are the differential equations and (6.9)-(6.17) are the algebraic constraints of the system. The only measurable variable in the model is the input current I and the voltage output V.

Figure 6.2 shows the model voltage and state evolution for 1A charge and discharge currents for a cell with 3.0 gm of total active sulfur.

6.3 Neural Net Model Architecture

The DAE model described in section 6.2 is approximated by the neural network to model both state and voltage dynamics. Typically neural networks are used as a black box model to capture input out dynamics, but they do not capture the underlying physical mechanism. In this work we integrate the governing state reaction kinetics into the neural network framework, to develop a physically interpretable, physics-consistent model. We reduce the DAE model to a numerically stable neural net (NN) model, which can be easily used to develop a state estimation algorithm.

The typical structure of the DAE model is:

$$
\begin{aligned}
\dot{x} &= f(x, z, u) \\
0 &= g(x, z, u) \\
y &= h(x, z, u)
\end{aligned}
\tag{6.18}
$$

The NN model is used to transform the above DAE dynamics to the following discrete equation:

$$
\begin{aligned}
x(t{+}1) &= f_{NN}(x(t), u(t)) \\
y(t) &= h_{NN}(x(t), u(t))
\end{aligned}
\tag{6.19}
$$

In this work, the NN model consists of two neural networks. i.e., the state neural network and the output neural network. The State neural network is used to capture the evolution of different polysulfide species while the output neural network is used to capture the voltage dynamics. Figure 6.3 shows the overall architecture of the model.

The above architecture in Fig .6.3 helps in providing insight into the physical states of the battery, i.e., the mass of sulfur species.

Data Preparation

For training the State NN and the output NN, different constant current discharge and charge profiles are used. The following 12 profiles dataset is used to train the model.

- Discharge constant current profiles with the following current magnitudes: [0.2, 0.5, 1, 1.5, 2, 3, 4]

- Charge constant current profiles with the following current magnitudes: [-3, -2, -1, -0.5, -0.1]

Both state and output NN are trained separately. The state and output voltage trajectories obtained from the DAE model are used to train the State NN and output NN. In this work, we model the battery state $x(t)$ as the normalized mass of sulfur species, i.e.

$$
x_i(t) = \frac{\text{Mass of } i^{th} \text{ Sulfur Species}}{\text{Total mass of active sulfur}}
$$
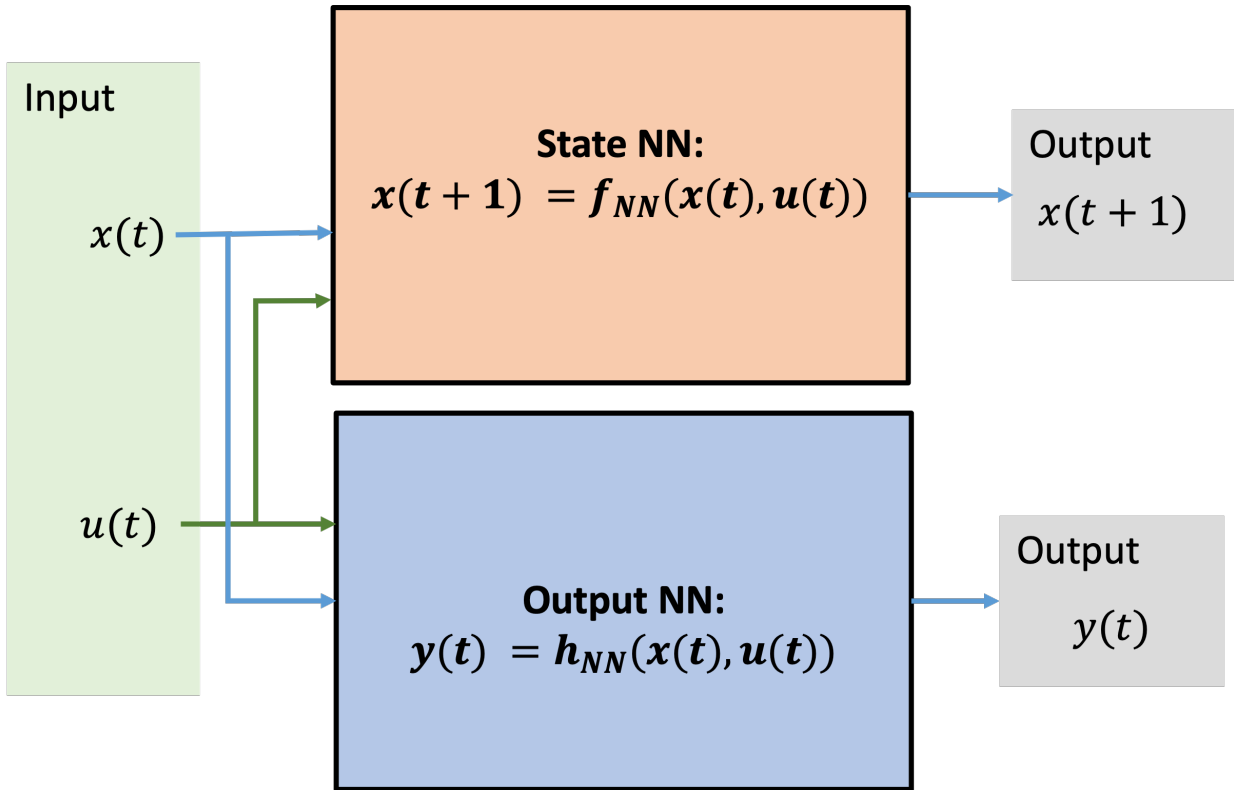
Figure 6.3: Neural Network Model

This is done for ease of interpretation of results.

State Neural Network

The state model developed here is a neural network model, that exploits the physical constraints of the state to develop a physics consistent model. The following are the physical constraints in the values the state can have:

- Sulfur species mass cannot be negative, i.e., $x(t) \geq 0 \quad \forall t \geq 0$

- Mass of sulfur species is conserved, i.e., $\sum_{i=1}^{5} x_i = 1$

The neural net state function f_{NN} is obtained by fitting the state trajectories of the training data. The state model predicts the next state $x(t+1)$ of the battery given the present state i.e., $x(t)$ and current input $I(t)$.

To ensure that the physical constraints of the system are followed, we filter the output of the neural network model as follows:

$$x\left(t+1\right) = \frac{ReLU\left(\ x\left(t+1\right)\ \right)}{\sum_{i=1}^{5}\left(ReLU\left(x_i\left(t+1\right)\right)\right)} \tag{6.20}$$

- ReLU function is used to ensure that states remain in a non-negative orthant. $ReLU\left(\ y\ \right) = \max\left(0, y\right)$

- Normalizing the $\frac{ReLU\left(\ x(t+1)\ \right)}{\sum_{i=1}^{5}\left(ReLU\left(x_i(t+1)\right)\right)}$ is done to ensure normalized states sum to one, i.e., $\sum_{i=1}^{5} x_i = 1$

The state NN $\left(f_{NN}\right)$ is approximated by a Feed-forward neural network (FNN) with 3 hidden layers with thirty nodes in each layer. Rectified linear unit (ReLU) is used as an activation function in each layer. The inputs to the state NN are $x(t)$ and $I(t)$ and the output is state at $x(t+1)$.

Output Neural Network

The output NN $\left(h_{NN}\right)$ is approximated by an FNN with 3 hidden layers with fifty nodes in each layer. Rectified linear unit (ReLU) is used as an activation function in each layer. The inputs to the output NN are the $x(t)$ and $I(t)$ output is the voltage estimate $y(t)$.

Figure 6.4 shows the fitting of the state NN for different training discharge and charge current profiles. The black solid line shows the ground truth DAE states and the dotted colored results show the states estimated from the trained state neural network. It can be observed that state NN estimates both the discharge and charge state trajectories of the DAE model.

Similarly, Fig. 6.5 shows the fitting of the output NN for different training discharge and charge current profiles. The black solid line shows the ground truth DAE voltage output, and the red dotted line shows the voltage output from the trained output neural network. The output NN accurately estimates the DAE voltage output for a range of charge and discharge profiles. The characteristic discharge voltage curve of Li-S, with two distinct plateaus and the voltage dip, is also well approximated.

Table 6.1, summarizes the error in state NN and output NN training, over all the 12 training profiles mention in section 6.3.

Table 6.1: Neural Net fitting

Neural Net	Error Calculation	Value
State	$\sum_{m=1}^{12}\sum_{t=0}^{T_{end}}\left\|\left\|x_{m,NN}\left(t\right) - x_{m,DAE}\left(t\right)\right\|\right\|^2$	0.0158
Output	$\sum_{m=1}^{12}\sum_{t=0}^{T_{end}}\left\|\left\|V_{m,NN}\left(t\right) - V_{m,DAE}\left(t\right)\right\|\right\|^2$	0.0044

DAE vs estimated states constant current
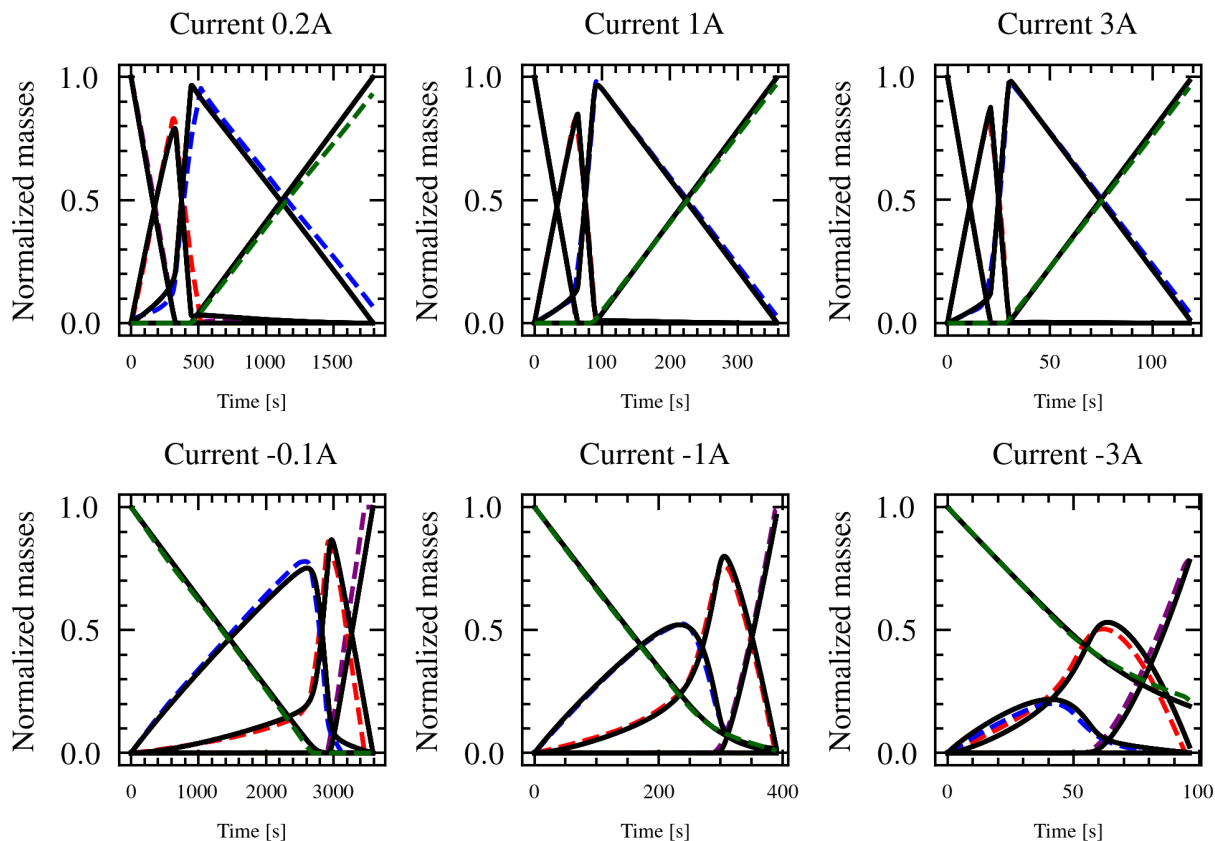
Figure 6.4: DAE State vs Neural Network State comparison

6.4   State Estimation

In this section, we detail the algorithm used for state estimation. The discrete-time neural model formulated (6.19), can be easily used to design observers for state estimation. We use a moving horizon estimator for state estimation and compare it to the classical EKF algorithm that is most widely used for the estimation of non-linear systems.

Extended Kalman Filter

The EKF is a non-linear extension of the Kalman Filter which linearizes the state transition function and output function around the predicted state estimates. The algorithm consists of two main steps: prediction and update. In the prediction step, the algorithm predicts the new state estimate based on the nonlinear state transition function and updates the covariance matrix accordingly. The update step, incorporates measurements to adjust the

DAE vs Neural Net Voltage
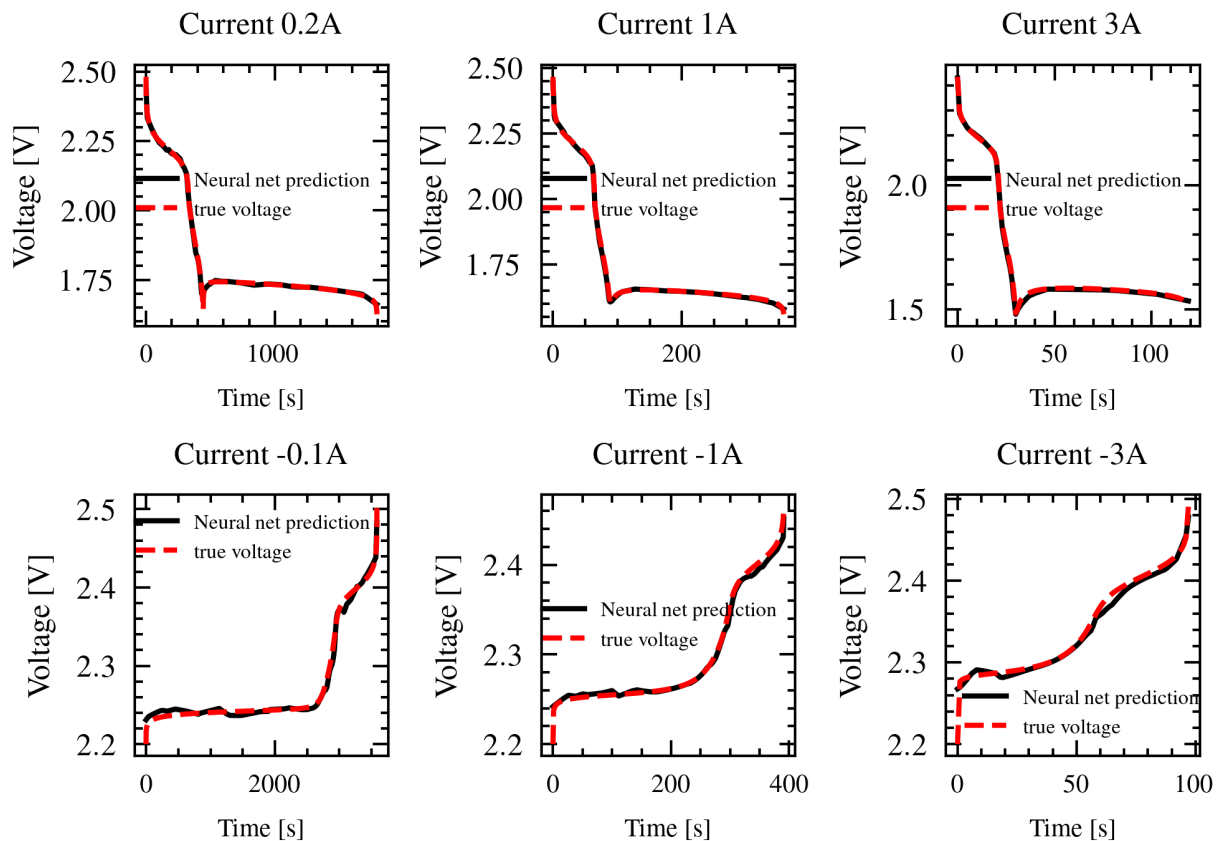
Figure 6.5: DAE voltage output vs Neural Network voltage output comparison

prediction, considering the nonlinear measurement function and updating both the state estimate and covariance matrix. The EKF is summarized in Algorithm 1.

Algorithm 1 Extended Kalman Filter Algorithm [70]

---

0 -1 Initialize state estimate $\hat{x}$ and covariance matrix P Define system dynamics f, measurement model h Define process noise covariance Q and measurement noise covariance R

while new measurements available **do Prediction Step:**
Predict state: $\hat{x}_{k|k-1} = f(\hat{x}_{k-1}, u_{k-1})$
Linearize state transition: $F = \frac{\partial f}{\partial x}\big|_{k-1}$
Predict covariance: $P_{k|k-1} = FP_{k-1}F^T + Q_k$

Update Step:
Obtain measurement: z_k
Compute measurement residual: $y_k = z_k - h(\hat{x}_{k|k-1})$
Linearize measurement: $H = \frac{\partial h}{\partial x}\big|_{k|k-1}$
Compute innovation covariance: $S_k = HP_{k|k-1}H^T + R_k$
Compute Kalman Gain: $K_k = P_{k|k-1}H^T(S_k)^{-1}$
Update state: $\hat{x}_k = \hat{x}_{k|k-1} + K_k y_k$
Update covariance: $P_k = (I - K_k H)P_{k|k-1}$

Moving Horizon Estimation

Moving Horizon Estimation (MHE) is an optimization-based state estimation technique that estimates the current state of a dynamical system using a window of measurements. While MHE is more computationally demanding than traditional EKF, it outperforms EKF, particularly in systems where the underlying dynamics are complex and nonlinear [71]. An additional advantage of MHE is its explicit consideration of constraints that maintain the feasibility of the state estimates. The significance of these factors renders MHE particularly valuable for state estimation in the context of our study.

The key idea behind MHE is to formulate an optimization problem that minimizes the difference between the predicted system outputs and the actual measurements over a finite time horizon. The optimization objective can be tailored to the use case. In our study, use MHE to perform constrained optimization to ensure feasible state estimates and minimize the following errors:

1. Error between state estimates $x(\tau+1)$ and the state dynamic model $f(x(\tau), u(\tau))$

2. Error between true measurement $y(\tau)$ and computed measurements $h(x(\tau), u(\tau))$

3. Coherency between the initial state and its previous estimates

The MHE optimization problem for Li-S is formulated as:

$$\min_{\mathbf{x}} \quad \sum_{\tau=t-h}^{t} ||\mathbf{x}(\tau+1) - \mathbf{f}(\mathbf{x}(\tau), \mathbf{u}(\tau))||_R^2 + ||\mathbf{y}(\tau+1) - \mathbf{f}(\mathbf{x}(\tau), \mathbf{u}(\tau))||_Q^2 + \quad (6.21)$$

$$||\mathbf{x}(\mathbf{t-h}) - \bar{x}(t-h)||_\Pi^2$$

$$\text{subject to} \quad \sum_{i=1}^{5} \boldsymbol{x_i(\tau)} = 1$$

$$x_i(\tau) \geq \mathbf{0} \quad\quad\quad (6.22)$$

The constraints in the MHE ensure feasible state estimates, i.e., the mass of sulfur species is non-negative, and the total mass of sulfur is conserved.
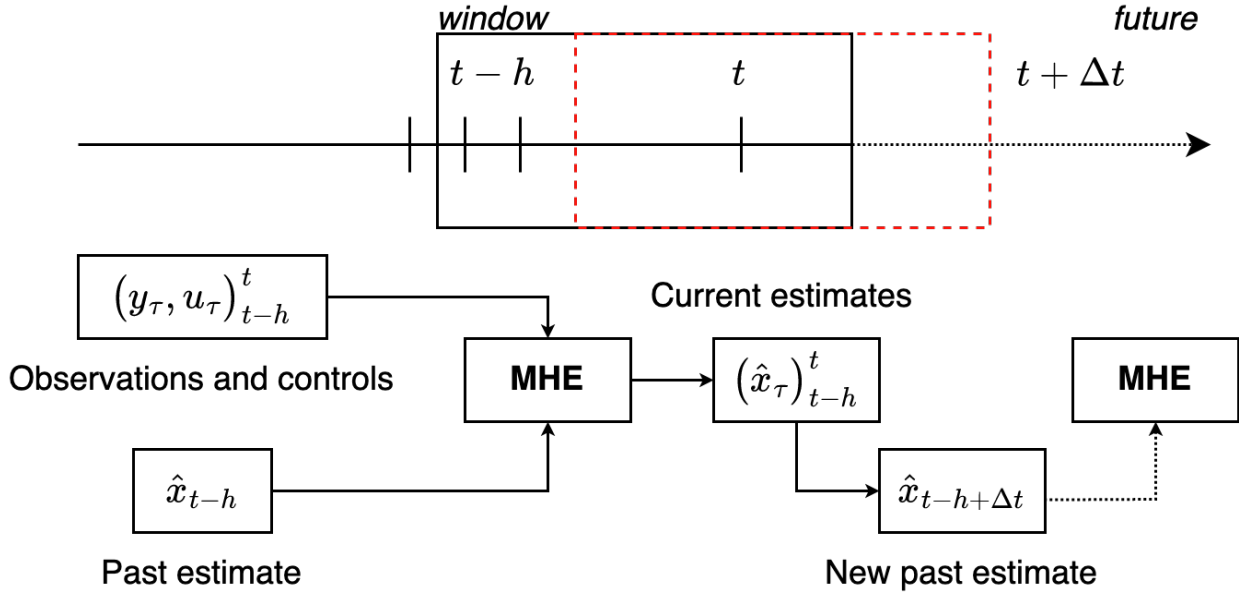
Figure 6.6: MHE framework developed in [68] 'h' here represents the window length and ' δt' represent the update period. For more information refer [68].

6.5 Results

State estimation is performed on the physics-informed neural network model using both traditional EKF and MHE. The performance of the algorithms was tested on varying current profiles. It should be noted that the training of neural nets was done only using constant current profiles, so using varying current profiles for state estimation was a check on the

robustness of both the state estimation algorithm and the performance of neural nets. The dataset used for validation consists of two varying current profiles obtained by simulating the DAE model, which is taken as ground truth data. Validation profiles used for state estimation:
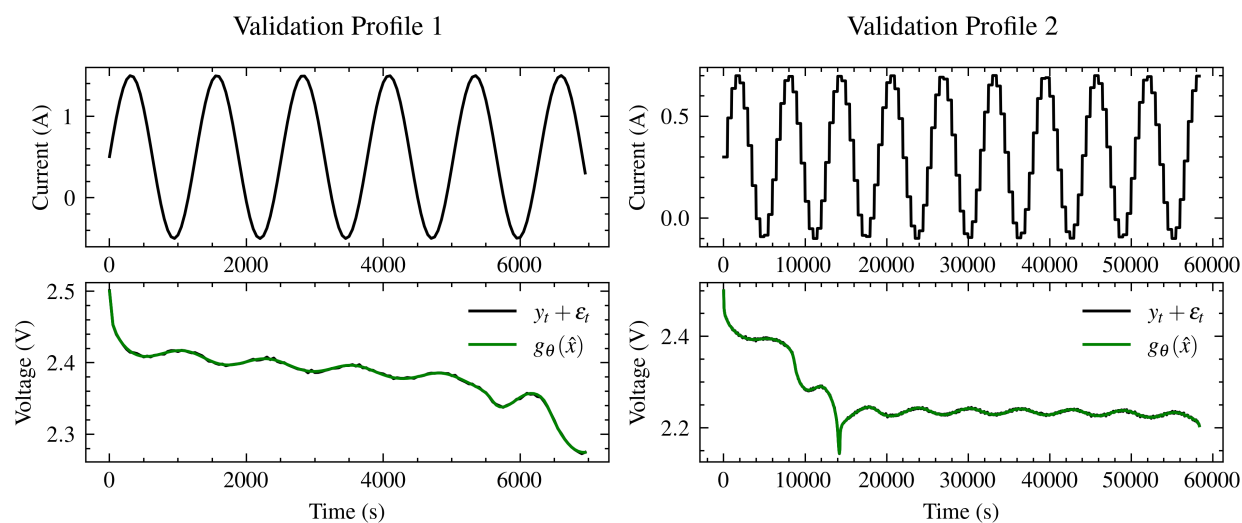
1. Sinusoidal current

2. Pulsed Sinusoidal profile

Figure 6.5 shows the validation current profiles along with the output voltage used as measurement data. Gaussian noise, with a standard deviation of 1mV was added to the DAE output voltage to add measurement noise to the data.

Table 6.2 details the hyperparameter used in MHE and EKF.

Figure 6.7: Validation profiles for State Estimation

Figure 6.8 and Fig. 6.9 show the result of MHE and EKF state estimation. The solid lines in Fig. 6.8 and Fig. 6.9 are the "true" state vales and the dotted line are the state estimates obtained from MHE and EKF. The same initial condition offset is used for both MHE and EKF. Both EKF and MHE estimates converge eventually to the "true" state estimates, as evident in Fig 6.9. It can be observed that MHE performs better than EKF in state estimation for both cases. The MHE allows initial state estimates to be changed and optimized according to (6.22). Because of this, even after incorrect initialization of initial states as shown in Table 6.2, MHE is able to get the optimum values of the initial state and converge faster to the "true" state estimates. Even though MHE performs better than the EKF in this study, it comes with a higher computational cost. The time to run EKF on profiles 1 and 2 was 4 sec and 75 sec respectively, compared to 28 sec and 660 sec to run MHE.

Table 6.2: Hyper-parameters for EKF and MHE

	Parameter	Value
EKF	P	$10^{-5} \cdot \mathbb{I}_5$
	Q	$10^{-5} \cdot \mathbb{I}_5$
	R	$10^{-6} \cdot \mathbb{I}_5$
MHE	Horizon window h	50
	Update period δt	10
	Weight in state dynamic error	50
	Weight in output dynamic error	10
	Weight in initial condition perturbation	1
The initial condition of states for both EKF and MHE	x_0	[.7 .2 .1 0 0]

Table 6.3 summarizes the error in state estimates for both MHE and EKF.

The results show robust performance of the MHE in state estimation of the developed physics-informed neural network, which comes with additional computation cost. In terms of accuracy, MHE decreased the RMSE of state estimates by almost 50% in both validation profiles when compared to EKF 6.3.

Table 6.3: State estimation error comparison

	Validation Profile 1		Validation Profile 2	
State	EKF	MHE	EKF	MHE
x_1	0.179	0.077	0.077	0.033
x_2	0.167	0.074	0.084	0.038
x_3	0.039	0.018	0.053	0.026
x_4	0.003	0.003	0.007	0.003
x_5	0.002	0.0007	0.013	0.018
Average State Error	0.078	0.035	0.047	0.024

6.6   Conclusion

In this chapter, we proposed a physics-informed NN model that approximates a zero-dimensional electrochemical model. The resulting NN model overcomes the numerical challenges of modeling and state estimation of the DAE model while providing physical insight about the state of the Li-S battery. We further use MHE for state estimation of the NN model framework
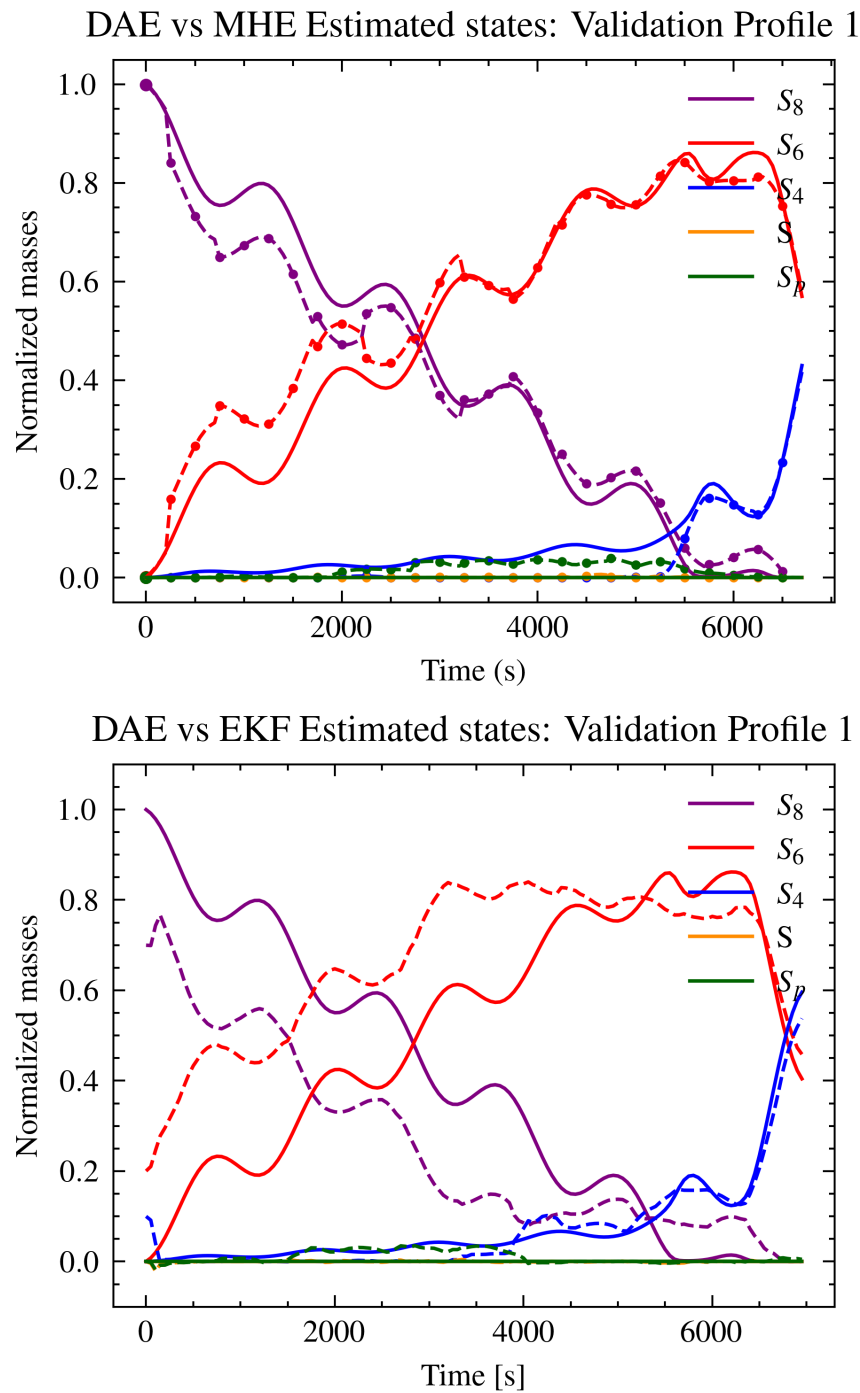
Figure 6.8: State Estimation comparison: Validation profile 1
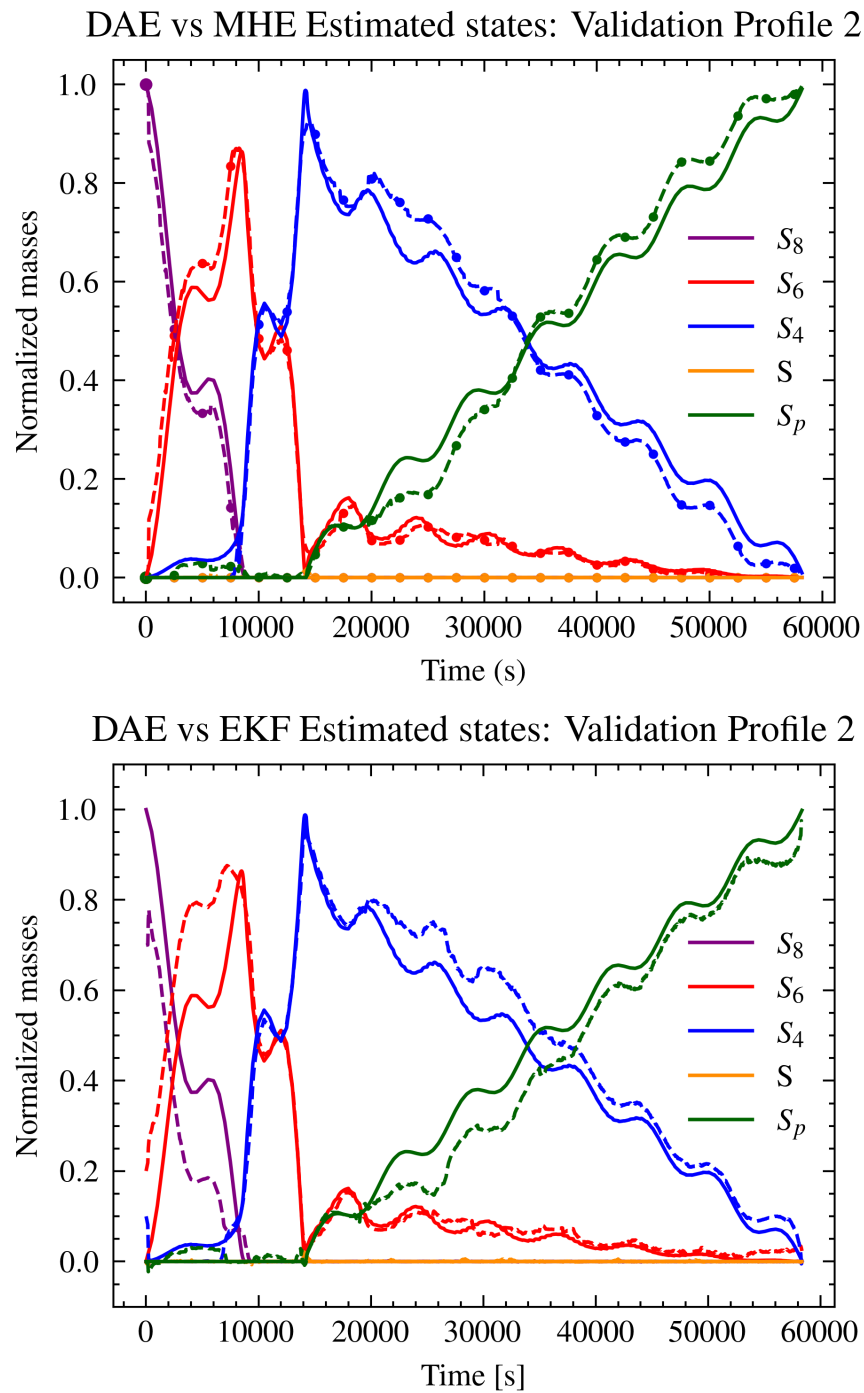
Figure 6.9: State Estimation comparison: Validation profile 2

and compare the results with traditional EKF estimator. The estimation is performed using varying current profiles, which shows the robustness of the estimation method used.

Chapter 7

Conclusion

7.1 Thesis Review

This dissertation addresses critical issues in modeling and state estimations of batteries by presenting a comprehensive methodology across five chapters, each contributing to a deeper understanding and enhanced performance of lithium-ion battery packs and emerging lithium-sulfur batteries.

In Chapter 2, the focus lies on estimating real-time power limits in lithium-ion battery packs composed of heterogeneous cells. The methodology introduced combines an interval prediction algorithm with a modified reference governor, accommodating cell-to-cell variations in a scalable and computationally efficient manner. This chapter establishes a foundation for accurate power predictions without fixating on individual cells.

Chapter 3 builds upon the methodologies presented in Chapter 1 by experimentally quantifying the estimation accuracy of State of Charge (SOC), State of Health (SOH), and State of Power (SOP) interval estimation algorithms. The experimental validation, conducted on a 3-cell battery module designed to mimic larger packs, verifies the robustness of the proposed algorithms with actual data, emphasizing their applicability in real-world scenarios.

In Chapter 4, the dissertation delves into the challenge of power prediction for battery packs with cell-to-cell heterogeneity, extending the analysis to include the effect of heterogeneity in thermal parameters. The chapter introduces a robust interval prediction algorithm achieved through reachability analysis for mixed monotonic systems. Validation on diverse case studies, including a small hybrid electric vehicle (HEV) and a Tesla Powerwall storage, demonstrates the algorithm's accuracy and versatility.

Chapters 5 and 6 shift the focus to emerging battery technologies, specifically lithium-sulfur (Li-S) batteries. Chapter 5 explores global parameter sensitivity in a zero-dimensional Li-S battery model, addressing challenges in modeling and parameter identification critical for battery management systems. The work emphasizes sensitivity analysis under various parameter distributions to reveal their relevance and interdependence.

Chapter 6 concentrates on efficient modeling and state estimation algorithms for Li-S

batteries. Recognizing the limited work in this domain, the chapter proposes a physics-informed neural network model, providing accurate approximations of the electrochemical model. The application of MHE framework is explored and compared to the widely used EKF, demonstrating the algorithm's robustness under varying current profiles.

In conclusion, these chapters represent a comprehensive journey through the intricacies of battery modeling and state estimation, offering novel methodologies, experimental validations, and insights applicable to the dynamic landscape of lithium-ion and lithium-sulfur battery technologies.

7.2 Perspectives on Future Work

Chapters 2, 3 and 4 explore SOP algorithm for the heterogeneous battery pack. While the framework provides promising results on simulation data, it was observed in Chapter 3 that for practical application battery model chosen in algorithm design must fit actual data. In this dissertation, the SOP algorithm was developed using 1RC ECM. For the future, further work can be developed on building SOP algorithms using higher fidelity models, be it 2RC ECMs or electrochemical models. The adaptability of the reachability approach for interval prediction or interval observer for initial state estimation would need to be verified. The challenge of finding accurate interval prediction and interval observer will further increase if electrochemical models are used. Another possible improvement in the presented SOP work would be developing an SOP algorithm based on constant power pulses rather than constant current pulses.

In summary, the suggested research directions for improving the SOP algorithm can be considered.

- Checking the adaptability of SOP algorithm to different models, eg. 2RC/ 3RC ECMs, and electrochemical models.

- Development of interval prediction and interval observer algorithm for higher fidelity electrochemical models

- Developing the SOP algorithm on constant power pulses rather than constant current

Chapters 5, 6 dwell on modeling, state, and parameter estimation challenges of Li-S batteries. The study done in chapter 5 investigates global parameter sensitivity for a zero-dimensional Li-S battery model under different parameter distributions. As observed in this study, the *a-priori* information about a parameter has a significant impact on its relative importance for identification. Future work to quantify the impact of parameter ranking and ordering caused by its *a-priori* information on parameter identification can be explored. This serves as inspiration for future endeavors in the realm of distributionally robust optimal experiment design.

Chapter 6 proposes a physics-informed neural network model to approximate an electro-chemical model, which is further used for state estimation using MHE. Due to the lack of experimentally available data for Li-S batteries, the developed framework assumes the zero-dimensional electrochemical model as the " ground truth". In the future, gaining access to experimental data and facilities related to Li-S batteries would be invaluable for developing models that accurately capture the physical dynamics of the battery.

Bibliography

1. Hsieh, I.-Y. L., Pan, M. S., Chiang, Y.-M. & Green, W. H. Learning only buys you so much: Practical limits on battery price reduction. *Applied Energy* **239,** 218–224 (2019).

2. Howell, D., Cunningham, B., Duong, T. & Faguy, P. Overview of the DOE VTO advanced battery R&D program. *Department of Energy* (2016).

3. Fotouhi, A., Auger, D. J., O'Neill, L., Cleaver, T. & Walus, S. Lithium-sulfur battery technology readiness and applications—a review. *Energies* **10,** 1937 (2017).

4. Beck, D., Dechent, P., Junker, M., Sauer, D. U. & Dubarry, M. Inhomogeneities and cell-to-cell variations in lithium-ion batteries, a review. *Energies* **14,** 3276 (2021).

5. Scrosati, B., Hassoun, J. & Sun, Y.-K. Lithium-ion batteries. A look into the future. *Energy & Environmental Science* **4,** 3287–3295 (2011).

6. Zhang, D. *et al.* Thermal-Enhanced Adaptive Interval Estimation in Battery Packs With Heterogeneous Cells. *IEEE Transactions on Control Systems Technology* (July 2021).

7. Gill, P. *et al. State-Of-Health Estimation Pipeline for Li-ion Battery Packs with Heterogeneous Cells* in *2022 American Control Conference (ACC)* (2022), 1080–1086.

8. Marinescu, M., Zhang, T. & Offer, G. J. A zero dimensional model of lithium–sulfur batteries during charge and discharge. *Physical Chemistry Chemical Physics* **18,** 584–593 (2016).

9. Xu, C., Cleary, T., Li, G., Wang, D. & Fathy, H. Parameter identification and sensitivity analysis for zero-dimensional physics-based lithium-sulfur battery models. *ASME Letters in Dynamic Systems and Control* **1** (2021).

10. Lu, J., Chen, Z., Yang, Y. & Lv, M. Online estimation of state of power for lithium-ion batteries in electric vehicles using genetic algorithm. *IEEE Access* **6,** 20868–20880 (Apr. 2018).

11. Farmann, A. & Sauer, D. U. A comprehensive review of on-board State-of-Available-Power prediction techniques for lithium-ion batteries in electric vehicles. *Journal of Power Sources* **329,** 123–137 (Oct. 2016).

12. Plett, G. L. High-performance battery-pack power estimation using a dynamic cell model. *IEEE Transactions on Vehicular Technology* **53,** 1586–1593 (Sept. 2004).

13. Liu, X., He, Y., Zeng, G., Zhang, J. & Zheng, X. State-of-Power Estimation of Li-Ion Batteries Considering the Battery Surface Temperature. *Energy Technology* **6,** 1352–1360 (July 2018).

14. Liu, X. *et al.* An improved state of charge and state of power estimation method based on genetic particle filter for lithium-ion batteries. *Energies* **13,** 478 (Jan. 2020).

15. Xiang, S., Hu, G., Huang, R., Guo, F. & Zhou, P. Lithium-ion battery online rapid state-of-power estimation under multiple constraints. *Energies* **11,** 283 (Feb. 2018).

16. Jiang, B., Dai, H., Wei, X., Zhu, L. & Sun, Z. Online reliable peak charge/discharge power estimation of series-connected lithium-ion battery packs. *Energies* **10,** 390 (Mar. 2017).

17. Jin, Z., Zhang, Z., Aliyev, T., Rick, A. & Sisk, B. *Estimating the power limit of a Lithium battery pack by considering cell variability* in *SAE Technical Paper* (Apr. 2015).

18. Zhou, Z. *et al.* Peak power prediction for series-connected LiNCM battery pack based on representative cells. *Journal of Cleaner Production* **230,** 1061–1073 (Sept. 2019).

19. Feng, T., Yang, L., Zhao, X., Zhang, H. & Qiang, J. Online identification of lithium-ion battery parameters based on an improved equivalent-circuit model and its implementation on battery state-of-power prediction. *Journal of Power Sources* **281,** 192–203 (May 2015).

20. Waag, W., Fleischer, C. & Sauer, D. U. Adaptive on-line prediction of the available power of lithium-ion batteries. *Journal of Power Sources* **242,** 548–559 (Nov. 2013).

21. Xavier, M. A., de Souza, A. K. & Trimboli, M. S. *An LPV-MPC Inspired Battery SOP Estimation Algorithm Using a Coupled Electro-Thermal Model* in *2021 American Control Conference (ACC)* (May 2021), 4421–4426.

22. Meyer, P. J., Devonport, A. & Arcak, M. *Interval Reachability Analysis: Bounding Trajectories of Uncertain Systems with Boxes for Control and Verification* (Springer International Publishing, 2021).

23. Leurent, E., Efimov, D., Raissi, T. & Perruquetti, W. *Interval prediction for continuous-time systems with parametric uncertainties* in *2019 IEEE 58th Conference on Decision and Control (CDC)* (Dec. 2019), 7049–7054.

24. Althoff, M., Stursberg, O. & Buss, M. *Reachability analysis of nonlinear systems with uncertain parameters using conservative linearization* in *2008 47th IEEE Conference on Decision and Control* (Dec. 2008), 4042–4048.

25. Krewer, U. *et al.* Dynamic models of Li-ion batteries for diagnosis and operation: a review and perspective. *Journal of the Electrochemical Society* **165,** A3656 (Nov. 2018).

26. Perez, H. E., Hu, X., Dey, S. & Moura, S. J. Optimal charging of Li-ion batteries with coupled electro-thermal-aging dynamics. *IEEE Transactions on Vehicular Technology* **66,** 7761–7770 (Mar. 2017).

27. Efimov, D. & Raïssi, T. Design of interval observers for uncertain dynamical systems. *Automation and Remote Control* **77,** 191–225 (Feb. 2016).

28. Zhang, D. *et al. Interval Observer for SOC Estimation in Parallel-Connected Lithium-ion Batteries* in *2020 American Control Conference (ACC)* (2020), 1149–1154.

29. Perez, H., Shahmohammadhamedani, N. & Moura, S. Enhanced performance of li-ion batteries via modified reference governors and electrochemical models. *IEEE/ASME Transactions on Mechatronics* **20,** 1511–1520 (Jan. 2015).

30. Dangwal, C. *et al. Pack Level State-of-Power Prediction for Heterogeneous Cells* in *2022 American Control Conference (ACC)* (June 2022), 1066–1073.

31. Quinn, J. B., Waldmann, T., Richter, K., Kasper, M. & Wohlfahrt-Mehrens, M. Energy density of cylindrical Li-ion cells: a comparison of commercial 18650 to the 21700 cells. *Journal of The Electrochemical Society* **165,** A3284 (Oct. 2018).

32. Mitchell, I. M., Bayen, A. M. & Tomlin, C. J. A time-dependent Hamilton-Jacobi formulation of reachable sets for continuous dynamic games. *IEEE Transactions on Automatic Control* **50,** 947–957 (July 2005).

33. Jaulin, J., Kieffer, M., Didrit, O. & Walter, E. *Applied interval analysis: with examples in parameter and state estimation, robust control and robotics* (Springer Science Business Media, 2001).

34. Chen, X., Abraham, E. & Sankaranarayanan, S. *Taylor model flowpipe construction for non-linear hybrid systems* in *2012 IEEE 33rd Real-Time Systems Symposium* (Dec. 2012), 183–192.

35. Girard, A. *Reachability of uncertain linear systems using zonotopes* in *International Workshop on Hybrid Systems: Computation and Control* (Mar. 2005), 291–305.

36. Stursberg, O. & Krogh, B. H. *Efficient representation and computation of reachable sets for hybrid systems* in *International Workshop on Hybrid Systems: Computation and Control* (Apr. 2003), 482–497.

37. Kurzhanskiy, A. A. & Varaiya, P. Ellipsoidal techniques for reachability analysis of discrete-time linear systems. *IEEE Transactions on Automatic Control* **52,** 26–38 (Jan. 2007).

38. Dreossi, T. *Sapo: Reachability computation and parameter synthesis of polynomial dynamical systems* in *Proceedings of the 20th International Conference on Hybrid Systems: Computation and Control* (Apr. 2017), 29–34.

39. Meyer, P. J., Devonport, A. & Arcak, M. *TIRA: Toolbox for interval reachability analysis* in *Proceedings of the 22nd ACM International Conference on Hybrid Systems: Computation and Control* (Apr. 2019), 224–229.

40. *Traction Battery*

41. *Tesla Powerwall* https://www.tesla.com/powerwall.

42. Yao, S., Liu, W., Cheng, J. & Shen, Y. Series-parallel grouping modeling simulation and experimental analysis of zinc-nickel single flow batteries. *Journal of Renewable and Sustainable Energy* **10,** 034105 (May 2018).

43. Jahangiri, M., Nematollahi, O., Sedaghat, A. & Saghafian, M. Techno-economical assessment of renewable energies integrated with fuel cell for off grid electrification: A case study for developing countries. *Journal of Renewable and Sustainable Energy* **7,** 023123 (Mar. 2015).

44. Laboratory, N. R. E.

45. Parke, C. D., Teo, L., Schwartz, D. T. & Subramanian, V. R. Progress on continuum modeling of lithium–sulfur batteries. *Sustainable Energy & Fuels* **5,** 5946–5966 (2021).

46. Lim, W.-G., Kim, S., Jo, C. & Lee, J. A comprehensive review of materials with catalytic effects in Li–S batteries: enhanced redox kinetics. *Angewandte Chemie* **131,** 18920–18931 (2019).

47. Peng, L. *et al.* A fundamental look at electrocatalytic sulfur reduction reaction. *Nature Catalysis* **3,** 762–770 (2020).

48. Feng, S., Fu, Z.-H., Chen, X. & Zhang, Q. A review on theoretical models for lithium–sulfur battery cathodes. *InfoMat* **4,** e12304 (2022).

49. Shateri, N., Shi, Z., Auger, D. J. & Fotouhi, A. Lithium-sulfur cell state of charge estimation using a classification technique. *IEEE Transactions on Vehicular Technology* **70,** 212–224 (2020).

50. McCreary, C., An, Y., Kim, S. U. & Hwa, Y. A perspective on li/s battery design: Modeling and development approaches. *Batteries* **7,** 82 (2021).

51. Park, S., Kato, D., Gima, Z., Klein, R. & Moura, S. Optimal experimental design for parameterization of an electrochemical lithium-ion battery model. *Journal of The Electrochemical Society* **165,** A1309 (2018).

52. Kumaresan, K., Mikhaylik, Y. & White, R. E. A mathematical model for a lithium–sulfur cell. *Journal of the electrochemical society* **155,** A576 (2008).

53. Ghaznavi, M. & Chen, P. Analysis of a mathematical model of lithium-sulfur cells part III: electrochemical reaction kinetics, transport properties and charging. *Electrochimica Acta* **137,** 575–585 (2014).

54. Ghaznavi, M. & Chen, P. Sensitivity analysis of a mathematical model of lithium–sulfur cells part i: Applied discharge current and cathode conductivity. *Journal of power sources* **257,** 394–401 (2014).

55. Ghaznavi, M. & Chen, P. Sensitivity analysis of a mathematical model of lithium–sulfur cells: Part II: Precipitation reaction kinetics and sulfur content. *Journal of Power Sources* **257,** 402–411 (2014).

56. Parke, C. D., Subramaniam, A., Kolluri, S., Schwartz, D. T. & Subramanian, V. R. An efficient electrochemical tanks-in-series model for lithium sulfur batteries. *Journal of The Electrochemical Society* **167,** 163503 (2020).

57. Ramancha, M. K., Astroza, R., Madarshahian, R. & Conte, J. P. Bayesian updating and identifiability assessment of nonlinear finite element models. *Mechanical Systems and Signal Processing* **167,** 108517 (2022).

58. Saltelli, A. *et al.* Variance based sensitivity analysis of model output. Design and estimator for the total sensitivity index. *Computer physics communications* **181,** 259–270 (2010).

59. Huang, Z., Zhang, D., Couto, L. D., Yang, Q.-H. & Moura, S. J. *State estimation for a zero-dimensional electrochemical model of lithium-sulfur batteries* in *2021 American Control Conference (ACC)* (2021), 3114–3119.

60. Fronczek, D. N. & Bessler, W. G. Insight into lithium–sulfur batteries: Elementary kinetic modeling and impedance simulation. *Journal of power sources* **244,** 183–188 (2013).

61. Doyle, M., Fuller, T. F. & Newman, J. Modeling of galvanostatic charge and discharge of the lithium/polymer/insertion cell. *Journal of the Electrochemical society* **140,** 1526 (1993).

62. Andersson, J. A. E., Gillis, J., Horn, G., Rawlings, J. B. & Diehl, M. CasADi – A software framework for nonlinear optimization and optimal control. *Mathematical Programming Computation* **11,** 1–36 (2019).

63. Joe, S. & Kuo, F. Y. Remark on algorithm 659: Implementing Sobol's quasirandom sequence generator. *ACM Transactions on Mathematical Software (TOMS)* **29,** 49–57 (2003).

64. Iwanaga, T., Usher, W. & Herman, J. Toward SALib 2.0: Advancing the accessibility and interpretability of global sensitivity analyses. *Socio-Environmental Systems Modelling* **4,** 18155. https://sesmo.org/article/view/18155 (May 2022).

65. LeBlanc, D. J. *Road departure crash warning system field operational test: methodology and results. volume 1: technical report* tech. rep. (University of Michigan, Ann Arbor, Transportation Research Institute, 2006).

66. Xu, C., Doosthosseini, M. & Fathy, H. K. Lithium-Sulfur Battery Discharge Optimization using a Thermally-Coupled Equivalent Circuit Model. *IFAC-PapersOnLine* **54,** 399–405 (2021).

67. Huang, Z. *et al.* On Electrochemical Model-based State Estimation for Lithium-Sulfur Batteries. *IEEE TCST.* (in press).

68. Goujard, G., Dangwal, C., Gill, P., Kato, D. & Moura, S. Modeling and State Estimation for Lithium Sulfur Batteries as a Piecewise Affine System. (in press).

69. Bruce, P. G., Freunberger, S. A., Hardwick, L. J. & Tarascon, J.-M. Li–O2 and Li–S batteries with high energy storage. *Nature materials* **11,** 19–29 (2012).

70. Ribeiro, M. I. Kalman and extended kalman filters: Concept, derivation and properties. *Institute for Systems and Robotics* **43,** 3736–3741 (2004).

71. Allgöwer, F., Badgwell, T. A., Qin, J. S., Rawlings, J. B. & Wright, S. J. Nonlinear predictive control and moving horizon estimation—an introductory overview. *Advances in control: Highlights of ECC'99,* 391–449 (1999).